Spectral and Timing Studies of Accretion Disk in Black Hole Binaries

A thesis submitted in partial fulfilment of

the requirements for the degree of

Doctor of Philosophy

by

Anjali Rao Jassal

(Roll No. 11330003)

Under the guidance of

Dr. Santosh. V. Vadawale

Astronomy & Astrophysics Division

Physical Research Laboratory, Ahmedabad, India.

DEPARTMENT OF PHYSICS

INDIAN INSTITUTE OF TECHNOLOGY GANDHINAGAR

2015

to

my parents

Declaration

I declare that this written submission represents my ideas in my own words and where others' ideas or words have been included, I have adequately cited and referenced the original sources. I also declare that I have adhered to all principles of academic honesty and integrity and have not misrepresented or fabricated or falsified any idea/data/fact/source in my submission. I understand that any violation of the above will be cause for disciplinary action by the Institute and can also evoke penal action from the sources which have thus not been properly cited or from whom proper permission has not been taken when needed.

Signature

(Name: Anjali Rao Jassal)

(Roll No: 11330003)

Date: January 08, 2016

CERTIFICATE

It is certified that the work contained in the thesis titled "**Spectral and Timing Studies of Accretion Disk in Black Hole Binaries**" by **ANJALI RAO JASSAL** (Roll Number: 11330003), has been carried out under my supervision and that this work has not been submitted elsewhere for a degree.

Dr. Santosh V. Vadawale
Associate Professor
Astronomy and Astrophysics Division
Physical Research Laboratory
Ahmedabad-380009, India

Acknowledgement

First of all, I would like to express my sincere thanks to my thesis supervisor, Dr. Santosh V. Vadawale, for his valuable guidance and support through out my PhD tenure at PRL. I express my deepest regards for him. I am highly grateful to him as he introduced me to the interesting field of X-ray astronomy and guided me to learn its different aspects. I feel privileged to have Dr. Vadawale as my thesis supervisor.

I would like to extend my heartfelt gratitude to Prof P. Janardhan. I am thankful to him for help and support during my hard times. Your guidance and motivation are valuable to me.

I thank Prof. J. N. Goswami, former Director; Prof. Utpal Sarkar, Director; Prof P. Janardhan, Dean; Prof. S. Ramachandran, Chairperson of Academic Committee and Prof. K. S. Baliyan, area chairman, for providing necessary facilities to carry out research work. I thank Dr. B. G. Vaishnav for his help in academic matters.

I acknowledge the help I received from Prof. A. R. Rao and Prof. Ranjeev Misra in my research work. I am thankful to them for fruitful scientific discussions. I thank Mr. Biplob Sarkar for regular scientific discussions.

I thank Prof. N. M. Ashok for his continuous support during my tenure at PRL. I thank Prof. B. G. Anandrao for teaching us the course in Astronomy during the course work. I take the opportunity to thank the faculties in A&A division, Prof. T. Chandrasekhar, Prof. D.P.K. Banerjee, Prof. Hari Om Vats, Prof. U. C. Joshi, Dr. S. Naik, Dr. Shashikiran Ganesh, and Dr. Mudit K. Srivastava. I acknowledge Midhun for his help and discussions.

I am thankful to Dr. Ashok Singal, who has always been a very dear friend and a teacher. I always enjoyed long and fruitful scientific discussions with him. I thank Dr. Dibyendu Chakrabarty for his continuous support and motivation.

I thank all the staff members of PRL computer center for providing computational and internet facilities. I thank Mr. Jigar Raval, Mr. Hitendra Mishra, Mr. Alok Srivastava and Mr. Tejas Sarvaiya from computer center. I am thankful to staff members of PRL library, Mrs. Nistha Anilkumar and Mrs. Pragya Pandey. I am thankful to Bhagirath bhai, Doshi ji, Pancholi ji, and Ms. Prabha Chauhan.

I specially thank my senior Susanta for his unconditional help. His support is valuable to me. I thank my seniors Ashish, Tapas, Sunil, Arun Awasthi, Amrendra, Kaushik, Yogita, Chinmay, Vimal, Vineet and Arvind. I thank Blesson, Vijayan, Shweta and Rathnakumar.

I thank my batchmates Yashpal, Naveen, Dillip, Girish, Gulab, Gaurav Tomar, *Gaurav Sharma, Tanmoy, Priyanka, Monojit, Upendra, Uma, Lata, Dinesh Kumar, Dinesh Rajput, Bhavya, Lekshmi, Midhun, Damodar, Avdhesh, Wageesh, Aadhi and Reddy. I am thankful to Arun Pandey, Gaurav Jaisawal, Kamlesh, Navpreet, Rukmani, Rupa, Prahlad, Kuldeep, Satish, Chandan, Kumar, Ali, Aarthy, and Santosh Chaudhary.*

I thank my friends Dharak, Ketan, Abdul, Deepa, Anushya, Taranpreet, Balaji, and Rishabh for their constant support. I acknowledge the support from my friends Varun and Vaibhav. My special thanks to Ami and Jinia for being there with me always. Thank you :)

I am thankful to Sangharsh, Vicky, Mantu, Mukesh, Kunal and Suraj for their support and help.

Last, but not the least, I am thankful to my parents for being a continuous source of love, support and motivation. I can never thank you enough. I acknowledge my siblings Ampoo and Sonam and my cousins for always being with me.

Abstract

Accretion around compact objects is the most efficient way of extracting energy from material in an accretion disk. Luminous accretion disks around black holes in mass transferring black hole binaries offer an opportunity to study accretion processes taking place in the extreme conditions of temperature and gravitational field. However, these astrophysical sources cannot be observed with ground based conventional telescopes because they emit mainly in X-rays. Therefore, data are collected with space borne X-ray observatories. Spectra, light curves and images extracted from data are used as probes to understand the radiative processes in accretion disks. Although a significant understanding of the sources has been developed with the help of several empirical and theoretical studies, there are several phenomena, which are not understood. This thesis presents the efforts that have been made to understand some of these phenomena.

A majority of black hole binaries are transient in nature and they keep on switching between quiescent and outburst states. It is generally believed that an accretion disk is truncated far away from the central black hole during quiescent states. However, the observational evidence for this general picture is indirect at best. We studied a transient black hole candidate MAXI J1659−152 during its 2010 outburst, which was detected during very early stages of the outburst. We investigated the variation of the inner disk radius with progress of the outburst and found that the disk is truncated at larger radii in the beginning. A systematic decrease in the inner disk radius was found as the source transitions towards the soft states. We estimated mass of the black hole to be 8.1±2.9 $M_{\odot}$ with the help of normalization of the disk blackbody component.

A transient black hole candidate IGR J17091−3624 is studied, which behaved like 'normal' black hole binaries except during its latest outburst in 2011. The source showed properties similar to a unique black hole binary GRS 1915+105, known for exhibiting extreme variability. High mass accretion rate is believed to give rise to extreme variability, therefore IGR J17091−3624 is expected to be a bright source. However, IGR J17091−3624 is about 20 times fainter as compared to GRS 1915+105. We performed a comparative study of the two sources by

investigating 'heartbeat'-type variability observed in their light curves. The light curves were folded and spectra were generated for the 5 phases of 'heartbeat' oscillations. The spectra were fitted simultaneously by tying the system parameters and leaving the accretion-process-dependent parameters independently free across the 5 phases. We found important constraints on mass, distance, inclination and spin of IGR J17091−3624. It was noticed that the estimated value of spin is low ($a_* < 0.2$) as opposed to the high value of spin for GRS 1915+105. We suggest that the low spin of the black hole in IGR J17091−3624 can be a reason behind its faintness as compared to GRS 1915+105 instead of showing variability patterns arising from high mass accretion rate.

Black hole binaries are known for showing quasi periodic oscillations (QPOs) during hard states, which appear as narrow peaks superimposed on the broad band continuum in power density spectrum. Several studies have shown the correlation between QPO properties and spectral parameters, indicating a close link between the two. However, the mechanism behind generation of QPOs is not well understood. The thesis presents our attempts to understand the QPO mechanism by simulating light curves. We studied a NuSTAR observation of GRS 1915+105, which has a power law dominated spectrum and shows the presence of reflection component. Since there is only one primary component, we make a hypothesis that the QPO is generated as a result of oscillation of some of the spectral parameters (instead of spectral components) at frequencies close to that of the QPO. We test the hypothesis by finding whether the simulated results explain the observed energy dependence of QPO or not. It was found that the observed trend of increasing QPO power with energy can be reproduced qualitatively if the spectral index is varied with the phases of QPO. Variation of other spectral parameters does not reproduce the observed energy dependence. The variation of spectral index is verified by performing phase-resolved spectroscopy for the phases of QPO. The results clearly show the variation of spectral index with the phases of QPO. The finding of variation of spectral index is an important result and it puts significant constraints on the models explaining modulation mechanism for QPOs.

Keywords: accretion, accretion disks, black hole physics, X-rays: binaries, X-rays: individual (GRS 1915+105, MAXI J1659−152, IGR J17091−3624).

Contents

List of Figures

List of Tables

Chapter 1

Introduction

The work presented in this thesis includes the study of black hole binaries which harbor a stellar mass black hole and a normal star. These sources are luminous in X-rays and radio bands due to the presence of accretion disk around the black hole that consists of the material from the normal star, generally referred as 'companion'. The inner region of the disk primarily contributes to the emission in X-rays. The gradual sinking of the material in the accretion disks eventually leads to the accretion of material onto the black hole. About 70 accreting black hole candidates have been discovered till date. These black hole sources and the accretion disk are discussed in the present chapter. Among the different aspects, those properties are discussed which are relevant to the work illustrated in the following chapters.

1.1 X-ray binaries

More than half of the stars are the members of binary star systems wherein two stars revolve around their common center of mass. The stars in a close binary system affect the evolution of each other and the binary evolves as a whole. A class of binary stars which are bright in X-rays consists of a compact object; a black hole/neutron star, and a normal star. These binaries are called X-ray binaries (XRBs) and are among the brightest source in the X-ray sky. XRBs are high-energy emitters and highly variable sources. The compact star in an XRB accretes the material from the companion star, however the mode of accretion depends on the mass of the companion. A high mass ($\gtrsim$10 $M_\odot$) star emits strong stellar wind compared to a low mass star. In an X-ray binary consisting of a high mass companion, a fraction of emanating material is captured by the compact object. Such systems are termed as *high mass X-ray binaries (HMXRBs)* and these are bright in optical as well, owing to the brightness of the high mass companion, which is generally a high mass O- or B-type star. Fig (1.1a) shows a high mass star and a compact object in the orbit accreting through stellar wind.

Accretion via wind is not an effective way of transferring material from the companion if it is a low mass star ($\sim 1 M_\odot$) because the wind is feeble in such systems. Instead, the transfer of material takes place in a more efficient way in such binary systems. As a low mass companion expands during its evolutionary stages, its size increases. As it expands further, it starts to fill its Roche lobe, which is the surface of equal gravitational potential including the inner Lagrangian point L_1. The expanding material escapes through the inner Lagrangian point L_1 of the system and it is captured by the gravitational field of the compact object, as shown in Fig (1.1b). These binaries are called *low mass X-ray binaries (LMXRBs)*. It is noticeable here that the X-ray binaries are classified as low-mass or high-mass depending on the mass of the companion solely, irrespective of the mass of the compact object. The incoming material from the companion star has sufficient angular momentum that it forms a disk around the compact object. These disks are called *accretion disks* which play a crucial role in the observed luminosity and hence in the detection of black hole sources.

1.2 Black hole binaries

If a compact object in an X-ray binary is a black hole, the binary is called a *black hole binary*. Black holes are the end products of stellar evolution of a massive star ($\gtrsim$20$M_\odot$). The end stages of the stellar evolution are marked by the discontinuation of the nuclear burning in the core. Since there is no outward pressure to support the inward gravitational force, the star undergoes a

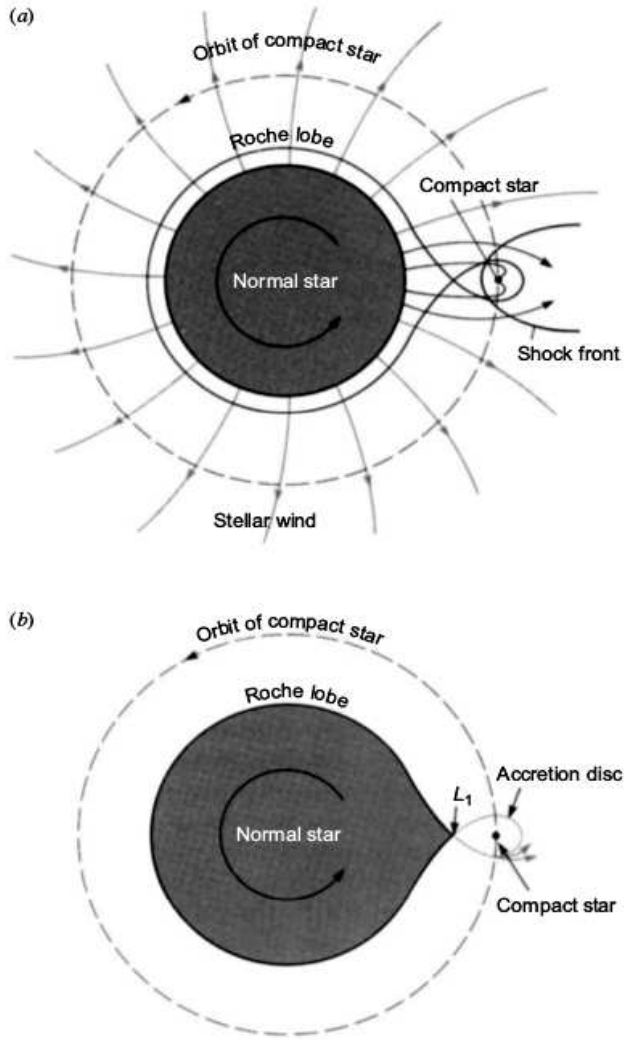

Figure 1.1: A schematic diagram showing the two modes of accretion through which a compact object accretes in a binary star system. Panel (a) shows a compact object accreting the material through the strong stellar wind of the high mass companion. Panel (b) shows the companion star filling its Roche lobe and the compact object accreting the material escaped through the inner Lagrangian point. *Figure adapted from 'High Energy Astrophysics' by M. S. Longair.*

gravitational collapse of the core which results either in a neutron star or a black hole. More massive the progenitor is, higher is the probability of the formation of a black hole. Mass of the resulting stellar mass black hole lie in a range of 3-20 $M_{\odot}$, where the lower limit is called Tolman-Oppenheimer-Volkoff limit. The lower limit on the mass of the compact object helps in its identification as a black hole or a neutron star. Therefore, mass estimation of the compact object in an X-ray binary is of great importance in order to understand the properties of the system. The most reliable estimate of the mass of a compact object is obtained from the radial velocity measurements of the companion star. Only those black hole sources are classified as confirmed black hole binaries for which the companion is observable and the mass function is found to be $\gtrsim 3M_{\odot}$. However, in several cases, the radial velocity measurement is not possible because of companion's low luminosity. Although, these X-ray binaries show spectral and temporal properties similar to that of the confirmed black hole binaries, these binaries are called 'candidates' because of the lack of confirmation on the compact object's mass. A list of 20 confirmed and 20 candidate black hole sources is given in Remillard & McClintock (2006, hereafter RM06). The estimated mass of the confirmed black holes lies well within the mass bracket of 3-20$M_{\odot}$.

A black hole remains undetected from this stage onwards as no photon escapes the event horizon of the black hole. However, the surroundings of the black hole may become illuminated with the material accreted from the companion star in a binary system. The angular momentum of the accreted material causes it to form a disk around the black hole. In the case of black hole binaries, the X-ray emission comes mainly from the inner regions of the disk, thereby study of black hole binaries offers an opportunity to understand the behavior of material in the conditions of high temperature and strong gravitational potential of the black hole. In the following section the basics of accretion disks are discussed, followed by some of the characteristic properties of the black hole binaries owing to the presence of disks in such systems.

1.3 Accretion disks

Accretion processes taking place in the disks around compact objects are more efficient than the nuclear burning in the core of the stars. With an efficiency of conversion as high as 42.6%, the maximally rotating Kerr black holes are the most powerful energy sources in the universe. The accretion disk around black holes is fed by the material from the companion star, which could be accreted via any of the two mechanisms viz. wind accretion and Roche lobe overflow (see Fig 1.1). The incoming material has adequate angular momentum that it cannot accrete onto the black hole directly until it looses most of its angular momentum. Conservation of angular momentum causes the material to form a ring at a certain radius around the black hole. The dissipative processes including collision of gas elements, shocks and viscous dissipation convert some of the energy of the ordered bulk orbital motion into heat, a portion of which is radiated. As a result of this loss of energy, the material sinks deeper into the gravitational potential of the black hole which requires loss of angular momentum. Viscosity redistributes angular momentum in the disk and transfers the angular momentum outwards. The initial ring of matter captured from the companion star spreads both outwards and inwards forming an accretion disk around the black hole.

Briefly, viscosity plays two major roles in an accretion disk; (a) extraction of energy from the material (b) redistribution of angular momentum. This ultimately leads to the accretion of material onto the black hole. Viscous forces give rise to a small radially inward velocity to the matter which is superimposed on the azimuthal Keplerian velocity. This causes a spiral motion of the material in the disk. According to Shakura & Sunyaev (1973) model of accretion disks, the heat generated is radiated locally. Also, the temperature in the disk is a function of radius,

$$T(R) \propto R^{-3/4} \tag{1.1}$$

This is why the radiation from the accretion disk is called multi-temperature or multi-color black body. The observed spectrum from black hole binaries clearly indicate the presence of a multi-temperature disk, along with the presence of other components. The standard accretion disk and its structure are discussed here briefly.

1.4 Steady State Accretion Disk

The steady state accretion disk is discussed in 'Accretion Power in Astrophysics' by Frank, King and Raine. The same is discussed here briefly. We shall discuss here the dynamics of a thin accretion disk which lies close to the plane $z = 0$ in cylindrical polar coordinates. It is assumed that the material in the disk revolves in circular Keplerian orbits. Let M be the mass of the primary. Let $\dot{M}$ be the mass accretion rate and Σ and ρ are surface and volume densities respectively.

The disk is assumed to be thin and therefore the surface density Σ becomes an important parameter, which is defined as mass per unit surface area of the disk. The surface density is obtained by integrating the volume density ρ in the z-direction. Let us consider that the disk has the scale height H, and ρ can be approximated as,

$$\rho = \frac{\Sigma}{H} \tag{1.2}$$

If pressure in the disk is P, the speed of sound c_s is given as,

$$c_s = \sqrt{\frac{P}{\rho}} \tag{1.3}$$

where pressure P is the sum of gas pressure and radiation pressure, i.e.

$$P = \frac{\rho k T_c}{\mu m_p} + \frac{4\sigma}{3c} T_c^4 \tag{1.4}$$

Here, T_c is the central temperature i.e. in plane z=0,

$$T_c(R) = T_c(R, z = 0)$$

It is considered that the disk is thin and there is no flow in the z-direction. Therefore, hydrostatic equilibrium must hold in the z-direction wherein the outward pressure balances the inward gravitational pull, i.e.

$$\frac{1}{\rho}\frac{\partial P}{\partial z} = -\frac{GMz}{(R^2+z^2)^{3/2}}$$

For a thin disk $R >> z$, therefore,

$$\frac{1}{\rho}\frac{\partial P}{\partial z} = -\frac{GMz}{R^3}$$

Also, we can approximate $\frac{\partial P}{\partial z} \sim \frac{P}{H}$, therefore

$$\frac{1}{\rho}\frac{P}{H} \sim \frac{GMz}{R^3}$$

Simplifying using equation (1.3),

$$H \sim c_s \left(\frac{R^3}{GM}\right)^{1/2} \tag{1.5}$$

The energy generated per unit disk face area, $D(R)$ is given as,

$$D(R) = \frac{3GM\dot{M}}{8\pi R^3}\left[1 - \left(\frac{R_*}{R}\right)^{1/2}\right]$$

where R_* is the size of accreting star. The radiated energy can be approximated as,

$$D(R) = \frac{4\sigma}{3\tau}T_c^4$$

Therefore,

$$\frac{4\sigma}{3\tau}T_c^4 = \frac{3GM\dot{M}}{8\pi R^3}\left[1 - \left(\frac{R_*}{R}\right)^{1/2}\right] \tag{1.6}$$

For simplicity, let us substitute

$$f^4 = \left[1 - \left(\frac{R_*}{R}\right)^{1/2}\right] \tag{1.7}$$

In equation (1.6), τ is opacity and is given as,

$$\tau = \rho H \kappa_R \tag{1.8}$$

where κ_R is Rosseland mean opacity.

$$\tau = \Sigma\kappa_R \tag{1.9}$$

It is assumed that ρ and T_c are such that the Rosseland mean opacity is well approximated by Kramer's law,

$$\kappa_R = 5 \times 10^{24} \rho_o T_{co}^{-7/2} \quad cm^2 g^{-1} \tag{1.10}$$

Also, from the conservation of angular momentum we get,

$$\nu\Sigma = \frac{\dot{M}}{3\pi}\left[1 - \left(\frac{R_*}{R}\right)^{1/2}\right] \tag{1.11}$$

where ν is kinematic viscosity. It is clear from the equation that the surface density can be found as a function of radius and mass accretion rate, if the dependence of ν on radius, mass and accretion rate is known. In 1973, Shakura & Sunyaev (1973) gave a viscosity prescription, which suggests that the viscous stresses are proportional to the total pressure. According to the prescription,

$$\nu = \alpha c_s H \tag{1.12}$$

where α is viscosity parameter.

All the important equations are listed here, which are used to find the disk structure for a steady state thin disk.

1. $\rho = \dfrac{\Sigma}{H}$

2. $H = c_s \left(\dfrac{R^3}{GM}\right)^{1/2}$

3. $c_s^2 = \dfrac{P}{\rho}$

4. $P = \dfrac{\rho k T_c}{\mu m_p} + \dfrac{4\sigma}{3c} T_c^4$

5. $\dfrac{4\sigma}{3\tau} T_c^4 = \dfrac{3GM\dot{M}}{8\pi R^3}\left[1 - \left(\dfrac{R_*}{R}\right)^{1/2}\right]$

6. $\tau = \Sigma \kappa_R$

7. $\nu\Sigma = \dfrac{\dot{M}}{3\pi}\left[1 - \left(\dfrac{R_*}{R}\right)^{1/2}\right]$

8. $\nu = \alpha c_s H$

9. $\kappa_R = 5 \times 10^{24} \rho_o T_{co}^{-7/2} \quad cm^2 g^{-1}$

10. $f^4 = \left[1 - \left(\frac{R_*}{R}\right)^{1/2}\right]$

Also, following conversions are used to convert the parameters into dimensionless parameters,

$$\rho = \rho_o \quad gcm^{-3}$$
$$T_c = T_{co} \quad K$$
$$M = m \quad M_\odot$$
$$\dot{M} = \dot{M}_{16} \quad 10^{16} \quad gs^{-1}$$
$$R = R_{10} \quad 10^{10} \quad cm$$

We shall start with eq. (5) and substitute the term containing radius using eq. (10) and opacity from eq. (6),

$$T_c^4 = \frac{3G}{8\pi}\frac{M\dot{M}}{R^3}\frac{3}{4\sigma}(\Sigma\kappa_R) f^4$$

Substituting dimensionless parameters and κ_R from eq. (9),

$$T_{co}^{15/2} = 5 \times 10^{24} \frac{(GM)^{1/2}}{c_s R^{3/2}} \frac{3G}{8\pi}\frac{3}{4\sigma}\Sigma^2 \frac{M\dot{M}}{R^3} f^4 cm^5 g^{-2} K^{-4} \tag{1.13}$$

It is clear from the above expression that either T_c or Σ has to be found independently in order to make further progress. For a gas pressure dominated region, eq. (4) can be written as,

$$P = \frac{\rho k T_c}{\mu m_p}$$

With the help of above expression, c_s can be written in terms of T_c, i.e.

$$c_s^2 = \frac{P}{\rho} = \frac{kT_c}{\mu m_p} \tag{1.14}$$

Substituting c_s in eq. (1.13) and solving further gives,

$$T_{co}^8 = 5 \times 10^{24} \left(\frac{G\mu m_p}{k}\right)^{1/2} \frac{3G}{8\pi}\frac{3}{4\sigma}\Sigma^2 \frac{M^{3/2}\dot{M}}{R^{9/2}} f^4 cm^5 g^{-2} K^{-9/2} \tag{1.15}$$

We shall use this result later. Now substituting eq. (10) in eq. (7),

$$\nu\Sigma = \frac{\dot{M}}{3\pi} f^4 \tag{1.16}$$

Using eq. (1.14), eq. (2) and eq. (8), the expression for Σ is,

$$\Sigma = \frac{1}{T_{co}} \frac{\mu m_p}{k} \left(\frac{GM}{R^3}\right)^{1/2} \frac{\dot{M}}{3\pi} f^4 \alpha^{-1} K^{-1} \tag{1.17}$$

Eliminating T_c from above using eq. (1.15) and substituting dimensionless parameters,

$$\Sigma = 3.3\alpha^{-4/5} m^{1/4} \dot{M}_{16}^{7/10} R_{10}^{-3/4} f^{14/5} cm^{-2} g \tag{1.18}$$

Using above expression to find T_c from eq. (1.15),

$$T_c = 2.5 \times 10^4 \alpha^{-1/5} m^{1/4} \dot{M}_{16}^{3/10} R_{10}^{-3/4} f^{6/5} K \tag{1.19}$$

With the help of eq. (2), (1.14) and (1.19), H can be expressed as,

$$H = 1.5 \times 10^8 \alpha^{-1/10} m^{-3/8} \dot{M}_{16}^{3/20} R_{10}^{9/8} f^{3/5} cm \tag{1.20}$$

Now, volume density ρ can be easily found using eq. (1), (1.18) and (1.20),

$$\rho = 2.2 \times 10^{-8} \alpha^{-7/10} m^{5/8} \dot{M}_{16}^{11/20} R_{10}^{-15/8} f^{11/5} cm^{-3} g \tag{1.21}$$

Solving for opacity using eq. (5) gives,

$$\tau = 111.1\alpha^{-4/5} \dot{M}_{16}^{1/5} f^{4/5} \tag{1.22}$$

Using eq. (8), (1.19), and (1.20) we can find ν,

$$\nu = 2.7 \times 10^{14} \alpha^{4/5} m^{-1/4} \dot{M}_{16}^{3/10} R_{10}^{3/4} f^{6/5} cm^2 s^{-1} \tag{1.23}$$

The expression for radial velocity of the material in the disk is given as,

$$\upsilon_R = -\frac{3\nu}{2R}\left[1 - \left(\frac{R_*}{R}\right)^{1/2}\right]^{-1}$$

Substituting ν from eq. (1.23),

$$v_R = -4.1 \times 10^4 \alpha^{4/5} m^{-1/4} \dot{M}_{16}^{3/10} R_{10}^{-1/4} f^{-14/5} cm\ s^{-1} \tag{1.24}$$

The expressions obtained for temperature, volume density, surface density, and scale height give their functional dependence on mass, accretion rate and radius. It is clear from eq. (1.22) that the disk is indeed optically thick as $\tau >> 1$, and hence it radiates as a black body. Also, eq (1.19) shows that the temperature of disk increases inwards, which implies that the inner regions of the disk contribute significantly as compared to the outer regions. In the next section, we discuss the observed properties of these accretion disks around black holes in the binary systems.

1.5 X-ray emission and the properties of black hole binaries

Viscous forces in the accretion disks extract energy from the accreted material before it reaches the Innermost Stable Cirucular Orbit (ISCO), beyond which the stable Keplerian orbits are not present. In the case of zero-stress boundary condition, the material plunges onto the black hole irretrievably with the remaining energy. The energy lost by the accreted material in the accretion disk appears in the form of X-ray emission, winds and jets. Hence, the X-ray emission is only a proxy of the total mass accretion rate. In the present study, X-ray emission from black hole sources has been studied and their properties are discussed below.

1.5.1 Spectral properties

The X-ray spectral studies have revealed the presence of two major components in the spectrum; a thermal component and a high energy tail. The thermal component is believed to originate from the cool, optically thick and geometrically thin accretion disk and is generally referred to as 'accretion disk component'. The thermal component is generally fitted with a multi-temperature black body which has temperature as a function of disk radius. The component peaks around

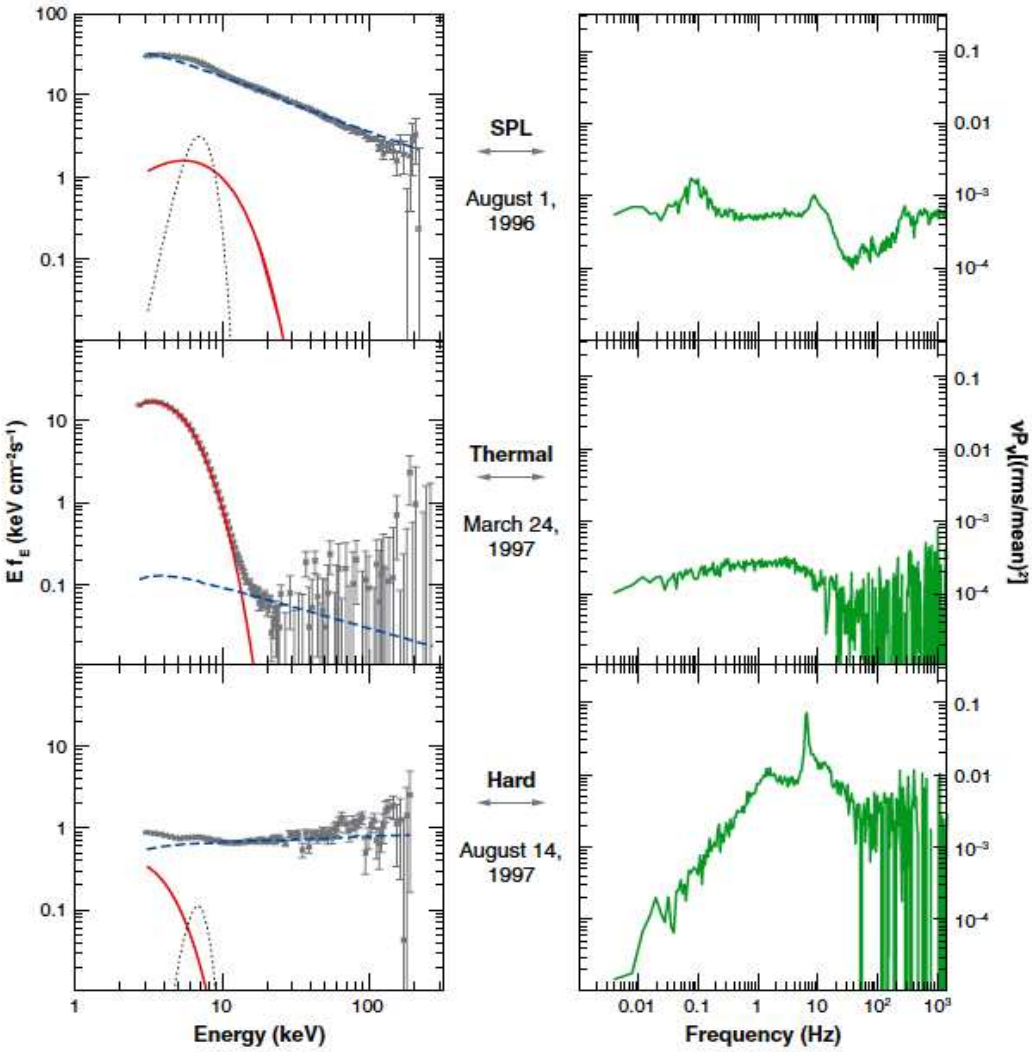

Figure 1.2: Different spectral states and the corresponding power density spectrum of a black hole binary GRO J1655-400. Spectra from steep power law, soft state and hard states are shown in first, second, and third panels respectively. Grey points show the total observed spectrum and the contributions of disk component (red solid line), power law component (blue dashed line) and the iron line are shown in each of the panels. Adapted from RM06.

∼1 keV and it dominates towards lower energies. An example of the observed spectrum for the black hole binary GRO J1655-40 is shown in Fig (1.2) for three different observations. The red solid curve in all the three panels represent the soft disk component. `DISKBB` (Mitsuda et al., 1984) and `DISKPN` (Gierliński et al., 1999) are the most frequently used non-relativistic models to explain the disk component, while the latter one is the modification of the former.

The second major spectral component, a higher energy tail, extends to hundreds of keV and it is generally fitted with a power law. This component is widely understood as a result of Compton upscattering of the soft disk photons by the high energy electrons in the corona (RM06). The component is often referred to as the Comptonization component. Other detailed models include `COMPBB` (Nishimura et al., 1986), `COMPST` (Sunyaev & Titarchuk, 1980), `NTHCOMP` (Zdziarski et al., 1996), as extended by Życki et al. (1999), `SIMPL` (Steiner et al., 2009b) and `COMPPS` (Poutanen & Svensson, 1996). The higher energy tail is shown with blue dashed lines in Fig (1.2).

Spectrum from a black hole binary shows another component which is the Comptonization component reflected from the accretion disk. This component appears as a reflection hump and/or fluorescence iron line in the X-ray spectrum. The most significant of this is the iron line found at ∼6.4 keV. The reflection component becomes particularly important for the brighter sources and for the sources observed at higher inclination angles. The line can be seen in Fig (1.2) plotted with black dotted line in the first and third panel. Modeling of a skewed iron line profile has been an important probe in the determination of spin of the black hole.

An interesting characteristic of the black hole binaries is the varying relative contribution of the two major components. This gives rise to the different shapes of spectrum and the concept of spectral states and their transitions.

Spectral states

(a) **Hard State**

At low luminosities, the spectrum is mainly dominated by the Comptonization component with a small contribution from the disk component. The broad band energy spectrum is relatively flat and the power law index is generally found in a range of $1.5 < \Gamma < 2.0$. This spectral state is called *hard state*. The power density spectrum (PDS) shows strong variability with fractional rms >30% (Belloni et al., 2011). An example of spectrum during hard states and the corresponding PDS is shown in Fig (1.2). Several spectral studies have revealed that the inner accretion disk is truncated at a higher radius during the hard states (e.g. Done & Zycki, 1999; Zdziarski et al., 2004; Tomsick et al., 2009; Cabanac et al., 2009; Done & Diaz Trigo, 2010; Shidatsu et al., 2011; Plant et al., 2015). It is noticeable that the hard states are not unique to low luminosities of black hole binaries as it can be observed at higher luminosities as well (e.g. Miller et al., 2015; Parker et al., 2015).

(b) **Soft State**

The spectral states, when the soft thermal radiation from the accretion disk dominates the spectrum, are observed at higher luminosities. This thermal dominant state, known as *soft state* exhibits a steeper spectrum with a power law index, $\Gamma > 2$. Power density spectra do not show prominent QPO feature superimposed on the continuum (Fig 1.2, middle right panel), although a broad and weak feature can be observed occasionally. The inner disk extends close to the black hole which may coincide with the ISCO. For this reason, spectrum of the soft states are helpful to put constraints on the spin of the black hole by measuring the inner disk radius.

(c) **Steep power law State**

Black hole binaries are sometimes observed in a *steep power law (SPL)* state wherein the power law component is generally very steep ($\Gamma \sim 2.5$). An observed spectrum and the corresponding PDS is shown in the first panel of Fig (1.2). There are similarities between soft states and SPL states as both of them have strong disk component and steeper power law component, however occurrence of QPOs is a distinguishing feature between the two states. QPOs are seen during SPL states in contrast to the soft states where QPOs are either absent or very weak. SPL states tend to occur as the luminosity of the source approaches the Eddington limit (RM06).

(d) **Intermediate State**

Apart from the two extreme cases of hard and soft states, there are two intermediate states called hard intermediate state (HIMS) and soft intermediate state (SIMS). The spectrum is softer and the variability in the PDS is less during HIMS than the hard states. In SIMS, the spectrum is softer and the fractional variability is less than HIMS. The threshold of fractional RMS and hardness for discrimination between HIMS and SIMS can be different for different sources (Belloni et al., 2011). A detailed description is given in Motta et al. (2011).

The occurrence of distinct spectral states can be explained with the disk truncation model which considers two types of accretion flows as evident from the spectrum. According to the model, when the mass accretion rate is high during soft states, the optically thick accretion disk extends to the inner regions. However, at low accretion rates, the inner edge of the optically thick disk is truncated at a larger radius and the inner flow is replaced by a hot and optically thin flow called advection dominated accretion flow (ADAF, Narayan & Yi, 1994). Different spectral states and the relative position of the inner disk radius can be seen in Fig (1.3) as a function of mass accretion rate.

1.5.2 Timing properties: short term behavior and QPOs

Black hole binaries are one of the highly variable sources in astronomy. Study of timing properties of these sources gives insight to the timescales of the processes in the disk and Comptonizing corona. Some of the tools for the study are power density spectrum, hardness-intensity diagram, time lag, cross correlation etc. PDS is the most frequently used for the quantitative study of the variability. The PDS for black hole binaries show quasi periodic oscillations superimposed on a band limited continuum (e.g. Fig 1.2 third right panel). A typical PDS from black hole binaries can be explained with multiple lorentzians; one centered at

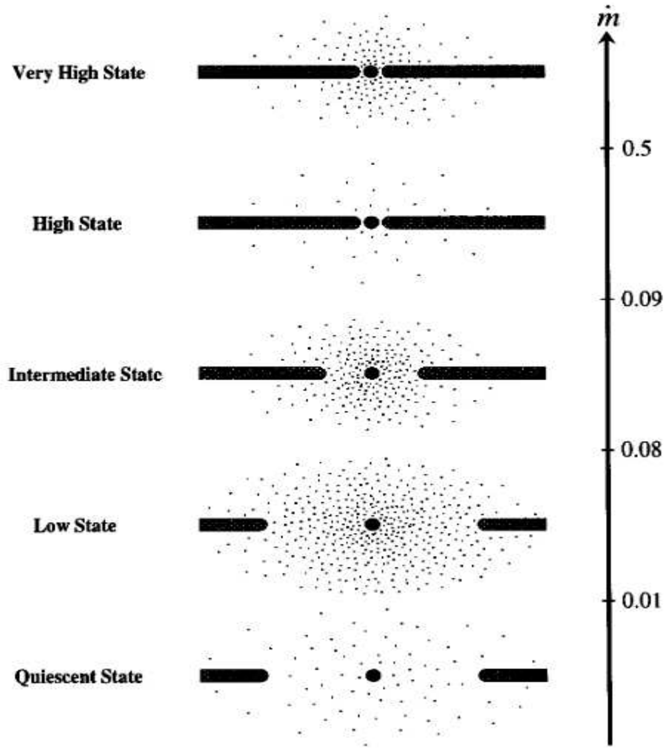

Figure 1.3: A schematic diagram showing qualitative description of accretion flow as a function of mass accretion rate. The horizontal bars show the thin accretion disk and the dots represent ADAF. The varying location of the inner disk radius for different spectral states is shown in the Figure. As the mass accretion rate increases, the disk extends inwards and it approaches ISCO. Adapted from Esin et al. (1997).

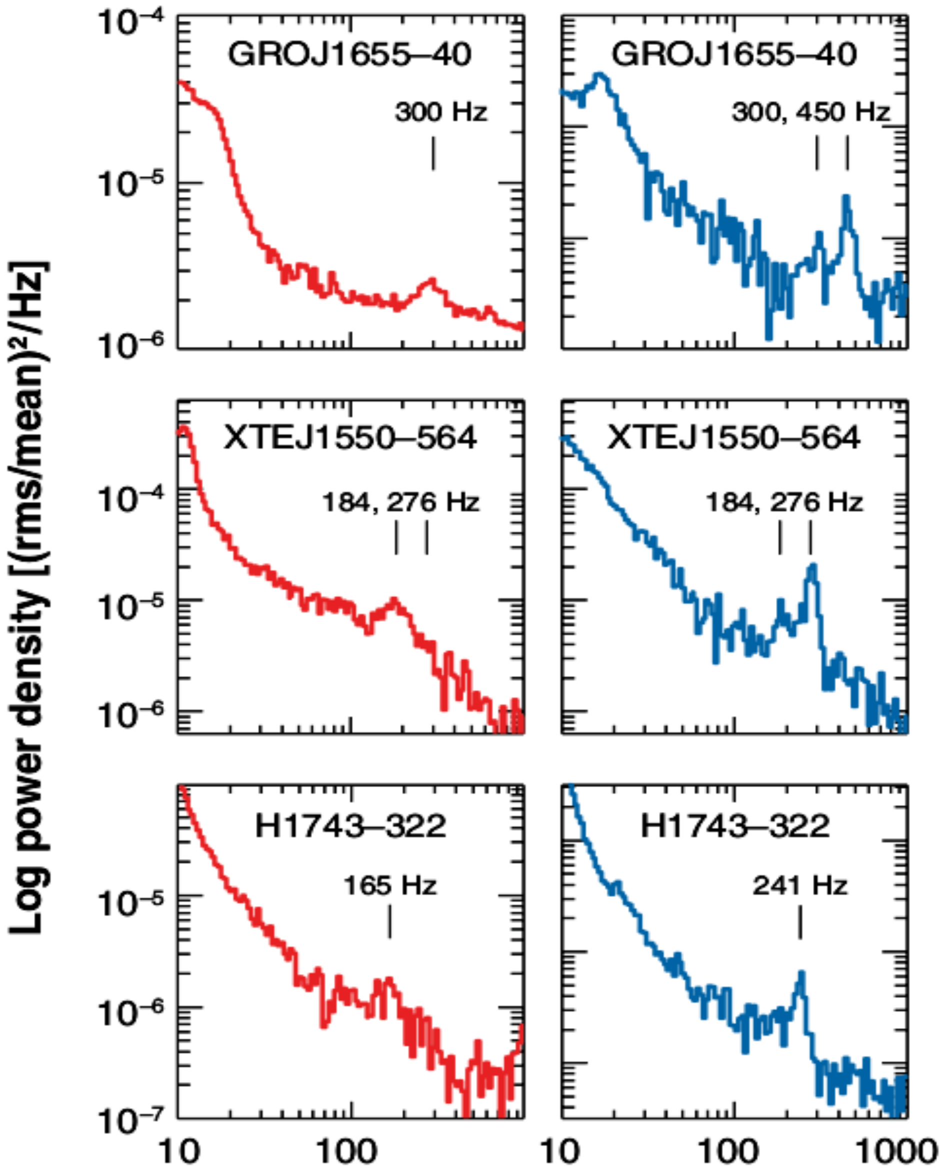

Figure 1.4: High frequency QPO observed from the three black hole binaries. PDS for the energy range of 13-30 keV and 2-30 keV are shown with blue and red respectively. Adapted from RM06.

the QPO centroid frequency and two broad lorentzians for the continuum. The lower and higher characteristic frequencies for broad lorentzians are called low and high frequency breaks respectively. QPOs have been classified into A, B and C type depending on their frequency, quality factor, and shape of the continuum (Casella et al., 2004). More details can be found in Motta et al. (2011). QPOs can again be classified as low frequency (0.1-30 Hz) and high frequency (40-450 Hz) based on the QPO centroid frequency. Although, the classification seems to be based on the range of frequencies, the two types of QPOs point towards different origins.

The LFQPOs are widely believed to originate in the Comptonizing medium and their properties have been observed varying with the spectral states of the black hole binaries. The frequencies of QPO centroid and low frequency break increases as the spectrum transitions from power law dominated hard state to the disk dominated soft state. The suggested mechanisms for QPOs includes Lense-Thirring precession (Stella & Vietri, 1998a; Wagoner et al., 2001a; Schnittman et al., 2006a; Ingram & Done, 2012) and disk instability models (e.g. Tagger & Pellat, 1999; Cabanac et al., 2010). These models explain successfully the power spectral properties of QPOs. A detailed study on a LFQPO observed in the black hole GRS 1915+105 has been discussed in the chapter (5).

In contrast to the LFQPOs, the frequencies of HFQPOs lie in the range of expected Keplerian frequencies of disk material in the innermost regions of the disk. These QPOs occur rarely and they do not shift freely in frequency with a significant change in the luminosity (factors of 3-4; Remillard & McClintock, 2006; Remillard et al., 2002, 2006). Fig (1.4) shows detection of HPQPOs in three sources. Generally, HFQPOs are weak and their detection is marginal, as observed in the figure. It is suggested that the HFQPOs are related to the black hole mass and spin. For a black hole with a well-constrained mass, HFQPOs offer an independent estimate of the black hole spin.

1.5.3 Transient nature: a long term behavior

Black hole binaries exhibit one of the most fascinating properties seen in the astronomical objects. A majority of the known low mass black hole binaries are transient in nature. The sources remain most of the time in the quiescence state where they are either very faint or below the detection limit of the instruments. The long quiescence, of typically a few years, is interrupted by outbursts where their brightness increases by orders of magnitude. The outburst state lasts typically for a few months and the source undergoes a cycle of spectral variation during a complete outburst. During quiescence states, the mass accretion rate and the temperature is low in the disk. As suggested by Jassal & Vadawale (2015), the inner edge of the disk remains truncated far from the central black hole. On the other hand, mass accretion rate and temperature is high when the source undergoes outburst. The disk extends close to the black hole and it may reach the innermost circular orbit.

Transient sources have shown different durations of the outbursts, amplitude, profiles and recurrence times. This is not only true when outbursts from different sources are compared, but this also holds for the outbursts of the same source (see Fig 1.5). Many of the transient sources have shown only single outburst since their discovery. Another interesting fact about the transient sources is that the new sources are being discovered with time. However, only a handful of outburst have been recorded including all the transient black holes. A collective study of outbursts can reveal a lot of information in future with more number of transient sources and outbursts. The occurrence of transient outburst is explained with the Hydrogen Ionization Instability which takes place in the outer cooler regions of the disk (Lasota, 2001).

It is highly unpredictable when a transient source enters into the outburst state after a long quiescence. Therefore, the detection of transient outbursts requires special wide field monitors which keep on spanning most of the sky with a certain frequency and better sensitivity. The transient phenomenon and its unpredictability has made all sky monitors an inevitable part of X-ray missions. Several missions are equipped with such all sky monitors viz. All Sky Monitor

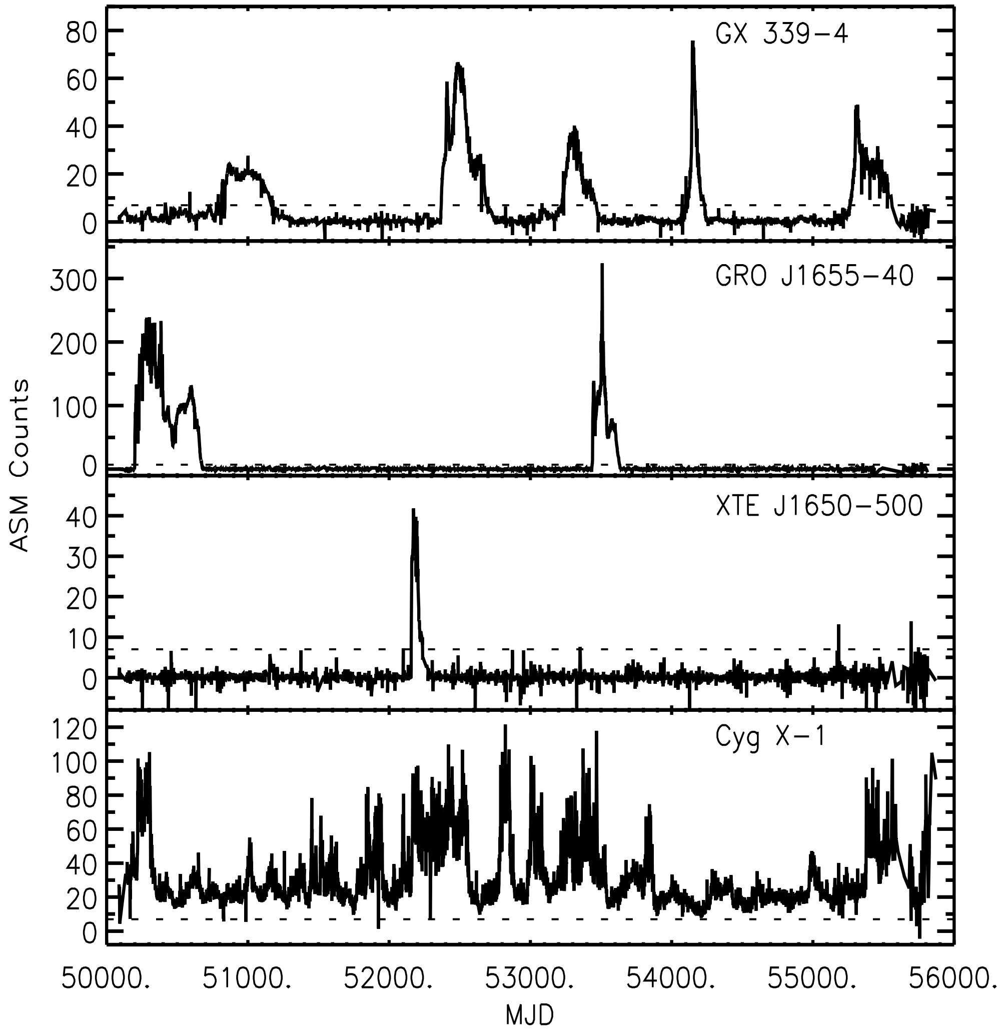

Figure 1.5: RXTE/ASM light curves spanning 16 years for three transient black hole binaries (GX 339-4, GRO J1655-40, XTE J1650-500) and a persistent black hole Cyg X-1. The dashed horizontal lines in the panels show the ASM counts corresponding to a brightness level of 100 mCrab. The spikes seen in the first three panels are the transient outbursts.

(ASM) onboard RXTE, Burst Alert Telescope (BAT) onboard Swift, and Monitor of All sky X-ray Image (MAXI) onboard International Space Station. The sensitivity of MAXI is about 10 times better than that of ASM which helps in the detection of new outbursts during early stages. The upcoming Indian X-ray mission ASTROSAT also consists of Scanning Sky Monitor (SSM) which would serve the purpose of an all sky monitor. X-ray astronomers are highly reliable on all sky monitors for the discovery of new transient sources and the detection of new outbursts from the known transient sources.

1.5.4 Transient outburst and the spectral evolution

Instead of all the differences in profile, recurrence time and amplitude of the outbursts, almost all the black hole binaries have been showing a similar pattern of spectral evolution during the outbursts. This pattern is best demonstrated with the hardness-intensity (HI) diagram. One such diagram is shown in Fig (1.6), adapted from Belloni et al. (2011), which shows spectral evolution for the four outbursts of a confirmed black hole binary GX 339-4. The evolutionary stages trace a Q-shaped track in an anticlockwise manner. The four spectral states; low hard state (HS), hard intermediate state (HIMS), soft intermediate state (SIMS) and soft state (SS) are marked by 1, 2, 3 and 4 respectively in the figure. The source is in the hard state as it enters the outburst. The spectrum remains hard and its luminosity increases. The observations in these states congregate along a rightward vertical line in the diagram. As the luminosity increases, the source transitions to the HIMS and the observations are located along the horizontal line. The spectrum becomes softer than in the hard state. As the softening continues, the source enters in the SIMS where the spectrum is similar to HIMS, however timing properties are different (see Homan & Belloni, 2005; Belloni, 2010; Motta et al., 2011). The spectrum further evolves to the soft states and the observations are seen along a leftward vertical line. The spectrum becomes soft and it is dominated by the thermal component. This completes half of the cycle, and in the remaining half the source follows reverse transitions. As summarized by Belloni et al. (2011), the evolutionary stages are: HS-HIMS-SIMS-SS as the

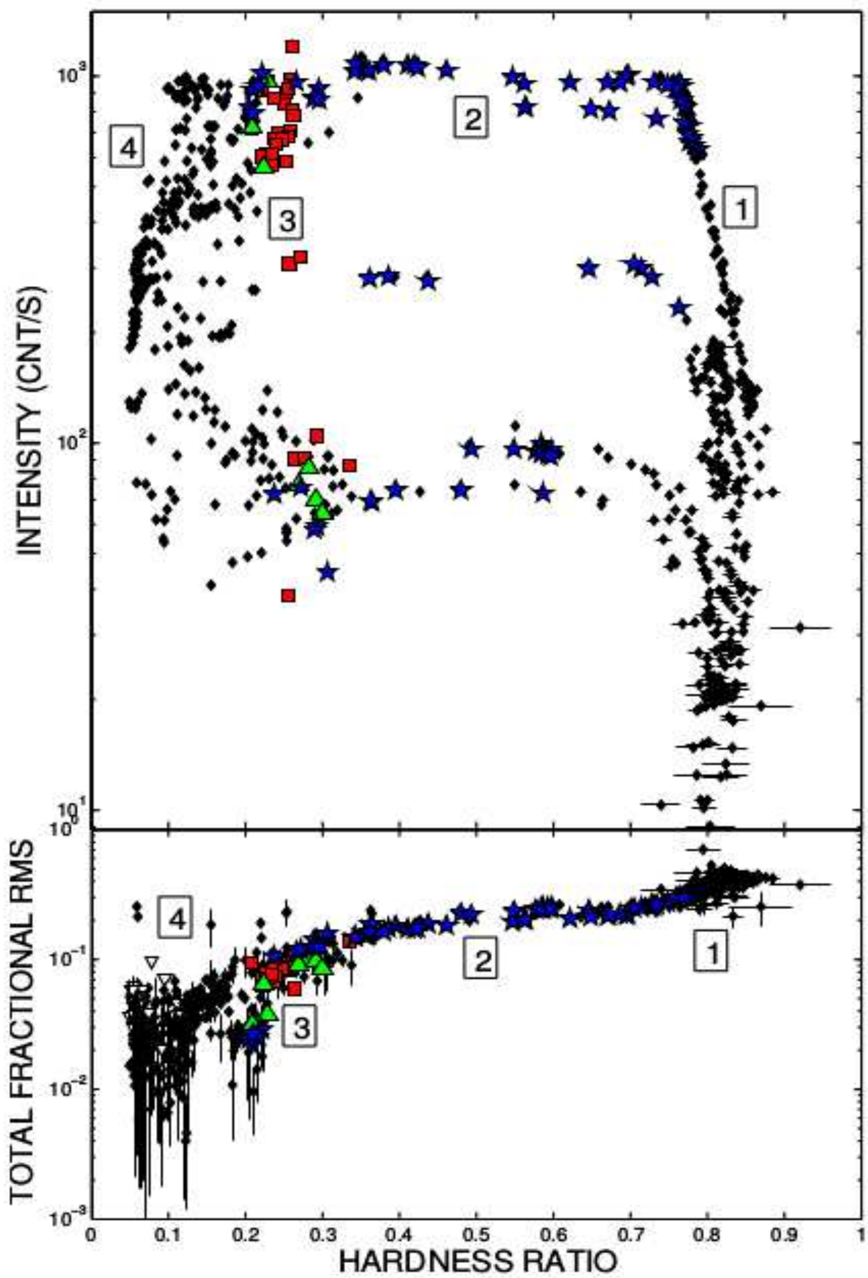

Figure 1.6: The top panel shows the hardness-intensity diagram plotted for the four outbursts (2000, 2004, 2007, and 2010) of GX 339-4. The bottom panel shows the rms-hardness diagram. Hard state, HIMS, SIMS and soft states are marked by 1, 2, 3 and 4 respectively. Black dots correspond to RXTE observations wherein no LFQPO was observed. Blue stars, red squares, and green triangles show the observation when Type-C, Type-B and Type-A QPOs respectively, were observed. Adapted from Belloni et al. (2011).

accretion rate increases, which is followed by SS-SIMS-HIMS-HS as the accretion rate decreases during an outburst.

In the present thesis work, two transient sources (IGR J17091−3624 and MAXI J1659−152) and a persistent source GRS 1915+105 have been studied. GRS 1915+105 is a unique source with several special properties, a few of which have been discussed in the next section.

1.6 The peculiar source GRS 1915+105

One of the most studied black hole binary, GRS 1915+105, was discovered on August 15, 1992 by WATCH onboard GRANAT (Castro-Tirado et al., 1992). The source appeared as a transient, however, it never switched to the quiescence since then. After radiating persistently for more than 20 years, the source is now considered as a persistent source. It is a confirmed black hole with an estimated mass of $12.4^{+2.0}_{-1.8}\ M_{\odot}$ (Reid et al., 2014) and a distance of $8.6^{+2.0}_{-1.6}$ kpc (Reid et al., 2014; Zdziarski, 2014). GRS 1915+105 is a legendary source with a number of unique properties. Mirabel & Rodríguez (1994) discovered GRS 1915+105 as the first Galactic source to show superluminal motion. Interpreting this phenomenon as relativistic jets, they found the bulk velocity of the ejecta of $\geq 0.9c$ at an angle of 60°-70°. Since its radio characteristic are similar to that of quasars, it is termed as 'microquasar'. Furthermore, GRS 1915+105 has an orbital period of 33.5 days which is longest of any known low mass black hole binary (Done et al., 2004). Its companion is a red giant (Greiner et al., 2001) and the black hole is believed to have a huge disk unlike other black hole binaries. It is believed to have a near extreme Kerr black hole with its spin parameter, $a_* \gtrsim 0.98$ (McClintock et al., 2006; Middleton et al., 2006; Miller et al., 2013).

The source has received immense attention of astrophysicists because of its extreme variability. RXTE observations of the source revealed that the source is highly variable at shorter timescales. Belloni et al. (2000) studied its variability patterns using RXTE/PCA data of 1996-1997 and classified its variability in 12 variability classes (Fig 1.7). These variability patterns are unique to the source

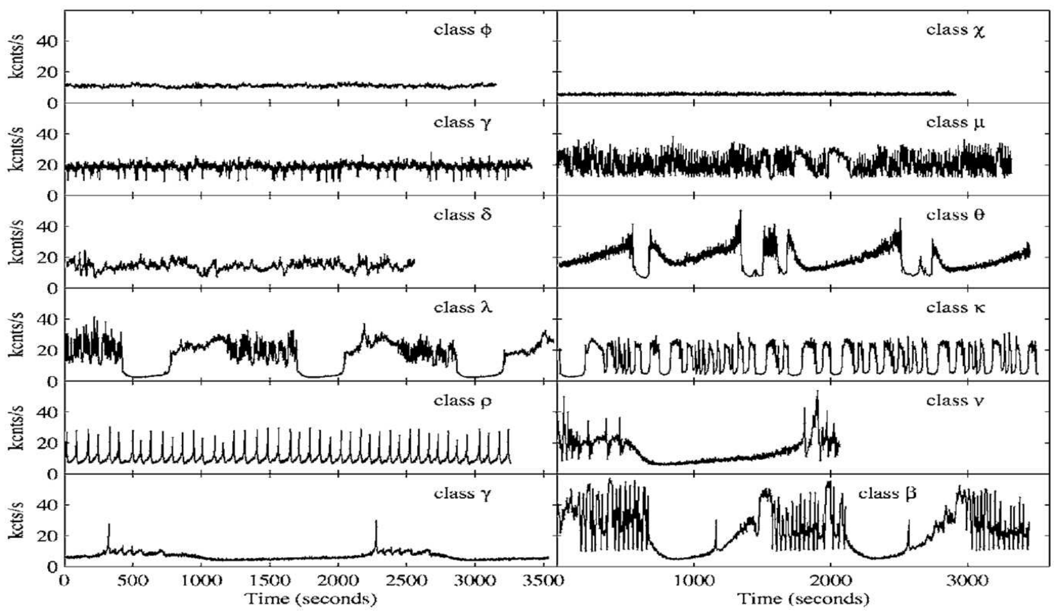

Figure 1.7: RXTE/PCA light curves binned at 1 second for the 12 variability classes as given by Belloni et al. (2000). The classes have been assigned greek letters shown in each of the panel.

(until 2011). Among the 12 classes, χ class is the most common variability pattern observed in the data. In order to understand its uniqueness, Done et al. (2004) studied GRS 1915+105 comparatively with the other black hole sources and found that it is similar to 'normal' black hole binaries in all aspects except the time it spends emitting close to the Eddington luminosity. While other black hole binaries emit at sub-Eddington luminosities and occasionally emit close to Eddington luminosity, GRS 1915+105 spends considerable time radiating close to the Eddington luminosity i.e. $L/L_{Edd} \sim 1$. The authors suggested that the high mass accretion rate is the trigger for the limit cycle variability uniquely observed in the source.

1.7 Outline of the thesis

Spectral evolution during an outburst and the occurrence of different type of QPOs during different spectral state clearly indicate that the temporal and spectral properties of black hole binaries are linked. Studies of both the spectral and temporal properties together are quite important as this can be a key to understand the link between the two set of properties. In the present thesis, both the properties have been studied using X-ray data from various space missions. The presentation of thesis is divided in six chapters and the outline is as follows:

- In **Chapter 1**, a brief description of accretion disks and mode of accretion is given. Timing properties of black hole binaries including QPOs and transient behavior are discussed. Spectral properties e.g. hard states, soft states, state transitions and spectral components are discussed in this chapter.

- A brief description of the missions of which data has been used in this thesis is given in **Chapter 2**.

- This is followed by a detailed study of 2010 outburst of a transient black hole candidate MAXI J1659−152 in **Chapter 3**.

- The work carried out to understand the quasi periodic 'heartbeat' oscillations along with the evolution of spectral parameters with the phases of 'heartbeats' for the two black hole sources GRS 1915+105 and IGR J17091−3624 is discussed in **Chapter 4**.

- **Chapter 5** describes our attempt to understand the QPO mechanism. A NuSTAR observation of GRS 1915+105 is studied in this work. Light curves are simulated by varying spectral parameters in different energy ranges. The simulated results are compared with the observed energy dependence of the QPO.

- Summary and future scope are discussed in **Chapter 6**.

Chapter 2

Instruments and Techniques

Many of the high energy phenomena in astrophysics are observed in sources that host compact objects, for instance, active galactic nuclei at the center of active galaxies, accretion onto white dwarfs, neutron stars or black holes in binary systems. Study of these sources requires detectors that are sensitive to the high energy photons emitted from the sources. However, the high energy radiation cannot be detected using detectors on the Earth's surface because our atmosphere absorbs high energy radiation. Half of the X-ray radiation from space is absorbed above a distance of about 100 km from the surface (see Fig 2.1). Therefore, it is essential to place detectors above the atmospheric layers. Balloons, rockets and satellites are generally used to lift X-ray detectors in order to observe the sources in X-rays. Although, balloons and rockets are short-lived programs and cost relatively less, satellites serve the purpose typically for a few years. In fact, several space missions have served for more than a decade e.g. RXTE, Suzaku, XMM-Newton etc.

The beginning of X-ray astronomy is marked by the discovery of the first X-ray source outside the solar system in 1962. The source is a neutron star Scorpius X-1 detected with Aerobee 150 sounding rocket. Since then, astrophysicists could unfold the mysteries of X-ray sky with a significant contribution from various X-ray observatories. The observational studies performed with the data collected by these missions have been very crucial in the discovery of several unknown phenomenon from X-ray sources. These observatories are mainly placed in the low Earth orbits. Einstein, Ginga, GRANAT, and RXTE are some of the past missions, however Chandra, XMM-Newton, Swift and NuSTAR are some of the currently active missions. The instruments onboard these observatories have different angular resolution, spectral resolution, timing resolution, sensitivity and energy coverage, hence they have contributed differently. While observing a particular source, the simultaneous data from different missions compliment each other (see Table 2.1). The data from several past and current missions can be availed from NASA's public archive HEASARC (High Energy Astrophysics Science Archive Research Center). The present work utilizes the data from the four missions viz. NuSTAR, RXTE, Swift, and XMM-Newton. The following sections give a brief description of these missions.

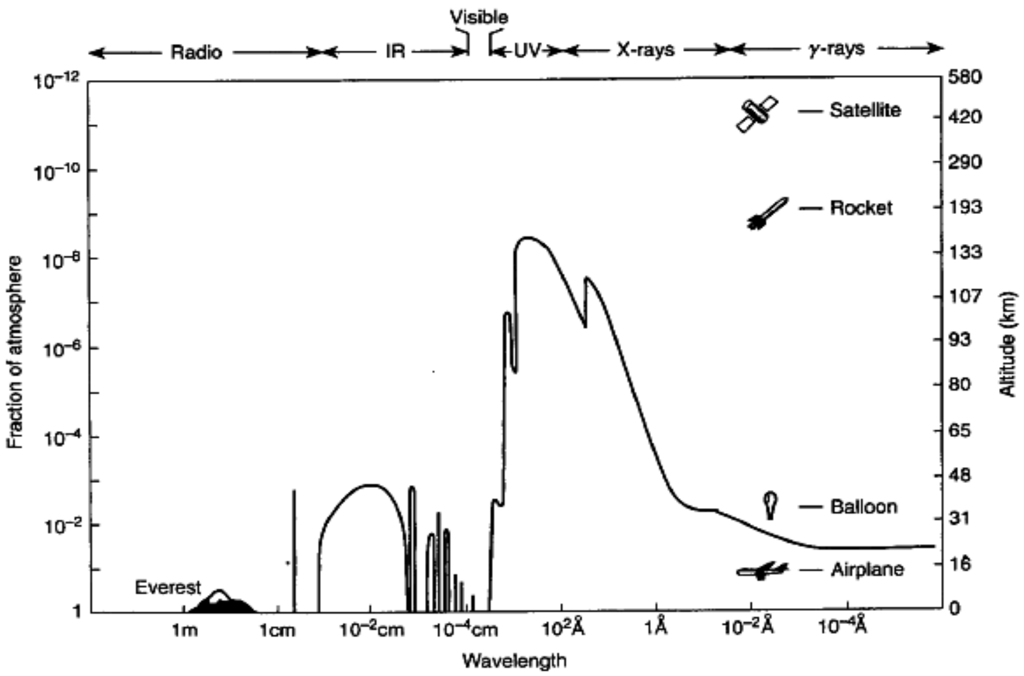

Figure 2.1: Figure shows the transmission of electromagnetic radiation through Earth's atmosphere. The solid line shows the altitude by which half of the radiation is attenuated. Most of the X-rays are absorbed above ∼100 km from the surface. Rockets and satellites are necessary to observe X-rays from astrophysical sources. Figure adapted from 'Exploring the X-ray Universe' by F. D. Seward & P. A. Charles.

2.1 Rossi X-ray Timing Explorer

Rossi X-ray Timing Explorer (RXTE, Bradt et al., 1993) is widely accepted as a historical mission for its tremendous contribution mainly in the study of timing properties of X-ray sources. It was launched on December 30, 1995 into a low Earth circular orbit at an altitude of 580 km and 23° inclination. The orbital period was about 90 minutes. After 16 years of successful performance, it was decommissioned on January 05, 2012. It has three non-imaging instruments onboard: Proportional Counter Array (PCA), High Energy X-ray Timing Experiment (HEXTE), and All Sky Monitor (ASM). A schematic diagram of the spacecraft showing all the instruments is given in Fig (2.2). PCA and HEXTE take pointed observations of sources, whereas ASM is a wide field monitor. PCA has the capability of detecting photons with microsecond accuracy. Also, it has larger collecting area, therefore adequate number of photons are collected per unit time. These two properties of better timing accuracy along with a larger collecting area make PCA the best instrument of its time to study timing behavior. A brief description of the instruments is given here.

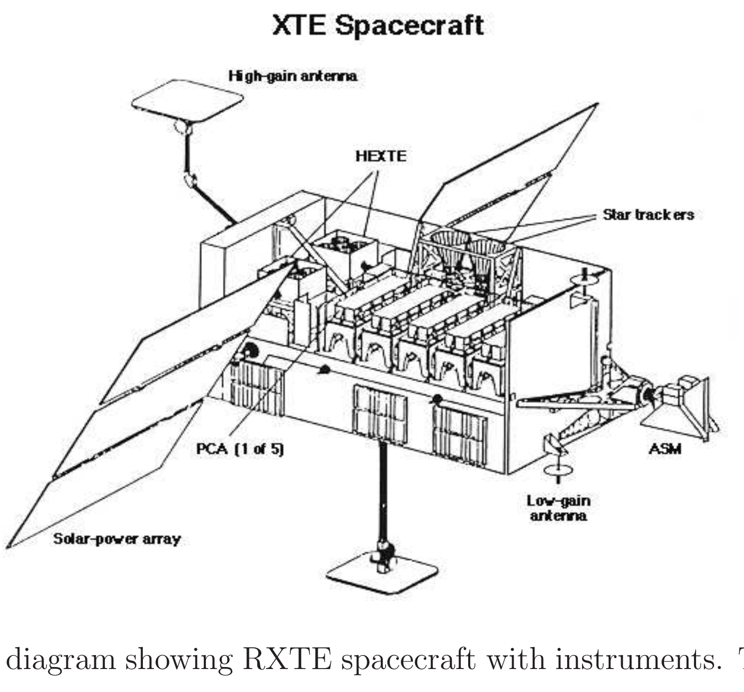

Figure 2.2: A diagram showing RXTE spacecraft with instruments. The five proportional counter units, two HEXTE clusters and ASM camera are shown in the diagram. Adapted from http://heasarc.gsfc.nasa.gov/docs/xte/xte_images.html.

2.1.1 Proportional Counter Array

As the name suggests, Proportional Counter Array (Jahoda et al., 1996) consists of five nearly identical gas filled proportional counters. Each counter is called Proportional Counter Unit (PCU), which has an effective area of about 1300 cm^2, thereby giving a total effective area of about 6500 cm^2 of PCA. These counters are sensitive over an energy range of 2-60 keV with an energy resolution of 18% at 6 keV. Each counter has a layer of propane and three layers of xenon with 10% methane. The propane layer serves as an anti-coincidence detector for the xenon layer to filter out the background events. There is a collimator for each PCU, which provides a field of view of $1°$ FWHM. Since PCA is a non-imaging detector, its background for any observation is calculated with models provided by PCA instrument team. PCA offers very good timing accuracy and moderate spectral resolution.

PCA dadta is available in different modes. Data in Standard 2 configuration is generally used to study spectrum. It provides 129-channel spectrum accumulated every 16 seconds. This mode does not allow spectral analysis with time bins smaller than 16 seconds. However, time resolved or phase resolved spectroscopy may require spectroscopy with finer time intervals and hence better timing resolution. Binned mode data is accumulated over shorter time intervals and hence it provides better time resolution as compared to Standard 2 data, however energy resolution is reduced. Event mode data contains information for individual events. It provides high time resolution, although it covers only a part of the whole PCA energy band. Good Xenon mode provides high energy resolution and high time resolution. This mode is useful in high time resolution analysis of fainter sources.

2.1.2 High Energy X-ray Timing Experiment

HEXTE (Rothschild et al., 1998) onboard RXTE consists of clusters of detectors named as cluster A and B. Each cluster has four NaI/CsI phoswich scintillation detectors. The two clusters can rock on and off source along mutually orthogonal directions in a way such that one is always pointed at the source while the other monitors the background. The clusters rock alternately to a total of four offset positions. It goes to a positive offset, then on source, then it goes to negative offset and again back on source. This completes a rocking cycle. Each cluster can rock up to 1.5° or 3° away from the source. The rocking feature enables HEXTE to perform realtime background measurements. It operates in an energy range of 20-200 keV with energy resolution of $\sim$ 15% at 60 keV. Therefore, HEXTE compliments PCA in terms of energy coverage by providing simultaneous observation in higher energy band. The two clusters have a total collecting area of about 1600 cm^2. The data from HEXTE are generally used for spectral studies.

2.1.3 All Sky Monitor

ASM (Levine et al., 1996) consists of three Scanning Shadow Cameras (SSCs), each consisting of a Position- Sensitive Proportional Counter (PSPC). The shadow patterns cast by X-ray sources help in finding their direction and intensity. The counters are filled with a mixture of 95% xenon and 5% CO_2 at 1.2 atmospheric pressure. Each SSC is sensitive in the energy range of 1.5-12 keV and the counts are recorded in the three energy range of 1.5-3, 3-5 and 5-12 keV. PSPCs view the sky through a slit mask which are divided into 6$\times$2 subsections. There are $\sim$15 open and $\sim$16 closed slit elements of size 1 mm $\times$ 110 mm arranged in a certain pattern in each of the 12 subsections. The field of view of each SSC is 6°$\times$90°. ASM data are available in the form of light curves in two modes: dwell by dwell and daily averaged. ASM data is of great importance in the long term monitoring of X-ray sources. Also, it is important for the detection of new outburst from known sources and detection of new transient sources.

2.2 X-ray telescopes

The high energy X-rays cannot be focused with conventional telescopes as they pass through the lenses without bending. Therefore, different techniques are used to focus X-rays. X-ray telescopes implement the concept of reflection of X-rays when incident at high incidence angles, called grazing incidence. Giacconi & Rossi

(1960) showed that the imaging with X-ray telescopes offers a significant reduction in noise from cosmic ray induced background. Most of the background counts are resulted from charged particles, which are uniformly distributed over the detector area. This is one of the major contribution of background in the large area proportional counters. Although, X-ray telescopes collect photons over a larger area, detection takes place over a very small area (a few pixels). This increases the signal to noise ratio and improves the sensitivity of the instrument. This property is not only important for point-like objects, but also for fainter and extended X-ray sources. Several X-ray observatories are equipped with X-ray telescopes e.g. Chandra, Swift, XMM-Newton and ROSAT. The present thesis uses the data of X-ray telescopes onboard Swift, NuSTAR and XMM-Newton. A brief description of these instruments is given here.

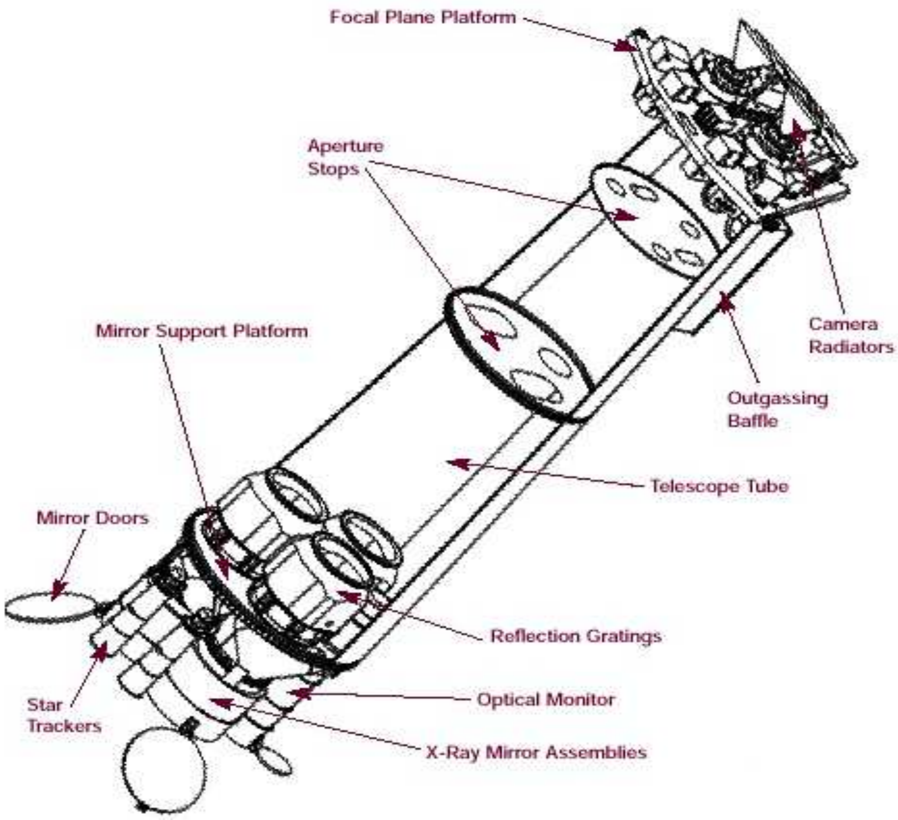

Figure 2.3: A diagram showing XMM-Newton spacecraft with instruments. The three telescopes can be seen in the left, with reflection grating array mounted on two of them. A PN and two MOS detectors are placed in the focal plane platform. Image Credit: ESA.

2.2.1 XMM-Newton

The XMM (X-ray Multi-Mirror Mission)-Newton observatory (Jansen et al., 2001) was launched on December 10, 1999 and after more than 15 years of successful performance the mission is still active. The observatory is placed in a highly elliptical orbit with an eccentricity of 0.78. Its 48-hour orbit inclined at 65° is relatively large which facilitates the functioning of the instruments outside the radiation belts. The apogee and perigee of the orbit are about 14,000 km and 7,000 km away from the Earth respectively.

The mission carries three X-ray telescopes each consisting of 58 nested mirrors for the reflection of X-rays. The nesting of mirrors increases the effective area of the instrument. Diameter of the largest and the smallest mirrors are 70 cm and 30.6 cm respectively. The instrument has a focal length of 7.5 m and there are three EPIC cameras in the focal plane: two EPIC-MOS (Metal Oxide Semiconductor) and an EPIC-PN. The two X-ray telescopes are equipped with the gratings of Reflection Grating Spectrometer (RGS) which diverts about half of the incident flux towards RGS detectors and about 44% of the incoming flux reaches the two EPIC-MOS detectors. However, EPIC-PN camera receives the unobstructed beam from the third telescope. The three telescopes and other instruments are shown in Fig (2.3).

EPIC cameras onboard XMM-Newton allow several modes of data acquisition. The three modes are 1) full frame and extended full frame, 2) partial window and 3) timing mode. In the full frame, all pixels of all CCDs are read out and the full field of view is covered. In partial window mode only a part of CCD chip is read out. For MOS, small window mode reads an area of 100x100 pixels and large window mode reads 300x300 pixels. However, in case of PN, the large window mode reads only half the area of all 12 CCDs and small window mode reads only the part of CCD0 quadrant 1 at the focal point. The timing mode allows imaging in one-dimension along the column axis. Along the row direction, data from a predefined area on onc CCD are collapsed inot a one-dimensional row to be read out at high speed. Burst mode of PN camera is a special case of timing mode, which offers very high time resolution. The data from XMM-Newton observatory has been utilized in this thesis in the study of IGR J17091−3624 along with RXTE data.

2.2.2 Swift

Swift (Gehrels et al., 2004) is mainly dedicated to the study of Gamma Ray Bursts (GRBs) and it is equipped with all the properties required to unfold this brief and powerful phenomenon. It is a multi-wavelength facility observing in gamma-ray, X-ray, ultraviolet and optical bands simultaneously. Swift has provided the most comprehensive study of GRBs. Its properties of better sensitivity and quick follow up make it important for the study of X-ray transients as well. The mission is still active after more than 10 years since its launch on November 20, 2004. It is orbiting in a low Earth orbit with an orbital period of about 95 minutes and inclination angle of 20.6°. The mission carries three instruments (see Fig 2.4) viz. Burst Alert Telescope (BAT), X-ray Telescope (XRT) and UVOT (Ultraviolet/Optical Telescope). For the study of the transient source MAXI J1659−152, the data were obtained from Swift/XRT and a description of the instrument is given here.

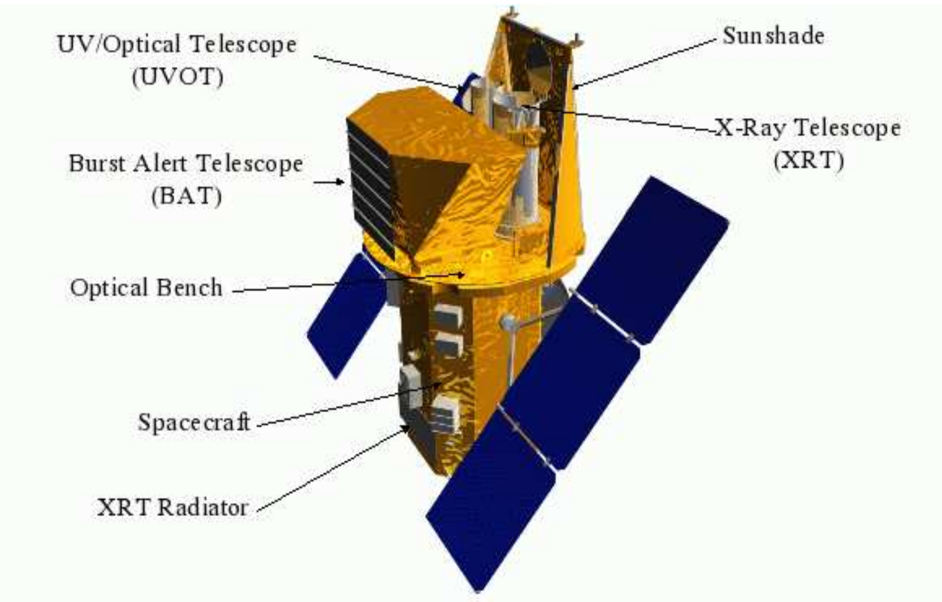

Figure 2.4: A figure showing Swift/XRT space mission with its instruments BAT, UVOT and XRT. Adapted from http://www.swift.ac.uk/about/instruments.php

X-ray Telescope (XRT)

XRT (Burrows et al., 2005) is an X-ray telescope onboard Swift. It uses a grazing incidence Wolter type 1 telescope to reflect X-rays. The mirror is composed of 12 nested mirrors with diameter ranging from 191 mm to 300 mm. The telescope has a focal length of 3.5 m and the X-rays are focused on a single MOS CCD placed in the focal plane. The effective area of the telescope is 110 cm^2 and its field of view is $23.6' \times 23.6'$. It operates in the energy range of 0.2-10 keV. XRT has capability of measuring position of a source with an accuracy better than 5 arcsecond within 100 s of receiving burst alert from BAT.

XRT can operate in different readout modes, which it can choose autonomously. This allows XRT to observe more than 7 orders of magnitude in flux. The four modes are: Imaging mode, Timing mode, Photon Counting mode, and Window Timing mode. Imaging mode can produce an integrated image with the total counts deposited per pixel in all energies. Hence, it produces better quality images at the cost of spectroscopic capability. It is useful to find the position of bright sources. Timing mode offers high time resolution through rapid CCD readouts. The mode has been disabled since a micrometeorite hit occurred on May 27, 2005 (see Abbey et al., 2006). Photon Counting mode is generally used only at very low flux levels. It offers full imaging and spectroscopic resolution, however the timing resolution is 2.5 s. Window Timing mode provides high timing resolution (2.2 ms). The mode is restricted to only 200 column window covering the central $8'$ of the field of view. Overall, XRT data is very helpful in the quick localization of sources and their spectroscopy in the lower energy band of 0.2-10 keV. Spectroscopic data in this band is very crucial in the study of thermal component of the disk blackbody in black hole binaries.

2.2.3 NuSTAR

Nuclear Spectroscopic Telescope Array (NuSTAR) was launched on June 13, 2012 and it is the first focusing high energy X-ray telescope in orbit (Harrison et al., 2013). All the focusing X-ray telescopes before NuSTAR are restricted to about 10 keV of energy coverage, however NuSTAR has dramatically extended it to 79

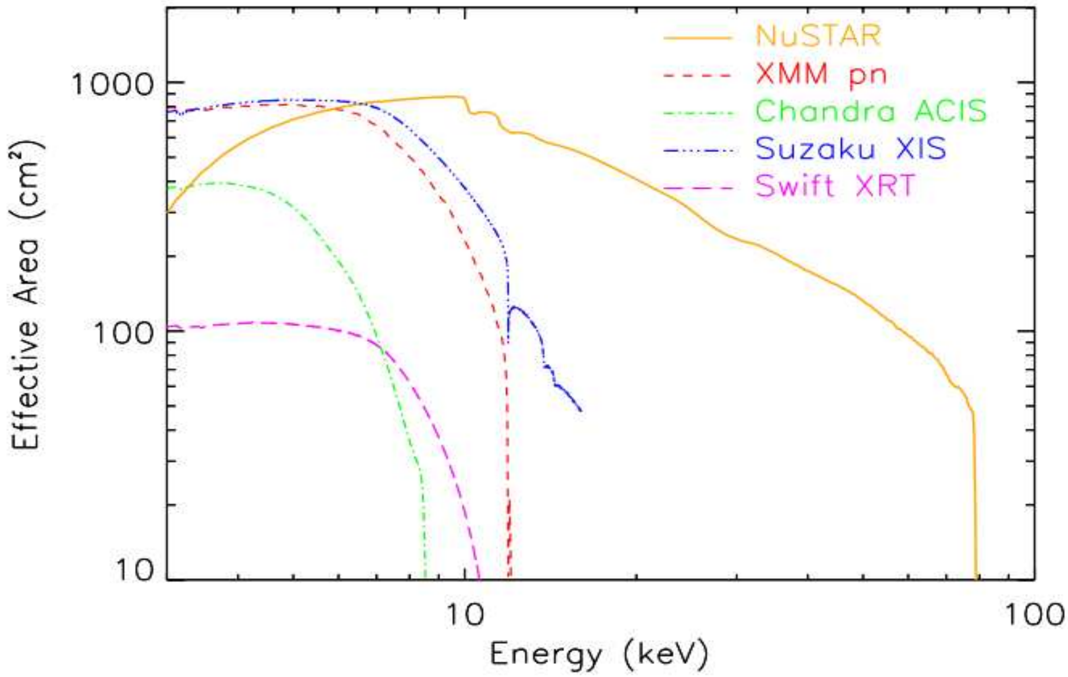

Figure 2.5: Effective collecting area from both the modules of NuSTAR as a function of energy. For comparison, the effective area of four other telescopes is given in the same plot. NuSTAR extends the focusing capability to 79 keV, however all the previous X-ray telescopes were limited to about 10-12 keV. Adapted from Harrison et al. (2013).

keV. It consists of two co-aligned hard X-ray telescopes. Each telescope consists of depth-graded and multilayer-coated nested shells to reflect X-rays. There are 133 concentric and confocal shells with a focal length of 10.14 m. The inner 89 shells are coated with depth-graded Pt/C multilayers and outer 44 shells are coated with depth-graded W/Si multilayers. This increases the graze angle, the angle between shell and incident X-rays, for energies >15 keV (see Fig 2.5), which helps in achieving significant reflectance at higher energy. The observatory has an angular resolution of 18″ FWHM and field of view is 10′.

In the focal plane of each of the telescopes, there are 4 hybrid hard X-ray detectors consisting of CdZnTe sensors placed in a 2×2 array. Each of the four detectors are segmented into 32×32 0.6 mm pixels. For any event, the onboard processors find the location of the pixel with the largest pulse height and read it out from this pixel and 8 neighbors. The event time is recorded to an accuracy of 2μs. The data is not affected by pile up until the source flux of $\sim10^5$ counts pixel^{-1} s^{-1} unlike CCDs. With the help of reflection from multilayer coatings and CdZnTe detectors, NuSTAR is capable of providing better sensitivity, spatial and spectral resolution.

Table 2.1: List of facilites from data of different missions

S. No.	Mission	Facilities
1	PCA Standard 2	1. moderate spectral resolution
		2. 129-channels
		3. binned at 16s, good for time-integrated spectroscopy
		4. available in all PCA observations
2	PCA Good Xenon	1. high time resolution
		2. 256-channels
		3. good for time resolved or phase resolved spectroscopy of fainter sources
3	XMM-Newton	1. low energy coverage (< 1keV), important for constraining

		disk spectrum 2. good spectral resolution (150 eV at 6.4 keV)
4	NuSTAR	1. Good spectral resolution (0.4 keV at 6 keV) 2. Goood timing resolution (0.1 ms) 3. Wider energy coverage (3-79 keV)
5	Swift	1. low energy coverage (< 1keV), important for constraining disk spectrum 2. quick follow-up observations

2.3 Data Reduction and Analysis

The data from RXTE come in two modes: binned mode and event mode. The binned mode data are already binned at a preselected time bin. Therefore, light curves form binned mode data are generated with timebins, which are multiples of the smallest binsize allowed by the mode. On the other hand, the event mode data has the capability of tagging each recorded event with the time of occurrence. Therefore, the data from event modes can be binned at desired value of binsize. The three other telescopes viz. Swift/XRT, XMM-Newton and NuSTAR provide data in event mode.

2.3.1 Screening

Data screening means the removal of data, which are not desired to contribute in the extraction of final science products. Data can be screened based on several parameters including altitude, orbital and instrumental parameters. For instance, it is required to reject the data during passage of South Atlantic Anomaly (SAA), wherein the highly charged particles trapped in the Earth's magnetosphere can give significant rise to background events. Generally, data is rejected by applying a constraint on time since the peak of SAA passage. Difference between source position and pointing of satellite known as offset is also an important parameter for screening. Data with offset beyond a certain value are rejected. Few other parameters e.g. elevation angle (angle between Earth's limb and target subtended by spacecraft), sun angle, moon angle and CCD temperature can be the parameters of interest to screen data. RXTE allows screening of data by applying screening criteria to create good time interval (GTI) file, which includes only the good data. This is done with the tools *xtefilt* and *maketime*. The GTI file is later used to extract science products. Data from Swift/XRT and NuSTAR is screened using their pipelines viz. *xrtpipeline* and *nupipeline* respectively to screen data. XMM-Newton data can be screened using sastask *evselect*. The screened data are used to generate science products for further analysis.

2.3.2 Extraction of Science Products

The final science products are light curves, spectra and images, which are used to learn about the sources. The products can be generated by applying criteria on count rates, time and energy in order to make best use of data and perform more meaningful analysis e.g. light curves generated in different energy bands or time intervals. Spectrum can be generated corresponding to certain features of interest observed in light curves. The other science products derived from light curves and spectra are hardness ratios, power density spectra, phase lags, hardness-intensity diagrams, color-color diagrams, cross-correlation etc. The two extractors for RXTE data are *saextrct* and *seextrct*, which are used to extract light curves and spectra from binned and event mode data respectively. The extraction of final products from Swift/XRT and XMM-Newton data requires the use of *xselect*, whereas NuSTAR products are generated with *nuproducts*.

2.3.3 XSPEC, Response, and Spectral Fitting

Energy spectrum extracted from data convey information about the radiative processes taking place in sources. The processes can be identified with the help of spectral study because each radiative process has a characteristic spectrum. However, the observed spectrum is not the actual spectrum emitted by the source. The observed spectrum is convolution of incident spectrum and detector response. As a result of detector response, photons of a given energy may redistribute over other energies. Therefore, the counts C recorded in channel I are given as,

$$C(I) = \int_0^{\infty} f(E)R(I,E)dE \tag{2.1}$$

where $f(E)$ and $R(I,E)$ are the incident spectrum and instrumental response respectively. Since incident spectrum cannot be found by inverting this equation, alternate ways are used to study energy spectrum of source. Generally, a model is chosen which is described in terms of a few parameters i.e. $f(E, p_1, p_2, ..)$ and convolve it with the response found experimentally and the predicted spectrum $C_p(I)$ is calculated. The best-fit model is found by changing the parameters $p_1, p_2, ...$ The fit statistics of χ^2 minimization is used to find the best fit quantitatively. `XSPEC` spectral fitting package available with HEASoft is used for this task in the work presented in this thesis. The package can be used to study spectral data from a number of X-ray observatories. `XSPEC` requires observed spectral file and detector response file in fits format to perform spectral fitting. It has a good number of models to describe the observed X-ray spectrum. Some of the most frequently used models to study spectrum from black hole binaries are multi-temperature disk blackbody (e.g. `DISKBB, DISKPN, KERRBB`), power law, cut-off power law, Comptonized emission (e.g. `COMPBB, COMPST, SIMPL`), lines (e.g. `LAOR`), reflection of Comptonized component (e.g. `PEXRIV, PEXRAV, REFLIONX, IREFLECT`) etc. `XSPEC` allows addition, multiplication and convolution of models to describe the observed spectra and to understand the interplay between different spectral components.

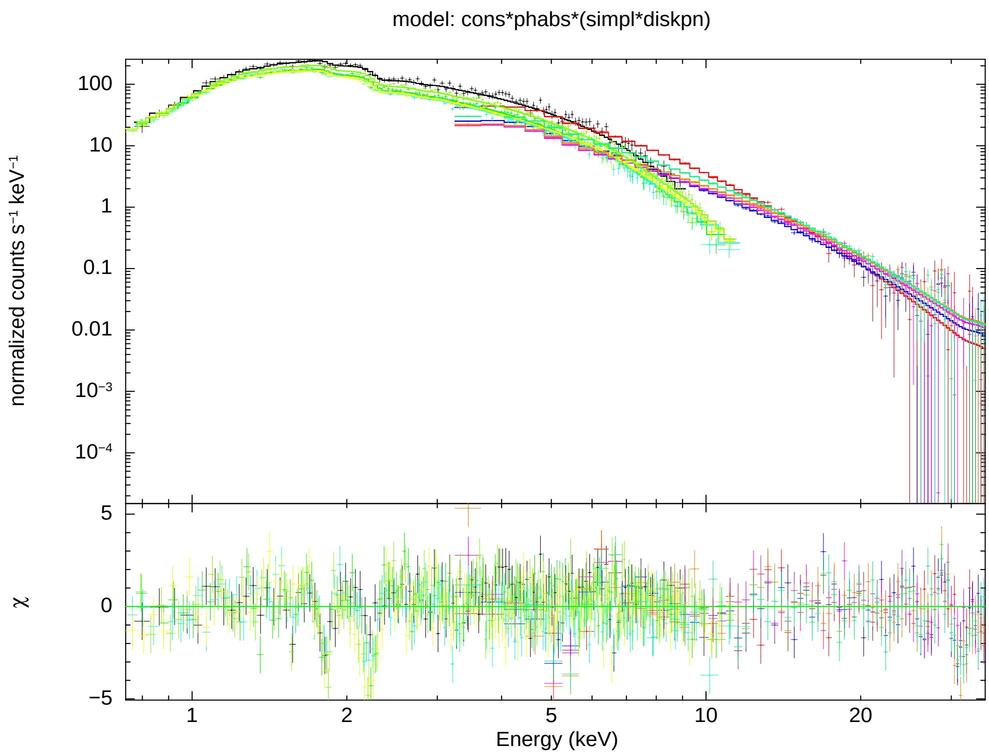

Figure 2.6: Spectra from RXTE and XMM-Newton for 5 phases of 'heartbeat' oscillations fitted simultaneously with the same model. Simultaneous fitting provides the energy coverage of 0.7-35 keV. The lower panel shows the reduced chi-square values.

2.3.4 Simultaneous Spectral Fitting

`XSPEC` allows fitting of more than one spectrum simultaneously with the same spectral model. Spectra have to be loaded as separate groups with respective response and background files. Simultaneous spectral fitting is generally used when the simultaneous observations of the same source are available from different instruments. Fitting of spectra of a source from instruments with different energy coverage helps to study spectrum over a broader energy range. An example is shown in Fig (2.6), where spectra from the two missions viz. RXTE and XMM-Newton are fitted simultaneously with the same model. XMM-Newton provides lower energy coverage of 0.7-9 keV, whereas RXTE/PCA covers 3-35 keV in the fitted spectrum. Method of simultaneous spectral fitting can also be used for observations of the same target at different epochs, while sharing some model parameters among the spectra. This can be helpful to understand variability in spectral components.

In the present thesis work, the method is used to study phase-wise spectrum of quasi periodic signals with a scheme of tying the spectral parameters across different spectra. Spectra from the same source and epoch, but different phases of oscillations were fitted together with the same model. Spectral parameters of a model were divided into two categories: accretion-process-dependent parameters and system parameters. The accretion-process-dependent parameters, e.g. temperature, inner disk radius, mass accretion rate, and spectral index etc not only change from one observation to the other, but also they are expected to change with phases of oscillations. Therefore, these parameters were allowed to take independent values while fitting spectra simultaneously. On the other hand, system parameters e.g. mass, spin, inclination angle and distance, are not expected to change with phases of oscillations and remain same for a given source. Therefore, these parameters were tied across spectra of different phases. Fig (2.6) shows spectra of five phases of 'heartbeat' oscillations fitted simultaneously. Figure shows the spectra obtained from the two observatories RXTE and XMM-Newton.

The simultaneous spectral fitting along with the above mentioned scheme of tying the parameters helps to get a tighter constraint on the values of parameters. The method has been frequently used in the study of black hole sources in the work presented in this thesis. The important results obtained using this method are discussed in the subsequent chapters.

Chapter 3

Variable Spectrum and the Inner Disk Radius

3.1 Introduction

Spectral studies of black hole binaries have revealed the presence of two major components in their spectra with variable contributions. The dominance of one component over the other gives rise to different spectral states. The occurrence of spectral states is generally explained in terms of the disk truncation model. Several empirical studies have found the inner radius of the disk component larger than the ISCO, which points towards the truncation of the inner disk. For example, Plant et al. (2014) compared the values of the inner disk radius for HIMS, SIMS and hard states and the truncation of the inner disk was observed for the hard states of the black hole GX 339-4 (Fig 3.1). Tomsick et al. (2009) studied RXTE and Suzaku observations of GX 339-4 and found $R_{in} > 35\ R_g$. The authors concluded that the inner portion of the disk is not present at low luminosities, which allows for the possibility of the replacement of the inner region by advection-dominated or magnetically-dominated accretion flows. The disk evaporation model is a widely studied model which explains the truncation of the disk at low luminosities. The model is discussed here briefly.

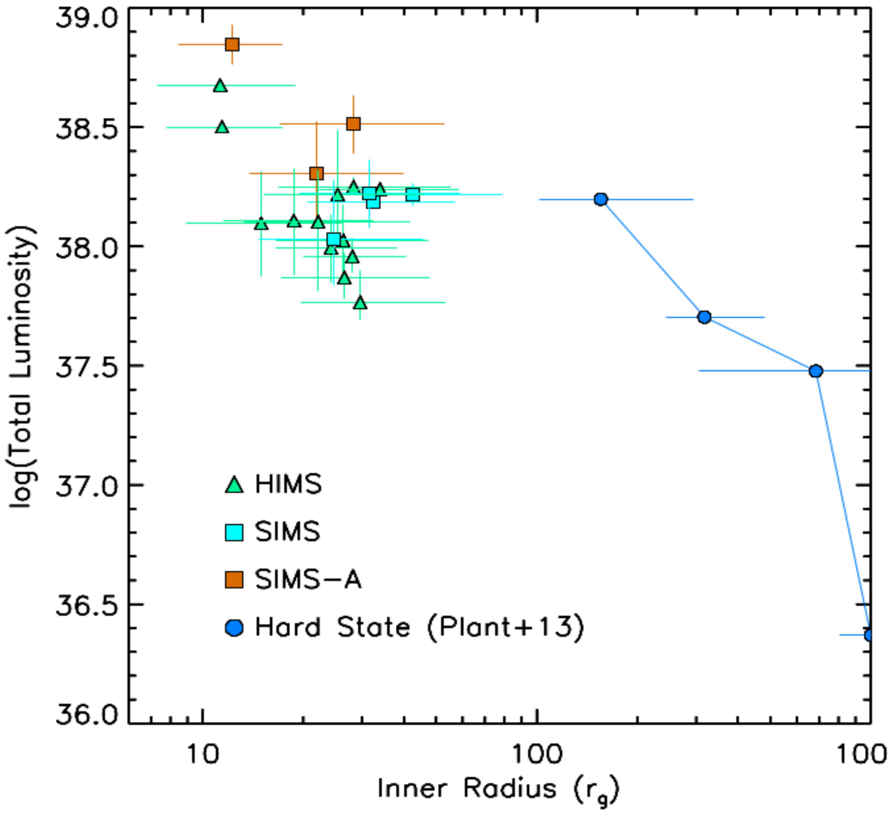

Figure 3.1: Measurements of the inner disk radius for HIMS, SIMS and hard states shown with triangles, squares and circles respectively. The figure shows the inner edge of the disk at a larger radius during hard states as compared to HIMS and SIMS. *Adapted from Plant et al. (2014).* The estimates of the inner disk radius during hard states are taken from Plant et al. (2013) in this figure.

3.2 Disk Truncation Model

The disk-corona evaporation model was first proposed by Meyer et al. (2000) and later extended by Liu et al. (2002) and Meyer-Hofmeister & Meyer (2003). The basic physics described in Qiao & Liu (2009) is summarized here briefly. The model considers a hot corona above a geometrically thin standard disk around the black hole in a binary. The lower regions of corona are cooler and denser. Viscous dissipation leads to ion heating in the corona which is partially transferred to electrons by Coulomb collisions. This energy is then conducted to the lower, denser and cooler corona. If the density is sufficiently high, the conductive heat is radiated away. On the other hand, if the density is low, the lower regions are heated up and evaporated into the corona. The mass evaporation continues until density equilibrium is established. The gas evaporated into the corona retains its angular momentum and rotates differentially around the central object. The frictional forces cause the gas to lose angular momentum and drift towards the central object. In this way, mass is continuously drained from the corona. This mass-loss from the corona is compensated by the steady evaporation flow from the underlying disk. In this way, heat is generated and radiated away by frictional forces and mass is accreted onto the central object. The accretion takes place in two ways:

(a) Partially through the corona (the evaporated part of the mass)

(b) Partially through the disk (part of the supplying mass which was not evaporated from the disk)

Qiao & Liu (2009) calculated the evaporation rate as function of disk radius (Fig 3.2). They showed that the evaporation rate takes a maximum values at a certain radius for a given value of viscosity parameter, and falls on both sides of that particular radius. In the inner regions, the evaporation becomes so efficient that all the accreted material in the disk is heated up and evaporated into the corona. The disk can survive the evaporation only when the accretion rate is higher than the evaporation rate. When the accretion rate exceeds the maximal evaporation rate (see Fig 3.2), the disk extends down to ISCO. This explains the smaller disk radius found during the soft states in observational studies. Truncation of disk will occur at a radius where the accretion rate is equal to the evaporation rate. Therefore, the disk is truncated during hard states as the mass accretion rate is low.

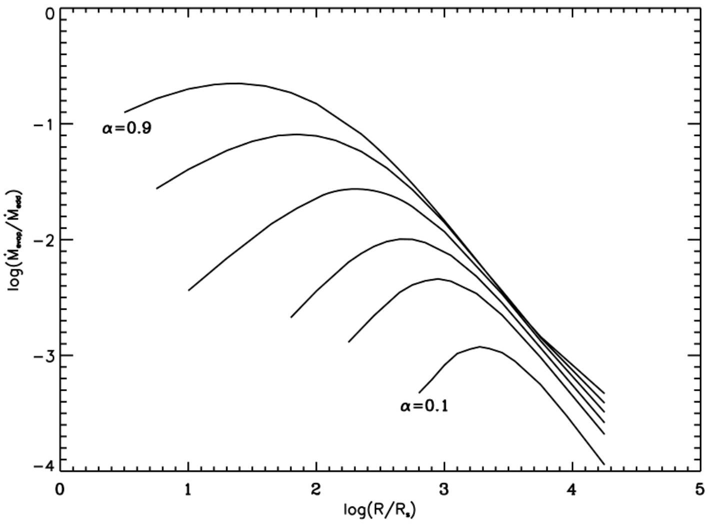

Figure 3.2: Evaporation rate as a function of disk radius. The accretion disk gets truncated at a radius where the accretion rate is equal to the maximal evaporation rate. Adapted from Qiao & Liu (2009).

3.3 Evidence Against the Disk Truncation Model

Although there are several lines of evidence in support of the truncation of accretion disk during hard states, few studies have presented observations which contradict the truncation model. Miller et al. (2012) found the inner disk radius at ISCO during the jet-producing low/hard state of Cyg X-1 (see more references therein). This led them to suggest that the truncation of the standard disk may not be required for relativistic jets. Reis et al. (2012b) studied a Suzaku observation of the black hole candidate MAXI J1836-194 and found the source to be in the hard/intermediate spectral state. A strong relativistically broadened iron line was observed in the spectrum, the study of which revealed the inner disk radius of $\sim 2.8\ R_g$. This shows that the disk is not truncated during the hard/intermediate state.

In another study by Reis et al. (2010), eight black holes in the low/hard state were studied and the thermal continuum following the relation $L \propto T^4$ was detected in all the sources at luminosities as low as $1.5{\times}10^{-3}L_{Edd}$. In six of the sources, spectral studies of the thermal continuum excluded the truncation of the disk beyond $10R_g$. Iron line was observed in five of the sources and its modeling excludes the truncation of the disk in all the five cases. Hiemstra et al. (2011) studied the black hole candidate XTE J1652-453 with simultaneous observations from XMM-Newton and RXTE. The observations belong to the hard/intermediate state during the decay of 2009 outburst. The broadened iron line was observed in the spectrum and the inner disk radius was found at $\sim 4R_g$ from the best fit. Other studies on the finding of the inner radius close to ISCO during low/hard state include Miller et al. (2006), Rykoff et al. (2007), Reynolds et al. (2010), Reynolds & Miller (2013), and Duro et al. (2011).

3.4 Inner Disk Radius During Transient Outbursts

The disk truncation model suggests that a disk is truncated during hard states as a consequence of low mass accretion rate. Therefore, it is generally assumed that the disk remains truncated during quiescent states of transient black hole binaries. Thus it is expected that during the onset of the outburst itself, the disk is truncated at a larger radius and it gradually moves in as the source transitions towards soft states. The observational evidence, showing the variation in the inner disk radius during very early stages of an outburst, is the best way to verify this concept. The early hard states of an outburst are difficult to be observed by detectors because of various reasons. Black hole binaries have X-ray luminosity of $L_X \lesssim 10^{-5}L_{Edd}$, (see Plotkin et al., 2015) during quiescence states. For a 10 $M_\odot$ black hole, this luminosity is of the order of 0.1 mCrab or less. Hence it is not detectable with the help of available X-ray detectors, for instance MAXI is sensitive to 1 mCrab for one week. When the source enters into an outburst, its brightness is low and it cannot be detected by the detectors until its luminosity reaches a significant fraction of its peak luminosity. Moreover, the source quickly switches to the hard intermediate state after early hard stages. Therefore, the early hard states are departed by the time the focusing detectors, preferably those with the energy coverage < 1 keV, point towards the source. This makes the observation of sources difficult during early hard stages of an outburst until recently with the availability of sensitive all sky monitors. An all sky monitor MAXI (Monitor of All sky X-ray Image) onboard International Space Station (Matsuoka et al., 2009), which has sensitivity almost ten times better than RXTE/ASM, is of great help in this regard. In order to harness the early detection of the source entering the outburst state, rapid follow-up observations are necessary, particularly with the focusing X-ray telescopes with energy coverage below 1 keV. NASA's Swift GRB mission (Gehrels et al., 2004), with its rapid follow-up capability using X-ray telescope (XRT), is providing valuable observations for the early stages of X-ray binary outbursts as well. MAXI J1659−152 is one such black hole binary source which was extensively followed up by Swift after the early detection of its 2010 outburst by MAXI. RXTE could start observing the source only after 3 days of the detection of the source. Fig (3.3) shows the densely sampled follow-up observations of the source. These pointed observations with low energy coverage provide a good opportunity to study the inner disk radius during early stages of outburst.

3.5 2010 Outburst of MAXI J1659−152

MAXI J1659−152 was detected both by Swift/BAT (Mangano et al., 2010) and MAXI (Negoro et al., 2010) when it entered into its discovery outburst on 2010, September 25. MAXI detected the source ~ 5.5 hours before the detection with Swift/BAT (Kennea et al., 2011; Kuulkers et al., 2013). It was first interpreted as a GRB (Mangano et al., 2010), however later it was confirmed as a black hole candidate (Kennea et al., 2011; Kalamkar et al., 2011) based on its spectral and temporal properties being similar to a black hole binary. The source is known for showing dips once every ~ 2.4 hours (see Kuulkers et al., 2013). If the dips

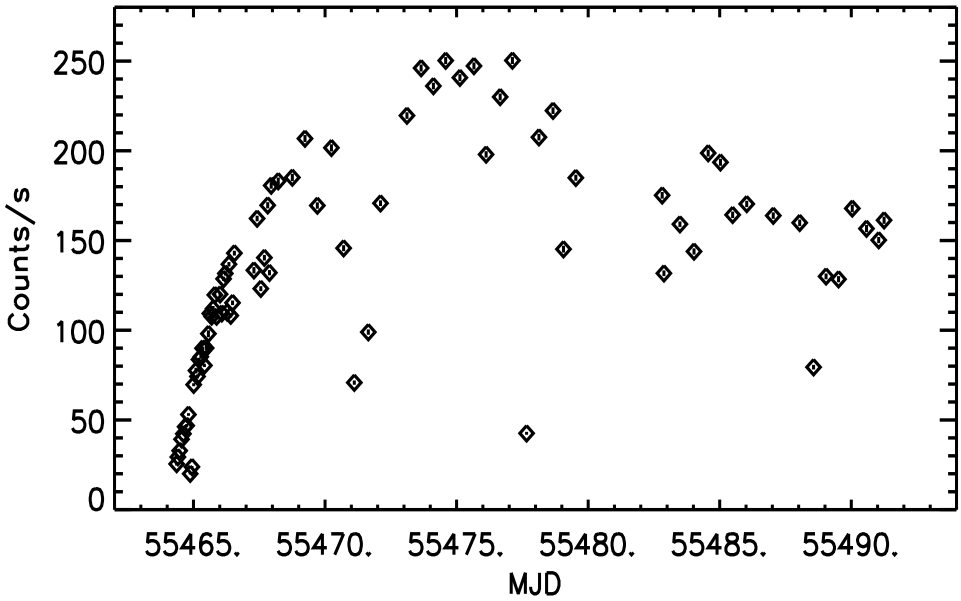

Figure 3.3: Swift/XRT coverage of 2010 outburst of MAXI J1659−152. Individual pointings are shown with diamond symbols. A very dense coverage can be seen during the early stages of the outburst.

are caused by the orbital motion of the secondary star, the source would be a black hole candidate with the shortest orbital period. The outburst, which lasted about one and a half months, has been extensively studied using observations from both Swift and RXTE missions and the results have been reported in Muñoz-Darias et al. (2011), Kennea et al. (2011), Kalamkar et al. (2011), and Yamaoka et al. (2012).

Muñoz-Darias et al. (2011) carried out spectral and timing analysis using energy and power density spectra obtained from RXTE/PCA. Assuming an orbital inclination of 70°, they found the inner disk radius to be constant at $\sim$ 40 km during the peak of the outburst with a possible decrease towards the later stages of the outburst. Kennea et al. (2011) found the inner radius of the disk to be decreasing along the outburst from the study of Swift observations of the source. Kennea et al. (2011) also suggested the inclination of the source to be in a range of 60°−75° owing to the absence of eclipses and the presence of dips in the light curves. In order to study the inner disk radius accurately, we preferred Swift data to RXTE data as Swift has energy coverage in a range where the disk radiation is dominant. Reanalysis of Swift observations of MAXI J1659−152 was carried out using the method of simultaneous spectral fitting of multiple observations while tying the geometry dependent parameters (e.g. black hole mass, binary inclination, distance, etc.), which are not expected to change across various observations (Rao & Vadawale, 2012). Also, the parameters related to accretion process are allowed to vary independently during the spectral fitting. This method is expected to provide a better estimate of the accretion-process-dependent parameters such as disk radius, temperature or mass accretion rate, because the uncertainty on the geometry dependent parameters is taken out to a large extent. It was found that the source was in the hard state during initial observations and the accretion disk was truncated at a large radius. Our results show that the inner disk radius decreases systematically as the outburst progresses and the spectrum becomes softer and ultimately it reaches the ISCO during the peak of the outburst. This is possibly the first observational confirmation of the general picture of black hole binary outburst evolution that it starts in the hard state with a truncated accretion disk and then the disk radius gradually closes in up to the ISCO.

Table 3.1: List of Swift observations of the black hole candidate MAXI J1659−152 during its 2010 outburst

S. No.	ObsId	Date of Observation (MJD)	Number of pointings
1	00434928000	55464.359	10
2	00434928001	55465.008	8
3	00431928002	55465.565	6
4	00434928003	55466.010	9
5	00434928005	55467.297	7
6	00434928007	55468.221	2
7	00434928008	55469.236	2
8	00434928009	55470.241	2
9	00434928010	55471.112	2

10	00434928011	55472.110	1
11	00434928012	55473.114	2
12	00434928013	55474.117	2
13	00434928014	55475.122	2
14	00434928015	55476.119	1
15	00434928016	55476.654	1
16	00434928017	55477.122	1
17	00434928018	55477.658	1
18	00434928019	55478.127	1
19	00434928020	55478.662	1
20	00434928021	55479.063	1
21	00434928022	55479.532	1
22	00434928023	55482.811	1
23	00434928024	55482.877	1
24	00434928025	55483.486	1
25	00434928026	55484.022	1
26	00434928027	55484.562	1
27	00434928028	55485.025	1
28	00434928029	55485.492	1
29	00434928030	55486.028	1
30	00434928032	55487.034	1
31	00031843001	55488.038	1
32	00031843002	55488.566	1
33	00031843003	55489.041	1
34	00031843004	55489.517	1
35	00031843005	55490.040	1
36	00031843006	55490.577	1
37	00031843007	55491.042	1
38	00031843008	55491.247	1

3.6 Observations and Data Analysis

We studied densely sampled observations of MAXI J1659−152 taken with Swift/XRT. Fig (3.3) shows the densely sampled observations and the relative brightness of the source. A total of 39 observations are available from NASA's public archive HEASARC with Swift/XRT. All the observations are in Window Timing mode except one observation which is taken in Photon Counting mode. This observation (ObsID 00434928004), taken on MJD 55466, helped in the accurate localization of the source (Kennea et al., 2011). The 38 observations in the Window Timing mode, listed in Table (3.1), were analyzed in our work. The data were reduced with *xrtpipeline* with the standard filtering and screening criteria for all the observations. The R.A. and DEC values of $16^h59^m01.679^s$ and $15°15'28.54''$, as obtained by Kennea et al. (2011) from UVOT data, were given to the pipeline. The first few observations are of longer duration with multiple pointings. Instead of generating spectrum for each of the observations, it was generated for each pointing. This resulted in a total of 80 spectra from 38 observations. The source and background spectra were generated with circular regions of 20 pixel radius. The spectra might be affected by pile-up. Although there is no direct way of determining the pile-up for XRT data, Romano et al. (2006) have suggested its removal based on the total count rate for the observation. Among the set of 80 observations, the count rate for a few observations are in the range of 150-300 counts s^{-1}. These observations might be affected by a moderate pile-up, which can be removed by ignoring the brightest pixel from the extraction region (Romano et al., 2006). Therefore, the source region was again generated with an annular region of 20 pixel outer radius, removing the inner brightest pixel. The source spectra were regenerated with the annular regions for the piled-up observations. The ancillary files were generated with the task *xrtmkarf*, corrected for hot columns and bad pixels along with PSF correction. The RMF files, necessary for the spectral fitting in `XSPEC`, were taken from CALDB as obtained from the task *xrtmkarf*. The spectra were grouped using *grppha* to obtain a minimum of 20 counts in each bin. The spectra were fitted in 0.7-9.0 keV energy range. The energy range of 1.7-2.5 keV was ignored in the spectral fitting due to the presence of large residuals in almost all the spectra.

3.7 Spectral Analysis

Spectrum from a black hole binary mainly consists of two components. One of them is a multi-temperature black body component, which originates from an optically thick, geometrically thin and cool accretion disk around the black hole. This component is generally fitted with the canonical model `DISKBB` (Mitsuda et al., 1984; Makishima et al., 1986). The model does not consider the zero stress inner boundary condition. The model has two fit parameters viz. temperature at the inner disk radius (T_{in}) and the normalization consisting of the inner disk radius (R_{in}), inclination (i) and distance (D) to the source. The presence of the inner disk radius in the expression for normalization makes it an accretion-process-dependent parameter, instead of the presence of two system parameters (i and D). Also, an accurate knowledge of distance and inclination is required in order to estimate the inner disk radius from the `DISKBB` normalization, which are not generally available for the new sources. There is an alternate model `DISKPN` to describe the multi-temperature disk component (Gierliński et al., 1999). The model calculates the spectrum of the disk by considering pseudo-Newtonian potential, unlike `DISKBB`, which is considered as a more accurate description of the gravitational potential in the vicinity of the black hole. In the context of the present work, an important aspect of the model `DISKPN` is that it has the inner disk radius as a separate fit parameter in the units of gravitational radius R_g. This facilitates the estimation of the inner disk radius without a priori knowledge of distance and inclination. There are other fully relativistic and hence more accurate models e.g. `KERRBB` to describe the disk spectrum. However, these models always assume that the inner accretion disk extends to the ISCO. Since we want to study the inner accretion disk radius, such models are not helpful to study the spectrum of a truncated disk. In this scenario, `DISKPN` is the most suitable model to describe the multi-temperature disk component. The normalization of `DISKPN` consists of geometry dependent parameters, apart from the color correction factor, which is generally assumed to be 1.7 in the literature. For this reason, normalization can be treated as a system parameter and thus it can be tied for different spectra in the simultaneous spectral fitting. This method leads to an independent estimate of the inner disk radius and a robust constraint on the normalization.

The second major component in the spectrum is the Comptonized component originating in the Comptonizing medium. The component is generally fitted with the power law as an approximation. Since the power law extends towards the lower energy, it results in underestimation of the disk component. The convolution model `SIMPL` (Steiner et al., 2009b) gives a more accurate description of the Comptonized component. This model calculates the Comptonization component by considering the inverse Compton scattering of a fraction of the disk photons.

All the spectra were fitted with the spectral model `PHABS*(SIMPL*DISKPN)`. The fitting of individual spectra with this model results in a rather poor fit with a larger confidence range for each of the spectral parameters and a larger range of `DISKPN` normalization. This also does not provide a consistent measurement of the inner disk radius. Although simultaneous spectral fitting can provide better constraints on the parameters, simultaneous fitting of 80 spectra is not feasible. Therefore, the 80 spectra were divided into 10 groups, such that each group has 10 spectra. The first two spectra in a group were the same as the last two spectra of the previous group. This step was required to create a link between the groups of spectra and thus avoid them being completely disjoint from one another. A schematic diagram illustrating the grouping of spectra is shown in Fig (3.4). Spectra in each group were fitted simultaneously with the same model and the values of `DISKPN` normalization were tied together. This eventually led to a tighter constraint on the `DISKPN` normalization. Since the last two spectra of nth group are same as the first two spectra of (n+1)th group, spectral parameters can be compared for these common spectra. It is found that the values of parameters are consistent for the two common spectra in the two groups. Since normalization is a geometry dependent parameter in this case, it can be tied across all the spectra. Putting two spectra common between the groups is used as an alternative way of tying normalization all the spectra. The maximum and minimum of the normalization values are selected to study detailed spectral variation which is shown in Fig (3.5).

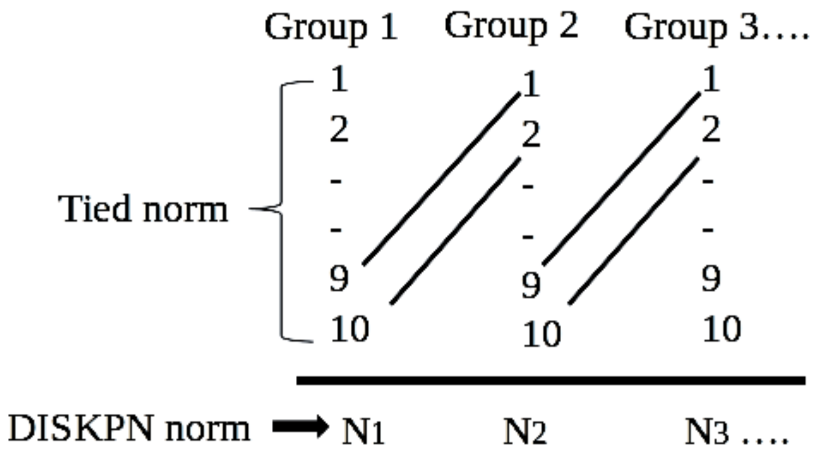

Figure 3.4: Schematic diagram showing grouping of spectra for simultaneous fitting. The first two spectra of a group were the same as the last two spectra of the previous group. Normalization of `DISKPN` was tied across the 10 spectra of a group.

Simultaneous fitting of spectra in 10 groups resulted in 10 values of `DISKPN` normalization. The maximum (3.26×10^{-2}) and the minimum (2.33×10^{-3}) values were selected for further analysis. Since the spectral fitting was not able to calculate errors for a few groups, individual spectra were fitted with the `DISKPN` normalization frozen at the maximum and minimum values and the errors were calculated for the spectral parameters. The spectral parameters obtained from the spectral fitting with the calculated error bars are shown in Fig (3.5) for both the values of normalization. The figure also shows the parameters obtained from the spectral fitting in groups. It is clear from the figure that the parameters obtained from the spectral fitting in groups and the fitting of individual spectra match very well. The error bars correspond to a confidence range of 90% for all the parameters.

All the spectra with the normalization frozen at the maximum and minimum values give statistically acceptable fit with the reduced χ^2 values below 1.26. Panels C and F of Fig (3.5) show respectively the variation of the inner disk radius (in units of gravitational radius) and the power law index with time. It is clear from the figure that the inner disk is truncated at a larger radius during the start of the outburst, when the spectrum is harder. With the progress of the outburst, the source becomes softer and the inner disk radius gradually decreases. This result is consistent with the results of Zdziarski et al. (2004), where the authors have studied the two outbursts of the black hole GX 339-4 and found the inner disk to be at a larger radius during the hard states than during the soft states. Done & Zycki (1999) have also shown that the disk is truncated at a few tens of Schwarzschild radii during the hard states of the black hole Cyg X-1.

3.8 Results

Black hole sources are known for exhibiting different spectral states with the evolution of an outburst. The definition of spectral state depends on the relative contribution of the two major components of the spectrum viz. the accretion disk component and the Comptonization component. In the soft states, the disk component dominates and the disk extends close to the ISCO. In the hard states, the contribution from the disk component is less or negligible and the spectrum is dominated by the Comptonization component. The inner disk is believed to be truncated at a larger radius during the hard states. In our work on MAXI J1659−152, we found that during the beginning of the outburst, the disk is truncated and the source is in the hard state. This result is consistent with the general understanding of the spectral states in black hole binaries. This confirmation of the general picture has become particularly important given that there have been a few recent studies contradicting the general picture of hard states (Reis et al., 2012b, 2010; Hiemstra et al., 2011), wherein the hard state spectrum is modeled as being dominated by the reflection component, thus implicitly assuming the presence of the disk close to the black hole. In fact, some studies (e.g. Miller et al., 2013) model the spectrum with the power law and reflection component while completely ignoring the disk component, which would not be physically appropriate. Thus our present results reinforce the general

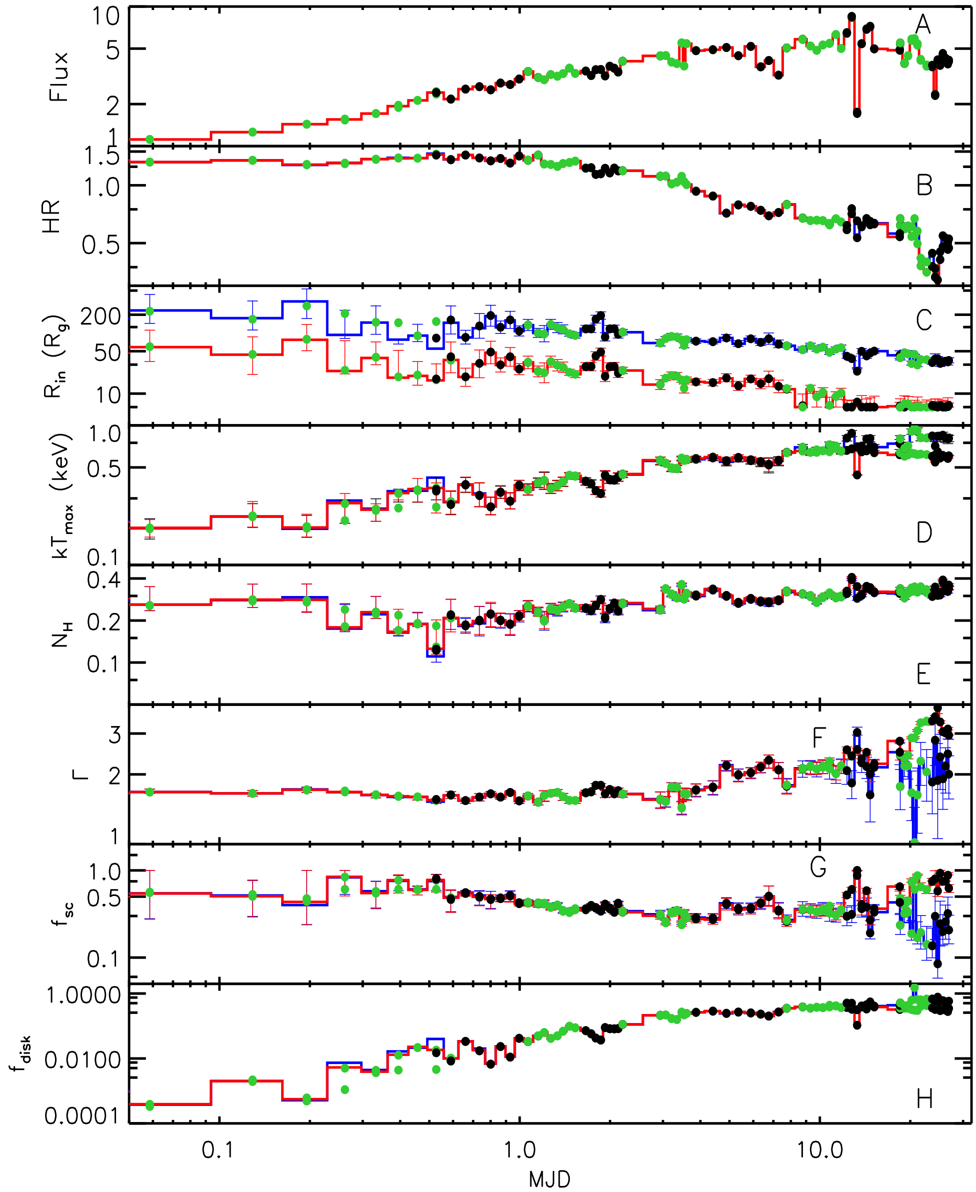

Figure 3.5: A multi-panel plot showing the evolution of spectral parameters with the progress of the outburst. Red and blue solid lines correspond to the parameters obtained by freezing the normalization of `DISKPN` to its maximum and minimum values respectively. The parameters obtained from the spectral fitting in groups have been over-plotted with filled circles. Green and black circles have been used alternatively to differentiate parameters used for neighboring groups. Adapted from Jassal & Vadawale (2015).

understanding that the accretion disk is truncated in the hard state.

3.8.1 Evolution of Spectral Parameters

The values of the inner disk radius for the maximum and minimum values of `DISKPN` normalization are shown in two separate panels in Fig (3.6) because the obtained values of the inner disk radius differ in the two cases. A systematic decrease in the inner disk radius is evident from both the panels in Fig (3.6). Since the values of the inner disk radius for the maximum normalization are smaller than those values corresponding to the minimum normalization, the inner disk radius in the former case reaches the minimum value of 6 R_g as allowed by the model `DISKPN` towards the later stages of the outburst. The model `DISKPN` does not allow values smaller than 6 R_g as it uses the Schwarzschild metric. The dotted horizontal line in second panel of Fig (3.6) correspond to the inner disk radius of 6 R_g.

The absorbed total energy flux is displayed in Panel A of Fig (3.5) in units of 10^{-9} ergs s^{-1} cm^{-2}. The hardness ratio, defined as the ratio of the energy flux in 5-12 keV to the energy flux in 2-5 keV, is shown in Panel B. The inner disk radius R_{in} and the maximum temperature kT_{max} are shown in Panels C and D respectively. The figure shows that the inner disk radius was truncated far from the black hole during the beginning of the outburst and the maximum temperature in the disk was low, which increases slowly as the outburst progresses. During the entire outburst, the maximum temperature was found in a range of 0.11-0.97 keV, including error bars. The variations in N_H, which was allowed as a free parameter in the simultaneous spectral fitting, are shown in Panel E in units of 10^{22} cm^{-2}. The value of N_H is found close to 0.3×10^{22} cm^{-2} during the entire outburst, although small fluctuations can be seen in the figure. Evolution of power law index is shown in Panel F, which shows that the spectrum was hard in the beginning of the outburst and it softens as the outburst progresses. The values of the power law index obtained for the maximum and minimum normalization are close except towards the end of the outburst. The power law index corresponding to the maximum normalization is well constrained and shows significant softening

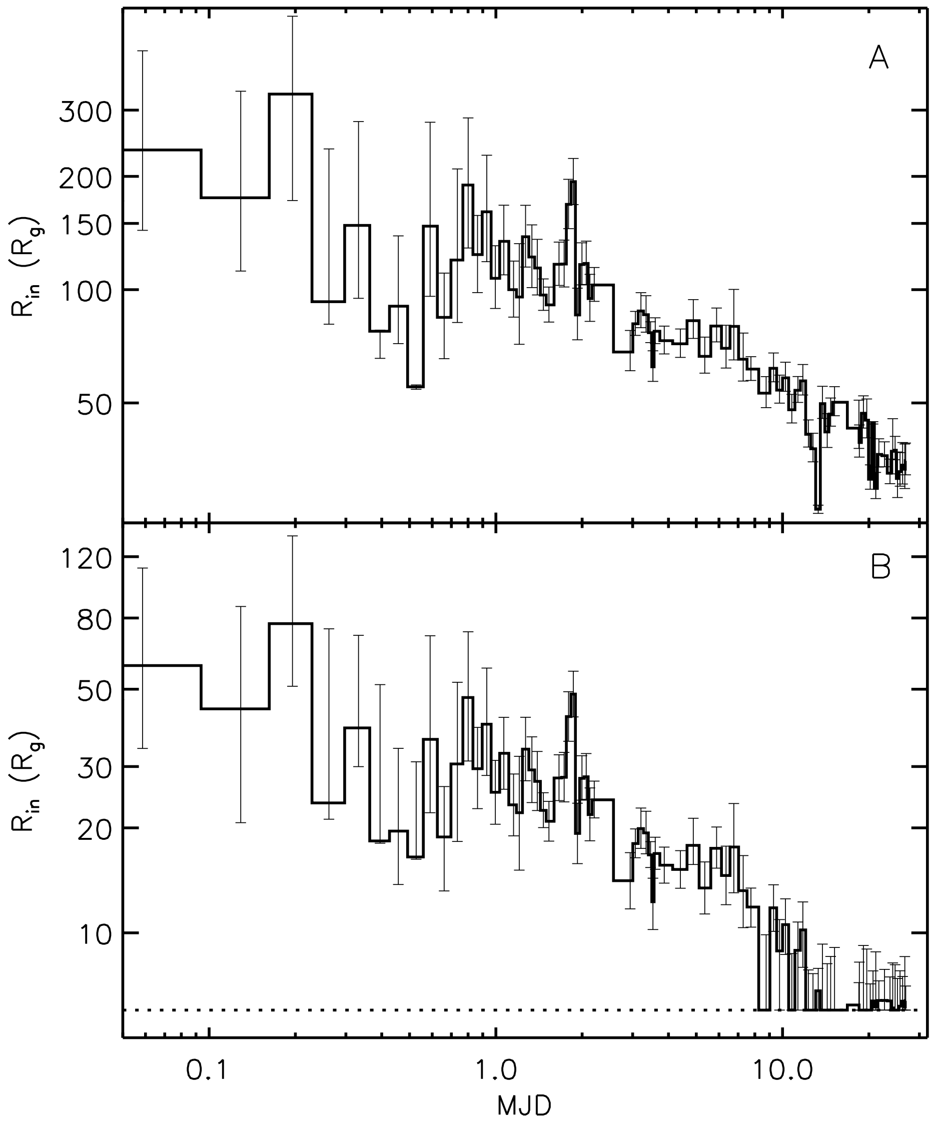

Figure 3.6: The figure shows the variation of the inner disk radius in units of R_g as a function of time. MJD 55464.4 is taken as reference. The values of R_{in} corresponding to the minimum and maximum values of DISKPN normalization are shown in Panel A and B respectively. A dotted horizontal line at $6R_g$ in panel B represents the minimum value of R_{in} allowed by the model DISKPN. Adapted from Jassal & Vadawale (2015).

towards the end, in contrast to the case of the minimum normalization. The well constrained values of power law index and the values of the inner disk radius obtained for the maximum normalization show that the spectral parameters for the maximum normalization are more physical. The scattering fraction, which gives the fraction of seed photons from the disk that are Compton up-scattered into the corona (Steiner et al., 2009b), obtained from the model component `SIMPL` is shown in Panel F of Fig (3.5).

In order to see the evolution of the contribution of the disk radiation, we studied the ratio of absorbed energy flux from the disk to the absorbed total energy flux. This is shown in Panel H of Fig (3.5). It is clear from the figure that the disk contribution continuously increases with the progress of the outburst. One observation (MJD 55485, ObsId 00434928028) shows a peculiar behavior by giving the disk to total flux ratio greater than 1, because the Swift/XRT spectrum alone is not able to constrain the power law index for this particular observation. The power law index obtained from the spectral fit is $\Gamma \sim 1$, which is unphysical. The spectral fit was verified by fitting Swift/XRT observation simultaneously with the nearest RXTE/PCA observation. The power law index obtained from the simultaneous fit is $\Gamma \sim 2.2$ and the ratio of disk to total energy flux is less than 1. Since RXTE observations are not available for the full duration of Swift observations, we have included the parameters obtained from Swift/XRT observation in Fig (3.5).

3.8.2 Correlation Between Spectral Parameters

We studied the correlation between the inner disk radius and the hardness ratio (defined in section 3.8.1) and the correlation coefficient was found to be 0.71 and 0.74 for the minimum and maximum values of normalization respectively. The two parameters are strongly correlated for both the values of normalization. This result is consistent with the general understanding that as the disk region increases with decreasing inner disk radius, the fraction of the soft photons from the disk increases, thereby decreasing the hardness ratio. We found the correlation coefficient between the disk-to-total flux ratio and the hardness ratio to be -0.83 and -0.92 for the minimum and maximum normalizations respectively. Again, these two parameters are found to be strongly correlated. The negative correlation shows that as the contribution in the flux from the disk increases, the spectrum grows softer. Fig (3.5) shows a sharp variation in almost all the parameters between MJD 55477 and 55478, which corresponds to the observation 00434928018. This observation has a very low count rate of 42.49 counts s^{-1}. This might be an observation during the extended dips observed in the MAXI J1659−152 (see Kuulkers et al., 2013; Belloni et al., 2010).

3.8.3 Relation Between R_{in} and T_{max}

We studied the relation between the inner disk radius and the maximum temperature in the disk for both the values of normalization. The observed values from the spectral fit were fitted and the best fit was found to be $kT_{max} = (7.75 \pm 0.93) \mathrm{R}_{in}^{-0.62 \pm 0.03}$ keV and $kT_{max} = (2.96 \pm 0.38)\ \mathrm{R}_{in}^{-0.62 \pm 0.04}$ keV for the minimum and maximum values of normalization respectively (see Fig 3.7). While finding the best fit, those values of R_{in} were ignored where the lower bound is not constrained by the spectral fit. The fitted parameters are comparable with the values reported by Kennea et al. (2011). However, a deviation is observed from the standard result of $T_{max} \propto R_{in}^{-0.75}$. This deviation can be attributed to the variation in the mass accretion rate with the progress of the outburst.

3.9 Mass Estimation

The spectral analysis discussed above not only helped in the study of the outburst and its spectral properties, but also it offers an opportunity to estimate the mass of the black hole in MAXI J1659−152 with the fitted values of normalization. In the present work, mass of the black hole was estimated with the help of the following expression taken from Gierliński et al. (1999),

$$M = \left[\frac{N}{(1 - f_{sc})} \frac{D^2 f_{col}^4}{\cos i} \right]^{1/2} \tag{3.1}$$

where M is mass in solar units, N is normalization obtained from the disk

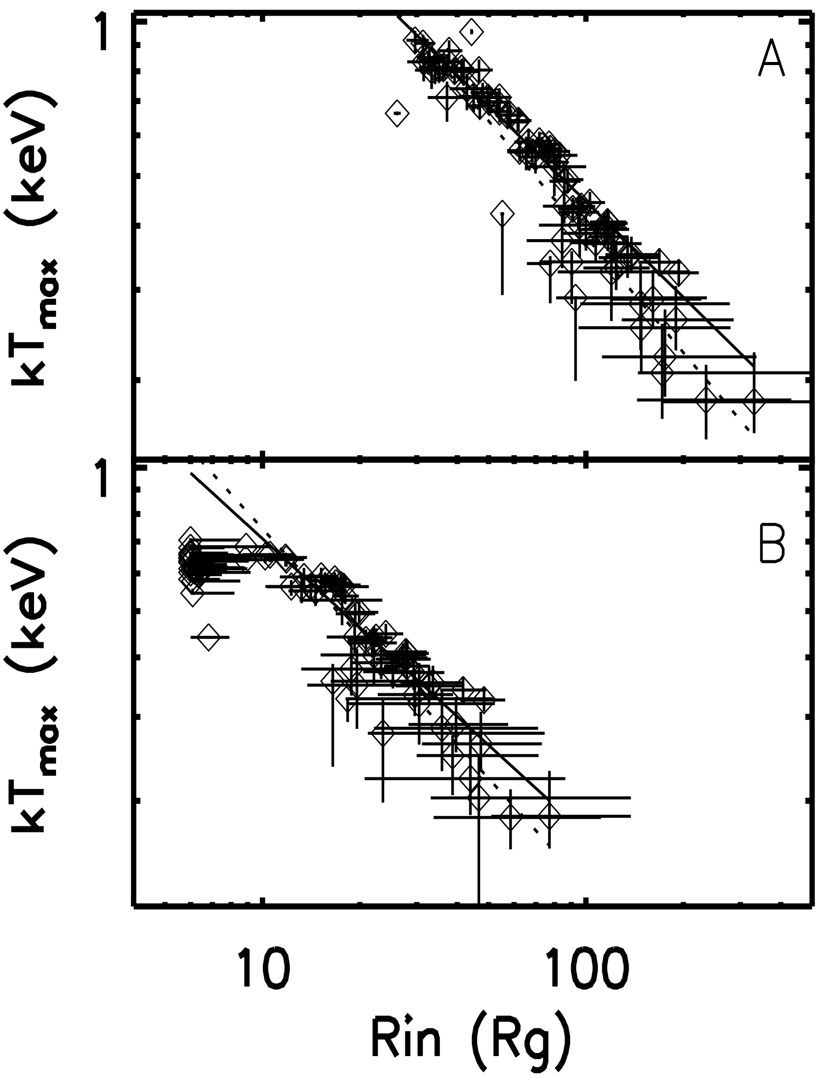

Figure 3.7: The figure shows the obtained values of kT_{max} and R_{in} with DISKPN normalization frozen at the minimum (panel A) and the maximum values (panel B). The solid and dotted lines are the best-fit and standard results respectively. Adapted from Jassal & Vadawale (2015).

component DISKPN, f_{sc} is scattering fraction obtained from the Comptonization component SIMPL, D is distance in kpc, f_{col} is spectral hardening factor and i is inclination angle in degrees. Since the distance and inclination angle are well constrained for MAXI J1659−152, equation (3.1) can be used for mass estimation with the observed values of N and f_{sc}. The inclination angle for the source is expected to be in the range of 60°-70° based on the occurrence of dips and the absence of eclipses in its light curves (Kennea et al., 2011; van der Horst et al., 2013; Kuulkers et al., 2013). The distance to the source reported by many authors is close to 6 kpc (Kaur et al., 2012; Kennea et al., 2011; Jonker et al., 2012). Since the analysis was carried on the 80 spectra, we obtained 80 values of scattering fraction, giving different mass estimates for each of the spectra, for a distance of 6 kpc, inclination angle of 70° and spectral hardening factor of 1.7. One observation (ObsId 00434928018) led to a very high value of mass as the scattering fraction for this particular observation is very high (~ 1). Excluding this observation, a histogram was generated with the remaining 79 mass estimates (Fig 3.8). The weighted average of these values gives the mass of the black hole to be 7.9±2.4 $M_{\odot}$. However, if the uncertainty in distance (5 to 6 kpc), inclination angle (65° to 75°) and spectral hardening factor (1.6 to 1.8) are considered, the estimated mass comes out to be 8.1±2.9 $M_{\odot}$. All the mass estimates were found using the maximum normalization from the simultaneous spectral fit. The mass estimates corresponding to the minimum normalization were less than 3 $M_{\odot}$ and hence were ignored. Therefore, the mass estimate provided here should be considered as an absolute upper limit on the mass of the black hole candidate.

3.10 Summary

MAXI J1659−152 was observed extensively with Swift and RXTE during its discovery outburst in September 2010. In the present work, we have studied 38 observations of the source taken with Swift. Simultaneous fitting of spectra in 10 groups was carried out with a more physical model that included DISKPN and SIMPL. A tighter constraint on the normalization was found with simultaneous

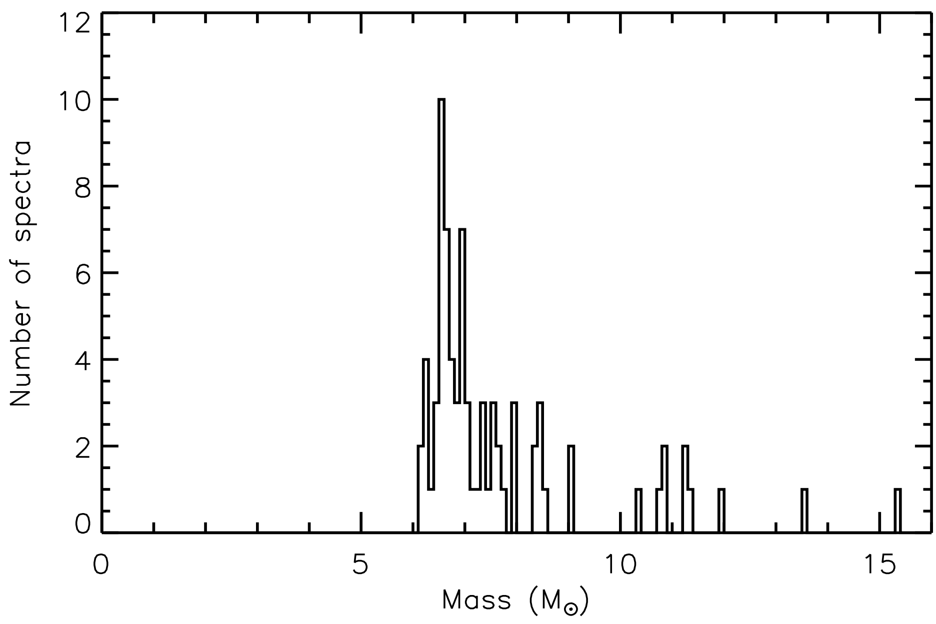

Figure 3.8: The figure shows the histogram of the mass estimates obtained for the 79 spectra. Adapted from Jassal & Vadawale (2015).

spectral fitting compared to fitting of individual spectra. The maximum and minimum values of normalization obtained from the 10 groups were frozen during the fitting of individual spectra. The evolution of the spectral parameters with the progress of the outburst was studied and we found that the inner radius shows a systematic variation. The inner radius of the disk was found to be truncated at hundreds of Schwarzschild radii during the early stages of the outburst. The inner disk gets closer to the black hole as the spectrum becomes softer. This is probably the first observational confirmation of an accretion disk closing in with the progress of the outburst. We consider the results as a supporting evidence for the disk truncation model amongst the growing evidence against it. An upper limit on the mass of the black hole was found to be 8.1±2.9 $M_\odot$ with the help of spectral fitting.

Chapter 4

High Mass Accretion Rate: Extreme Variability

According to the standard model for accretion disks, a disk is unstable both at low and high mass accretion rate. The instability of a disk at low temperature or low mass accretion rate is explained with the hydrogen ionization instability (Lasota, 2001) which takes place in the outer cooler regions of a disk. The temperature in the outer regions increases slowly as the material in the disk builds up with the mass accreted from the companion. As it reaches the hydrogen ionization temperature, the instability is triggered which can result in a massive outburst from the sources. The prevalent transient behavior seen in the low mass black hole binaries provides a strong support for the instability at lower mass accretion rates.

An accretion disk is expected to be unstable at higher mass accretion rate, however, contrary to the case of low mass accretion rate, no black hole binary is found showing signatures of the instability except a confirmed black hole GRS 1915+105. The source has been one of the highly studied black hole binaries and its description is given in Chapter 1. In this chapter, extreme variability of GRS 1915+105 and a transient source IGR J17091−3624 is discussed, which is followed by our results on the study of a particular class of variability seen in both the sources.

4.1 Radiation Pressure Instability

Viscosity plays an important role in the extraction of energy from the material i accretion disks, however molecular viscosity is not adequate to account for the amount of transfer of angular momentum in the accretion disks. Viscous forces in the accretion disks are not fully understood. Shakura & Sunyaev (1973) gave a viscosity prescription which is of significant importance in the progress of accretion theory. The prescription is derived from the limits on the length scale of turbulent eddies and azimuthal velocity of the material in the disk.

According to the prescription, the viscous stresses are proportional to the total pressure, which is the sum of radiation pressure (P_{rad}) and gas pressure (P_{gas}), i.e.

$$\tau \propto P_{tot} \tag{4.1}$$

$$\tau \propto P_{rad} + P_{gas} \tag{4.2}$$

The dependence of radiation pressure and gas pressure on the temperature is given as,

$$P_{rad} \propto T^4 \tag{4.3}$$

$$P_{gas} \propto T \tag{4.4}$$

It is clear from the two expressions that the radiation pressure is dominant at higher temperature than the gas pressure. Moreover, it is sensitive towards a small change in the temperature. In the inner regions of the accretion disk, temperature is high, therefore,

$$\tau \propto P_{rad} \tag{4.5}$$

$$\tau \propto T^4 \tag{4.6}$$

$$\Delta\tau \propto T^3 \Delta T \tag{4.7}$$

A small increase in temperature in an annulus gives rise to a large increase in the viscous stress, which in turn results in more viscous dissipation. Consequently, the temperature further rises leading to even higher viscous stress. This results in a runaway. An increased temperature in the annulus leads to a higher mass accretion rate which depletes the annulus faster than it can be replenished by the outer radii. The density in the annulus decreases and the temperature falls. This completes a cycle. The material slowly builds up in the annulus and the disk shows limit cycle oscillations. This instability is called Radiation Pressure Instability (RPI) and it occurs when the mass accretion rate is high. A detailed description of RPI is given in Taam & Lin (1984). The limit cycle oscillations seen in the legendary source GRS 1915+105 is the only evidence for the unstable accretion disk. In fact, GRS 1915+105 has exhibited extreme variability along with limit cycle oscillations which has never been observed in other black hole binaries (Belloni et al., 2000; Fender & Belloni, 2004). Done et al. (2004) showed that GRS 1915+105 emits most of the time close to the Eddington luminosity whereas luminosity of other sources reaches close to the Eddington limit occasionally. Accreting at a higher mass accretion rate, the source is one of the brightest black hole binary. The high mass accretion rate makes the disk the radiation pressure dominated which triggers RPI and limit cycle oscillations.

4.2 Faint IGR J17091−3624 and its 2011 Outburst

A transient source IGR J17091−3624 entered into an outburst in 2011. Though it has shown outbursts in 1994, 1996, 2001, 2003 and 2007 (Revnivtsev et al., 2003; Kuulkers et al., 2003; Capitanio et al., 2006, 2009), the 2011 outburst is special and different from the previous outbursts. The outburst was unusually long and the source was found active even after one year (Altamirano et al., 2012). The outburst lasted for more than $\sim$1.5 years in contrast to a typical of a few months for the other black hole binaries. The transient source showed extreme variability behavior which is unique to the black hole binary GRS 1915+105. Altamirano et al. (2011) documented the similarities in their light curves for different variability classes (see Fig 4.1). Since IGR J17091−3624 shows extreme variability, it is expected that the source is accreting at a high mass accretion rate

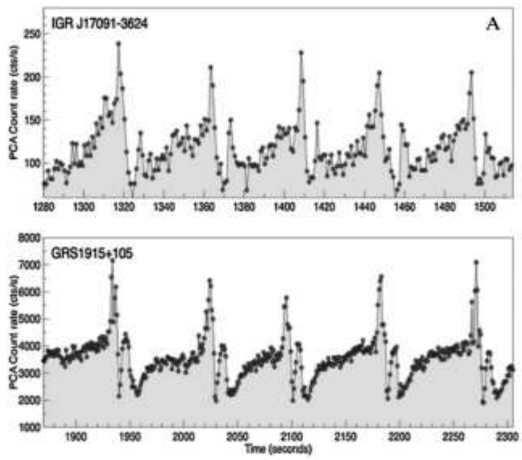

(a) ν class

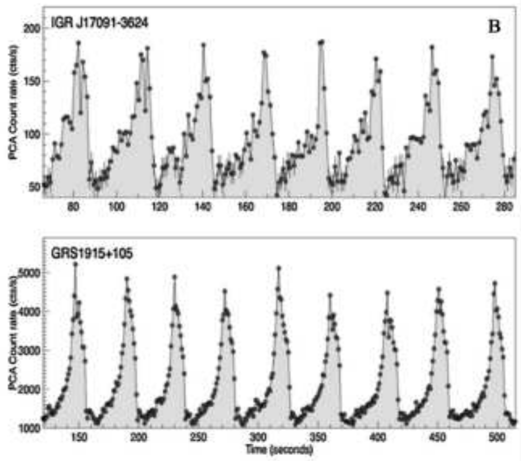

(b) ρ class

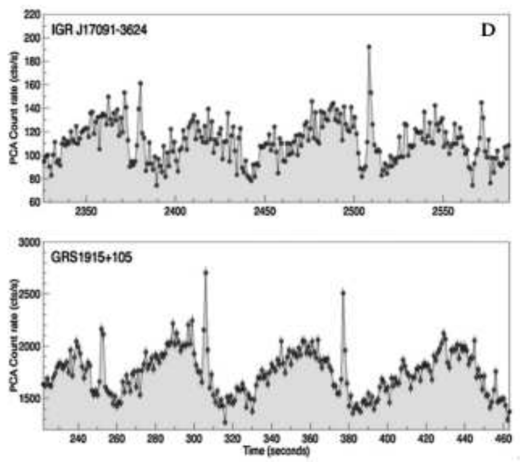

(c) α class

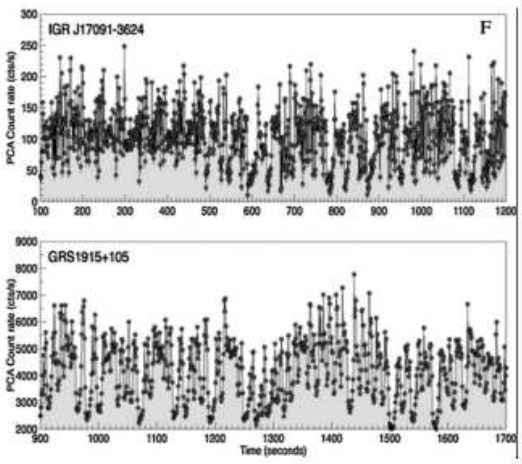

(d) μ class

Figure 4.1: RXTE/PCA light curves for ν, ρ, α and μ classes. The bin size of the light curves is 1 s. Light curves for IGR J17091−3624 and GRS 1915+105 are shown in upper and lower panels respectively. Figure adapted from Altamirano et al. (2011).

and hence, the source should be bright. However, IGR J17091−3624 is about 20 times fainter than GRS 1915+105.

Also, IGR J17091−3624 showed a high frequency QPO (HFQPO) at a frequency of 66 Hz which is very close to a HFQPO seen in GRS 1915+105 at 67 Hz. A very close similarity between the two sources cannot be a coincidence and a comparative study of both the sources can help to get an insight of the physical processes giving rise to such variability patterns. The black hole candidate IGR J17091−3624 was studied comparatively with GRS 1915+105 and the work is discussed here in detail.

4.3 Observations and Data Reduction

The 2011 outburst of the black hole candidate IGR J17091−3624 was extensively followed by RXTE. A strictly simultaneous data set is available for the source from NASA's public archive HEASARC from the two missions RXTE and XMM-Newton. These two data sets compliment each other, with RXTE giving higher energy coverage in a range of 3-35 keV and XMM-Newton covering lower energy range of slightly less than 1 keV to 12 keV using an X-ray telescope. A total energy coverage of 0.7-35 keV was obtained from the two data sets. Both the missions observed the source on March 27, 2011. These pointed observations are long, absolutely simultaneous and continuous. The observation Id of XMM-Newton observation is 0677980201 and the total exposure is $\sim$39 ks. The observation Id and total exposure for RXTE observation are 96420-01-05-000 and $\sim$21 ks respectively. The two data sets offer a total simultaneous exposure of $\sim$15 ks.

The data reduction for RXTE/PCA observation was carried out with HEASoft version 6.8 following standard analysis procedure for Good Xenon mode. The light curve was generated with the PCU2 data with a bin size of 1s and it was found that the source was showing typical ν-class variability pattern (Altamirano et al., 2011) resembling with the 'heartbeats' which continued throughout the complete observation. A section of the light curve for the first 500 s is shown in Fig (4.2). There were a total of 385 bursts in RXTE observation,

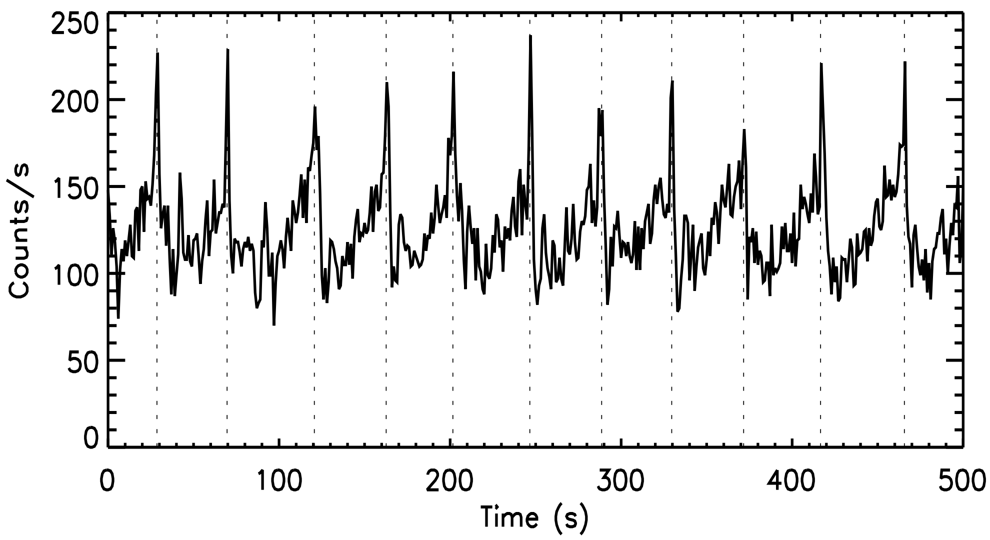

Figure 4.2: RXTE/PCA light curve of IGR J17091-3624 from observation 96420-01-05-000. Light curve was extracted with a bin size of 1s from PCU2 covering energy range 2.0-60.0 keV. The observation has been classified as ν-class observation by Altamirano et al. (2011).

however XMM-Newton observation continued further and it covered even more ‘heartbeats’ from the source. Further analysis was restricted to 385 bursts covered by both the instruments as it offers the simultaneous spectroscopy. The bursts are quasi-periodic with the burst period in a range of 30-50 s. The mean burst period is 39 s. A study of spectra of different phases of an individual burst is not possible as the counts in a phase spanning a few seconds are small enough to perform meaningful spectral fitting with different models. Therefore, the light curve was folded to improve the statistics in each phase. Since the bursts are quasi-periodic, a different method was followed to fold the light curves and collect the photons from different phases of the bursts.

4.3.1 Folding the light curves

In order to fold the light curve from RXTE data with respect to the peaks of the bursts, it is required to know the time of peaks in each of the bursts in the light curve. An IDL script was used to determine the peak positions in a semiautomatic manner. The peak-to-peak interval between consecutive bursts was then divided into 64 phases (or intervals) of equal lengths. The start and stop times for each of these phases obtained in terms of RXTE mission time were then converted into start and stop times for XMM-Newton mission using a tool xTime available on HEASARC and an IDL script. The start and stop times for 64 phases were given as input to the extractor *seextrct* to generate 64 spectra. In this way, the counts for a particular phase from a total of 385 bursts were co-added. With the help of total counts and total exposure for each of the phase spectrum, a folded light curve was generated (Fig 4.3).

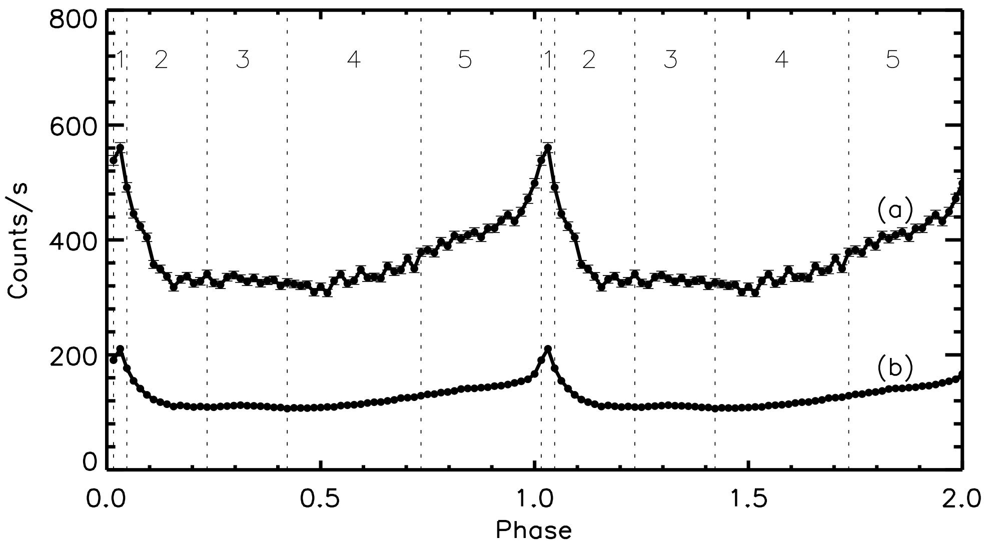

Figure 4.3: Folded light curve for XMM-Newton (a) and RXTE (b) for the two burst cycles. There are 64 phases in a burst cycle. Dotted vertical lines show the demarcations for the five phases.

The XMM-Newton observation was carried out in fast timing mode of EPIC-MOS and burst mode of EPIC-PN. The standard analysis procedures for these modes were followed using SAS v11.0.0 and the latest calibration files. The data from XMM-PN only were used because MOS2 data could not be checked for possible pileup (generation of pattern plot always resulted in error) whereas MOS1 data are not useful in the timing mode because of a dead pixel in the CCD. For PN data, the observed and the expected pattern behavior differed below 0.7

keV and hence the energy range for the rest of the analysis was restricted to 0.7-12.0 keV. The start and stop times for the 64 phases in terms of XMM-Newton mission time were used to generate gti files using SAS task *gtibuild*. These gti files were used for extracting the 64 phase spectra using the task *evselect*. The phase-folded light curve was generated using the total counts and the exposure times, as described earlier for RXTE. The folded light curve is shown in Fig (4.3) for both the missions. It is clear from the figure that the folded light curves maintain a typical burst shape, though the subtle features have been washed out as a result of co-adding and quasi-periodicity of the bursts. Further, it was seen that the oscillations were more pronounced in the XMM light curve, indicating that the accretion disk radiation was primarily participating in the oscillations and not the Comptonized emission from the corona which dominates at higher energies. The spectral fitting can now be performed as the co-adding of counts from corresponding phases improves the statistics. The source spectra for all the phases were extracted using RAWX columns between 32 and 42 for single and double pixel events (pattern 4). SAS tools *rmfgen* and *arfgen* were used to generate redistribution matrices and ancillary files respectively, and the same files were used for the spectra of all phases. The background spectrum was extracted from RAWX columns between 5 and 7 after confirming that the region was not contaminated significantly with source photons in the selected energy range. A single background spectrum was used for all the phases in the spectral analysis. All the spectra were rebinned using SAS task *specgroup* to get a minimum of 25 counts per channel.

4.4 Analysis and Results

The spectral analysis was carried out in two ways after dividing the bursts into 64 phases. First, the 64 phases were grouped into 5 phases as shown in Fig (4.3) with vertical lines and the spectra were extracted for the new 5 phases which were fitted simultaneously and the results are discussed in the section (4.4.1). Secondly, the 64 phases were grouped into 16 phases of equal lengths and the spectra were fitted individually and the results are shown in section (4.4.3).

4.4.1 Simultaneous fitting with 5 phases

Instead of studying the spectra for a full length of observation, a different approach was taken for spectral analysis. Spectra were generated for the 5 phases from both Proportional Counter Array (PCA) and PN. The 10 spectra (5 spectra each for RXTE and XMM-Newton) were loaded into `XSPEC` as 10 data groups and fitted simultaneously.

The spectral parameters of a model can be divided into two categories: parameters which are dependent on the geometry of the source and the parameters describing the accretion processes in the disk. The geometry dependent parameters e.g., mass, spin, inclination and distance, are not expected to vary from one phase to the other, therefore these parameters can be tied across different phases in the spectral fitting. On the other hand, the mechanism dependent parameters e.g. mass accretion rate, temperature, inner disk radius and photon index may vary with the phases of the bursts, therefore these parameters were fitted independently in the simultaneous fitting of 10 spectra. This scheme of spectral fitting gives a tighter constraint on both the geometry dependent and mechanism dependent parameters along with the information about the variation of the mechanism dependent parameters with phases of the burst.

Wide-band X-ray spectrum of a black hole binary generally comprises of two main components: a multi-temperature disk black body component coming from the cool, optically thick and geometrically thin disk and a high-energy Comptonization component originating from Compton scattering in an optically thin region surrounding the disk, known as corona. The multi-temperature component is generally fitted with the canonical model `DISKBB` for a non-relativistic study. We have used `DISKPN` which is a modified version of `DISKBB`. The advantage of using `DISKPN` over `DISKBB`, in the present work is that the model `DISKPN` allows the clear separation of parameters in two categories of accretion-process-dependent-parameters and system parameters. `DISKPN` has three parameters: maximum temperature in the disk T_{max}, inner disk radius R_{in} and its normalization which has all the system parameters e.g mass, distance and inclination. For the general relativistic description of the multi-temperature disk spectrum, KERRBB (Li et al., 2005) was used. The model takes care of the effects of general relativity on the spectra and it is widely used for the accurate modeling of disk spectrum and to investigate spin of the black hole. The high-energy tail is generally fitted with a power law to approximate the Comptonized component. However, Steiner et al. (2009b) proposed a more physical model SIMPL to empirically describe the Comptonized component. They mention that SIMPL is a more appropriate model for fitting Comptonized radiation than power law particularly when less is known about physical conditions like optical depth, geometry and temperature etc which is true for the new source IGR J17091−3624. Power law is meant for modeling the high energy tail, though it contributes at lower energies as well, where the disk emission is dominant however, SIMPL cuts off at lower energies and models the high energy tail by taking a fraction of soft disk photons for the inverse Compton scattering. Therefore, we attempt to fit the spectra by replacing power law with SIMPL and convolving with DISKPN and KERRBB one by one. The results of the spectral fitting with SIMPL and DISKPN are discussed below.

Fitting with DISKPN

For the non-relativistic treatment, the spectra were fitted with the model CONST*PHABS*(SIMPL⊗ All the 10 spectra, loaded simultaneously in XSPEC and fitted with this model are shown in Fig (4.4). The multiplicative constant was frozen at 1.0 for PN, whereas for PCA it was kept free, however, tied across the five phases. The constant takes care of the calibration uncertainty between the two instruments. DISKPN normalization was tied together for all the 10 spectra because it has all the system parameters which are not expected to vary between different phases of the burst. The other two parameters T_{max} and R_{in} from the DISKPN model; and photon index, scattering fraction and normalization from SIMPL were independently free for different phases. However, they were tied together for the two spectra from the two missions for a particular phase. The interstellar absorption arises from

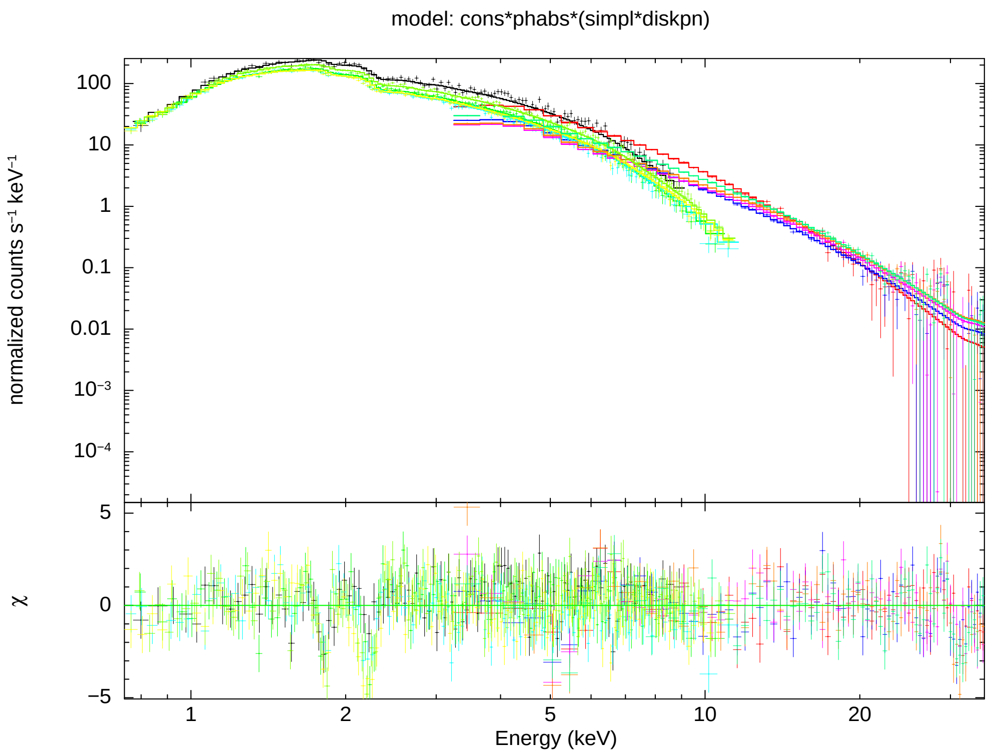

Figure 4.4: Spectra of 5 phases from the two missions fitted with `CONST*PHABS*(SIMPL⊗DISKPN)` covering an energy range of 0.7-35 keV. The lower panel shows the reduced chi-square values.

the photoelectric absorption by interstellar medium of the soft photons, therefore this should not be a function of accretion processes taking place in the accretion disk and should be tied across phases. However, any phase-dependent absorption intrinsic to the source may contribute to the variation in N_H. In order to confirm the same from the spectral fitting, it was treated as a free parameter. It was, however, found that the N_H values for the five phases were not significantly different and the fitted values of N_H were in agreement with the values reported by Rodriguez et al. (2011) and Krimm et al. (2011). It was found that the accretion process dependent parameters vary as a function of phases of the bursts and the parameters obtained from the five phases have been shown in Table (4.1). It can be seen from the table that the inner disk temperature is maximum during phase 1 which corresponds to the peak of the bursts. This implies a higher mass accretion rate during peaks of the burst as expected. Since the data is split into five phases, it was verified that neither the Fe-line nor the reflection component was required to fit the spectra of individual phase separately. A best fit was obtained with the χ^2 value of 1709.0 for 1030 degrees of freedom. For the present work, the `DISKPN` normalization $N_{DPN} = \frac{M^2 cos(i)}{D^2 f_{col}}$, is of most importance, as it can provide constraints on mass (M), distance (D), and inclination (i). The best-fit value of the `DISKPN` normalization was found to be, $N_{DPN} = 4.0 \times 10^{-4}$. Assuming a minimum mass of $\sim 3\ M_\odot$ and a maximum distance of $\sim$ 25 kpc for a Galactic black hole candidate along with a standard value for color correction factor, $f_{col} = 1.7$, the best-fit value of N_{DPN} resulted in a lower limit on the inclination angle of 76°. The upper limit on `DISKPN` normalization was found from the spectral fitting using *steppar* command. Considering the 90% upper confidence limit of 1.04×10^{-3} for the normalization, the lowest possible inclination angle was 53°. Since spectral fitting could not constrain the lower limit of N_{DPN} , it was not possible to obtain an upper limit on inclination with the spectral fitting. Instead, the lower limit on normalization of 0.30×10^{-4} was calculated using the maximum values of inclination and distance and the minimum value of mass (shown in Table 4.1). The lower limit on inclination found in this work comes only from the simultaneous spectral fitting and it is not dependent on any additional information, and hence it can

Table 4.1: Parameters obtained from simultaneous fit of spectra of 5 phases with the model CONST*PHABS*(SIMPL⊗DISKPN).

Phase	1	2	3	4	5
N_H ($\times 10^{22}$cm^{-2})	$0.93^{+0.04}_{-0.03}$	$0.84^{+0.02}_{-0.02}$	$0.82^{+0.02}_{-0.02}$	$0.81^{+0.01}_{-0.01}$	$0.88^{+0.01}_{-0.01}$
T$_{max}$ (keV)	$1.24^{+0.05}_{-0.05}$	$1.11^{+0.01}_{-0.01}$	$1.02^{+0.01}_{-0.01}$	$1.05^{+0.01}_{-0.01}$	$1.11^{+0.01}_{-0.01}$
R$_{in}$ (R_g)	$23.45^{+2.78}_{-2.33}$	$23.50^{+1.12}_{-1.04}$	$26.63^{+1.22}_{-1.17}$	$24.79^{+0.93}_{-0.87}$	$25.81^{+0.98}_{-0.93}$
Γ	$3.58^{+0.25}_{-0.28}$	$2.66^{+0.10}_{-0.01}$	$2.56^{+0.06}_{-0.06}$	$2.52^{+0.04}_{-0.04}$	$2.70^{+0.06}_{-0.06}$
Scattering fraction	$0.47^{+0.02}_{-0.24}$	$0.27^{+0.02}_{-0.02}$	$0.36^{+0.02}_{-0.02}$	$0.37^{+0.01}_{-0.01}$	$0.35^{+0.02}_{-0.02}$
Disk Flux^a	2.27	1.38	1.28	1.34	1.72
Total Flux^a	1.85	1.08	0.89	0.93	1.29
DISKPN normalization^b			$4.44^{+6.36}_{-4.14}$x10^{-04}		

a: Unabsorbed flux in units of $\times 10^{-9}$erg s^{-1}cm^{-2} for 2-10 keV energy range. Unabsorbed bolometric disk flux for phase 1 is 4.10×10^{-9}erg s^{-1}cm^{-2}.

b: Since spectral fitting could not constrain lower limit of norm, it was calculated from extreme values of M, D and i.

be considered to be fairly robust. However, the simultaneous spectral analysis with DISKPN to model accretion disk spectra suggests that IGR J17091−3624 is a high inclination binary. This is an important result which is consistent with the findings of Capitanio et al. (2012) and King et al. (2012). The spectra were studied with the relativistic model KERRBB after studying it with the non-relativistic model. The non-relativistic treatment and the constraint on inclination obtained from it helped in the relativistic treatment of the spectra.

Fitting with KERRBB

For the relativistic treatment of the spectra, DISKPN was replaced with the relativistic model KERRBB and convolved it with SIMPL. Spectra were fitted with the model CONS*PHABS*(SIMPL⊗KERRBB). Fig (4.5) shows the 10 spectra loaded into

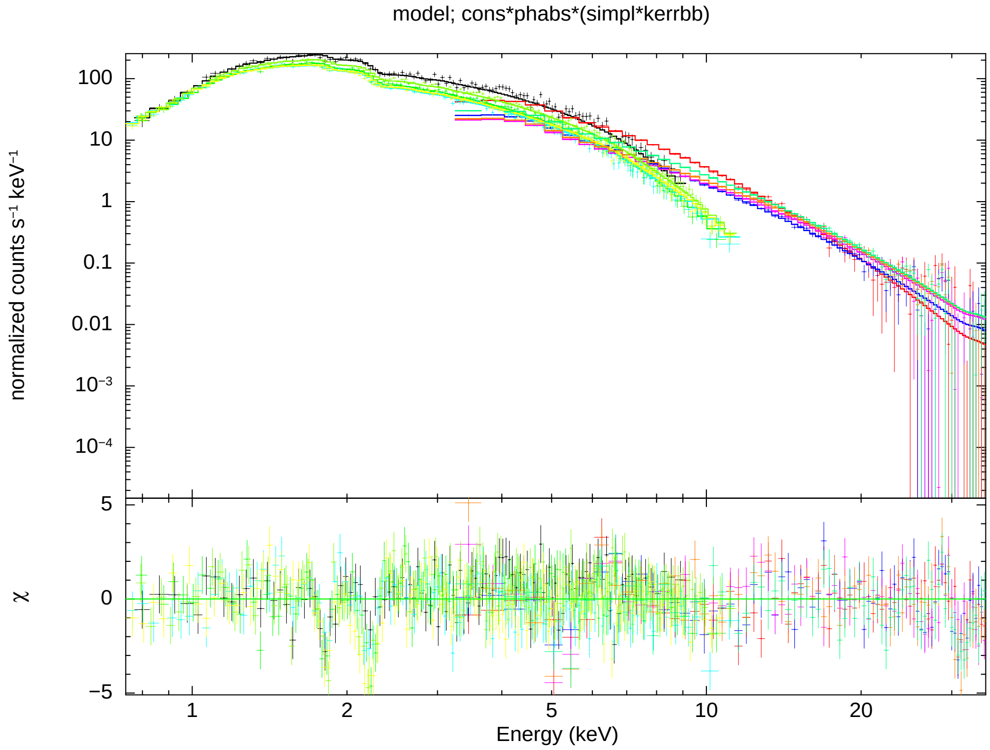

Figure 4.5: Spectra of 5 phases from the two missions fitted with `CONST*PHABS*(SIMPL⊗KERRBB)` covering an energy range of 0.7-35 keV. The lower panel shows the reduced chi-square values.

XSPEC and fitted with this model. The model KERRBB has system parameters mass, distance, inclination, and spin as separate fit parameters unlike DISKPN. None of these parameters are well determined for the new source. Also, KERRBB has parameters governing the second-order effects such as spectral hardening factor, returning radiation, and limb darkening. These parameters were frozen to their default values. Typically, KERRBB is used for disk-dominated spectra with luminosity $< 0.3\ L_{Edd}$, however, Steiner et al. (2009a) have shown that SIMPL⊗KERRBB can be used to accurately describe spectra with higher luminosities as well. This allows to fit the spectra of this source with SIMPL⊗KERRBB, instead of our ignorance on Eddington luminosity of the source as mass is not very well constrained. All the parameters of the KERRBB model, except the column density, N_H and mass accretion rate, were tied across the five phases. Further, the normalization was frozen to 1.0. Since all system parameters cannot be fitted simultaneously, specific values of mass, inclination, and spin were selected and the spectra were fitted for mass accretion rate and distance. In order to systematically investigate the parameter space, the black hole mass and spin were varied in exhaustive ranges of $3-20\ M_{\odot}$ and $0-0.9$ respectively. Since it was found that the source is a high inclination binary from the non-relativistic study mentioned in the previous section, the inclination angle was varied from 50° to 85°. The results obtained from this analysis are shown in Figures (4.6) and (4.7) where the former shows the variation of interstellar absorption (N_H), two parameters of SIMPL: power-law index (Γ) and the scattering fraction (f_{sc}), and fit statistic (χ^2_ν) for the five phases. Since these parameters are more or less the same for any combination of system parameters (mass, distance, inclination, and spin), these are shown without any distinction. Again it was found that neither the Fe-line nor the reflection component is required for fitting the data, with the F-test chance improvement probability being >88% for all combinations of mass, distance, and inclination. For a combination of mass M, inclination i (>50°), and spin a_*, the fitted values of distance D (top panel) and mass accretion rate $\dot{\mathrm{M}}_{Edd}$ (bottom panel) have been shown in Fig (4.7). Only the maximum (phase 1) and minimum (phase 3) mass accretion rates have been shown in Fig (4.7) for the sake of clarity. Error bars (90% confidence limit) are smaller than the symbols for most of the points in the plot. This indicates that the distance and the accretion rate obtained from simultaneous fitting of the spectra of different phases, are very well constrained for a given combination of system parameters.

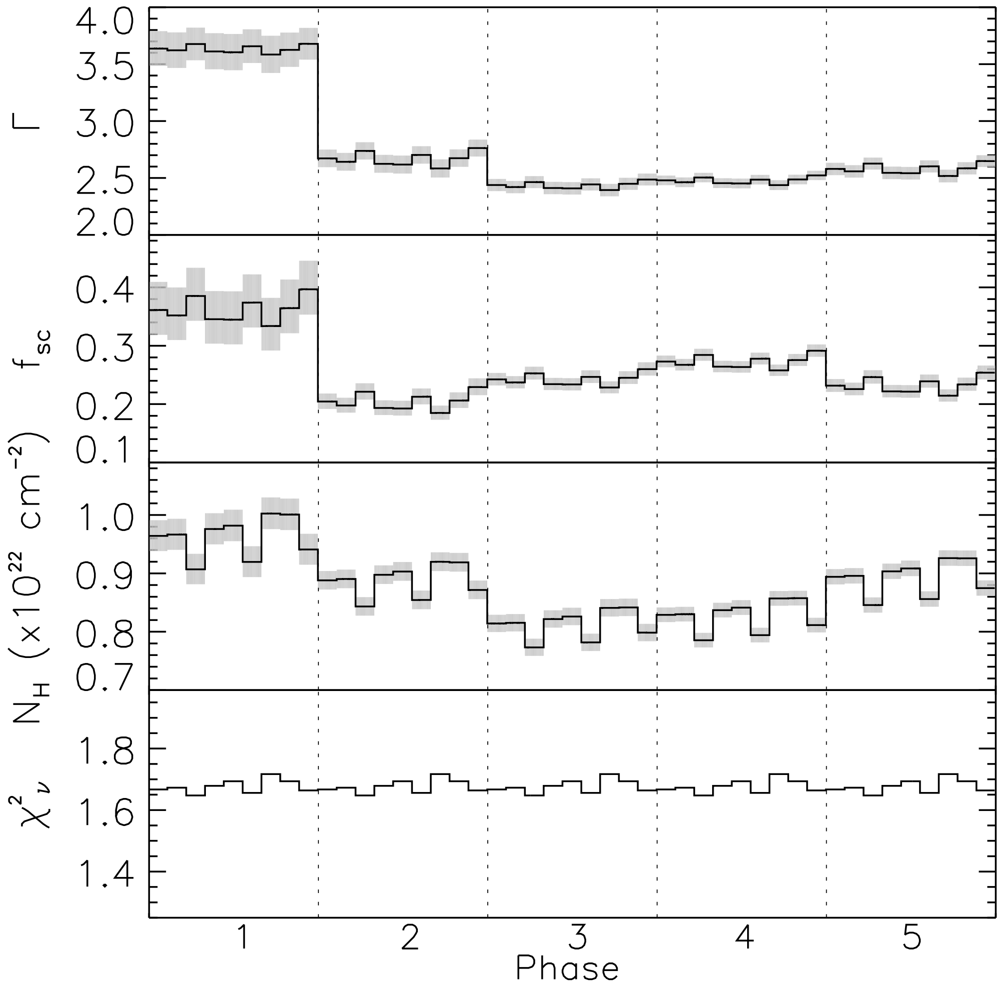

Figure 4.6: The plot shows the best-fit values for the five phases of power law index, scattering fraction, absorption column density, and χ^2_ν for all combinations of D, M, i, and a_*. The parameters are shown for different combinations of system parameters. Error bars (90% confidence) are shown with gray and only a subset of data are shown here.

Fig (4.7) can be used to put some significant limits on the spin of the black hole with some independent constraints on either black hole mass or distance. One such independent constraint on mass comes from the total luminosity argument during 'heartbeat' oscillations. Neilsen et al. (2011, 2012) studied such oscillations in GRS 1915+105 and suggested the radiation pressure instability augmented by the local Eddington limit within the inner accretion disk to be the origin of such a variability pattern. However, this mechanism requires high accretion rate. Neilsen et al. (2011) showed that during the peak of the 'heartbeat', the bolometric disk luminosity is typically as high as 80-90% of the Eddington luminosity. Given the similarity between the variability patterns in GRS 1915+105 and IGR J17091−3624, it is natural to assume a similar mechanism operating in both sources. In this way, the observed flux during the peak of the 'heartbeat' oscillations can be used to estimate the distance for a given mass, or, in other words, 'heartbeat' can be used as a standard candle to constrain the parameters. The best-fit value of the peak bolometric flux was found to be 4.10×10^{-9} erg s^{-1} cm^{-2} . Fig (4.2) shows that the peak flux in individual bursts is not the same and there is a burst-to-burst variation in the peak flux values. Therefore, we have assumed the range of the peak flux to be $(3.0\text{-}5.0)\times10^{-9}$ erg s^{-1} cm^{-2} and a more conservative range of peak luminosity to be 60-90% of Eddington luminosity. The obtained possible $M - D$ range is shown as a gray area in the top left corner of Fig (4.7). It can be seen that the points within this region correspond to a low mass black hole with the mass <5 $M_\odot$ and distance more than 20 kpc. The lines corresponding to the inclination angle <60° and spin <0.2 enter into the gray region. We further fit the spectrum with a_*=0,-0.2 and the obtained values of mass and distance are shown in the same figure. Hence, our results suggest a lower value of spin (a_* <0.2), including negative values of spin parameter if it is assumed that the high mass accretion rate, or particularly, radiation pressure instability is the reason behind hearbeat type of variablity in IGR J17091−3624. However, the lower limit on inclination was found to be 76° from `DISKPN` normalization. This presents the tantalizing possibility of the black hole spin being retrograde, indicating a black hole spin in an opposite direction to the accretion disk. Further, a lower limit of 53° on the inclination angle was found from the 90% upper confidence limit of `DISKPN` normalization. The points corresponding to $i \geq 50°$ require the spin to be <0.2. Thus, we exclude the possibility of high spin and it appears that the main reason for the observed faintness of IGR J17091−3624 is very low (or even negative) spin of the black hole, in contrast to GRS 1915+105, which is known to have a very high spin (McClintock et al., 2006; Middleton et al., 2006). It can be seen that even for the exotic type of black hole with mass <3 M (Altamirano et al., 2011), this inference on black hole spin remains valid. Further, in order to verify the effect of the other frozen parameters of `KERRBB`, such as returning radiation, limb darkening, and inner boundary stress, all these parameters were enabled (one by one as well as all together) and it was found that the lines corresponding to a particular combination of spin and inclination angle move away from the shaded region. It was verified that the same is valid when `POWERLAW` is used instead of `SIMPL`. Thus, for any combination of these parameters or model for the high-energy tail, the black hole spin is required to be either very low or negative.

Reis et al. (2012a) studied full time-integrated spectra of the source and found the presence of line in the spectra and they fitted it with relativistic line model `LAOR` and claimed that the source has high spin. It is noticeable that the two methods of spin determination are known for showing discrepancy (Wagoner, 2012). We, however, have repeated the whole exercise by adding relativistic line model `LAOR` in our simultaneous spectral fitting of 5 phases, and again generated the Fig (4.7) to find out the changes in our results after inclusion of line. The results are shown in Fig (4.8). It is clear from the figure that the results do not change after including line in the spectral analysis, though it improves the fit. This again makes our results robust.

4.4.2 High Frequency QPO at 66/67 Hz

One more similarity between the two sources is the finding of HFQPO at almost similar frequencies. GRS 1915+105 and IGR J17091−3624 show HFQPO at 67 and 66 Hz respectively. HFQPOs are generally believed to be scaled with the mass of the black hole. The 66 Hz HFQPO of IGR J17091−3624 detected by Altamirano & Belloni (2012) may also be considered to be an independent

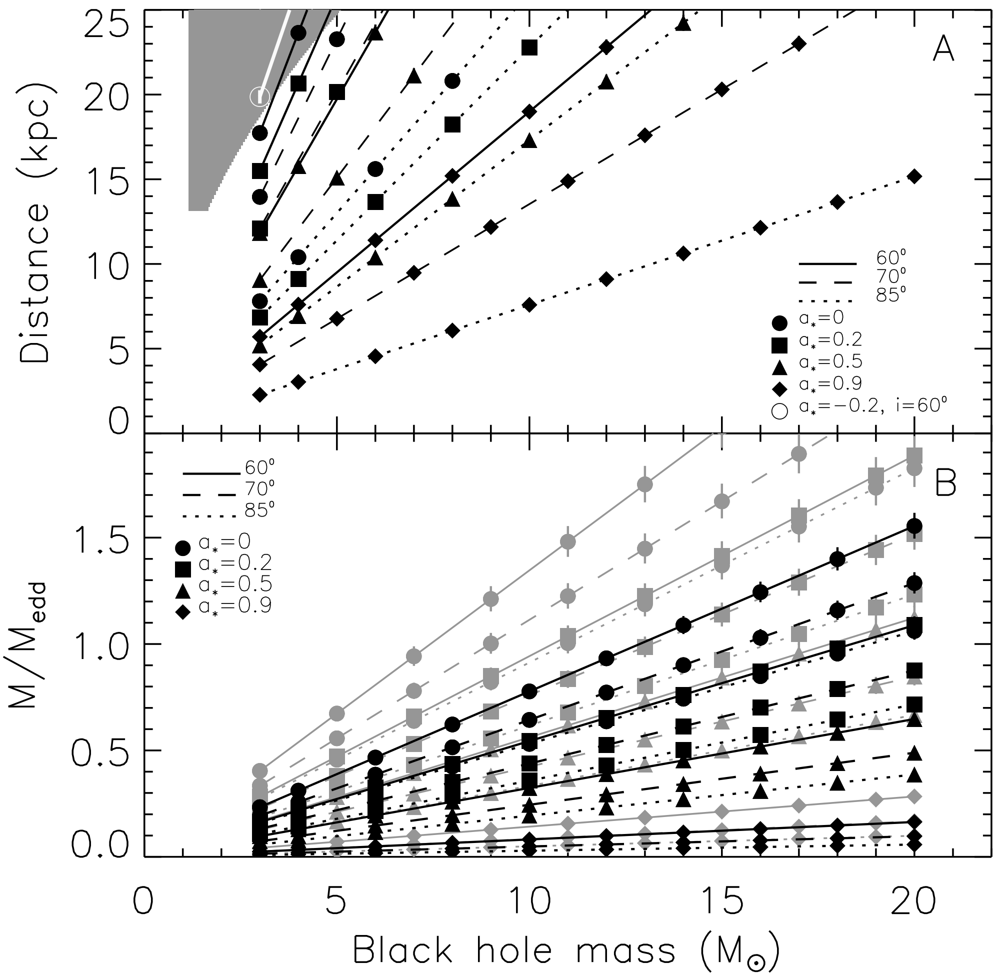

Figure 4.7: The obtained variation of distance (panel A) and mass accretion rate (panel B) as a function of mass for different inclination angles and spins. Symbols are shown for alternate values of mass, and mass accretion rate is shown only for the maximum (gray) and the minimum (black) of the five values. The gray region in the top left corner of panel A shows the allowed range for the black hole mass and distance from the luminosity argument.

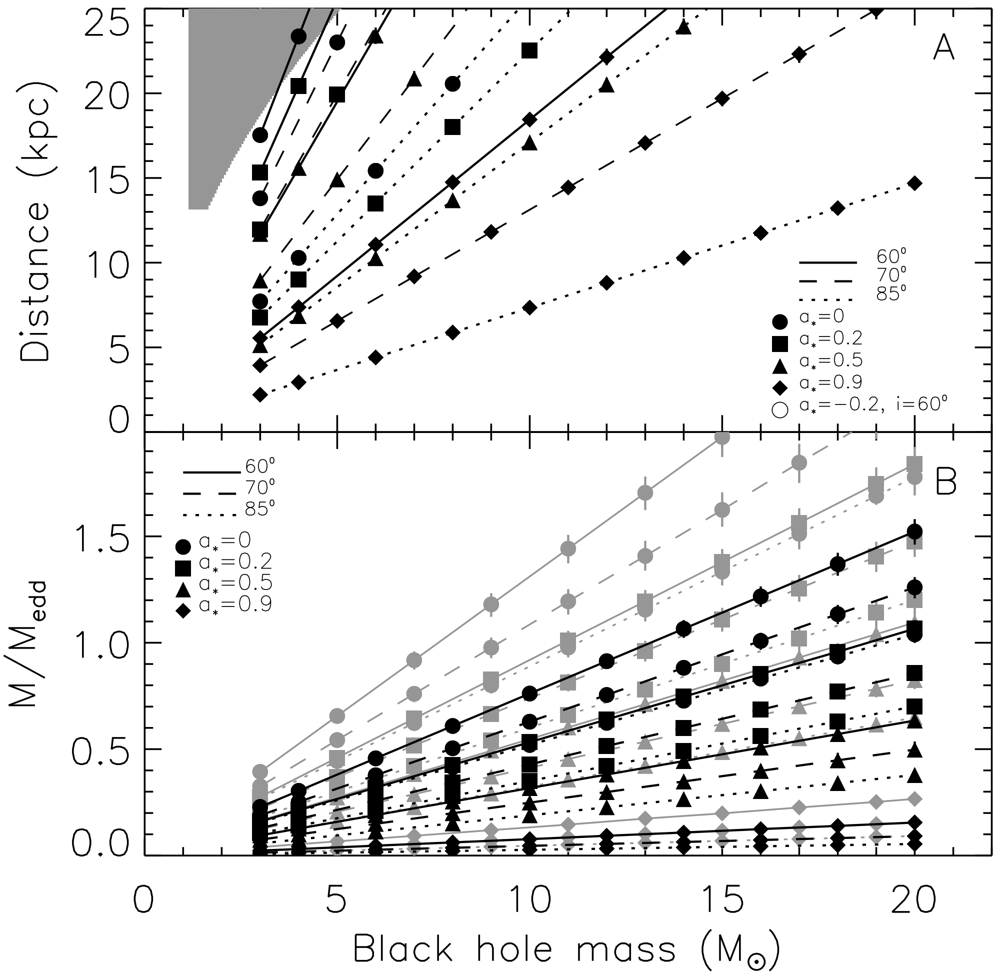

Figure 4.8: The plot shows variation of distance (panel A) and mass accretion rate (panel B) with black hole mass as obtained from spectral fit after including line model `LAOR`. The plot is reproduction of Fig (4.7) after including line model.

constraint on black hole mass, if it is assumed to be related to mass. In this case, the black hole mass in IGR J17091−3624 has to be $\sim$15 $M_\odot$. For such a high black hole mass, Fig (4.7a) does not provide any constraint on the distance; however, both the inclination angle and the spin are required to be $>70°$ and >0.7, respectively. For these high values of inclination angle and spin, Fig (4.7b) shows that the required accretion rate is only a small fraction of the Eddington accretion rate. Thus, if it is assumed that the 66 Hz QPO is related to the black hole mass, the basic accretion process giving rise to the apparent similar variability of GRS 1915+105 and IGR J17091−3624 has to be different. However, it is more likely, as also suggested by Altamirano & Belloni (2012), that the 66 Hz HFQPO is linked to some mechanism common in both the sources, instead of being directly related to the black hole mass. In that case, the previous argument for low black hole mass based on the apparent flux and similar accretion process between IGR J17091−3624 and GRS 1915+105 holds, and the inference of low or negative spin remains valid. Overall, this work indicates that the black hole spin may not play a significant role in generating the observed extreme variability and such a behavior is generated mainly by a high accretion rate.

4.4.3 Fitting 16 phases individually

After fitting the spectra of different phases simultaneously, 64 phases were grouped into 16 phases of equal length and the spectra were extracted. Spectra of individual phase were fitted separately with `CONS*PHABS*(SIMPL*DISKPN)`. The normalization of `DISKPN` was frozen at the best fit value obtained from the simultaneous fitting of spectra of 5 phases. Variation of different parameters were studied as a function of phase of the burst and the results are shown in Fig (4.9). It is clear from the figure that the maximum temperature in the accretion disk and the inner disk radius vary periodically. When the inner disk radius decreases or the inner disk moves inward, the maximum temperature in the disk increases. During peak of the burst, temperature is maximum and the inner disk radius is closest to the central object during an individual burst. A periodic variation in photon index can also be seen in Fig (4.9). However, photoelectric absorption

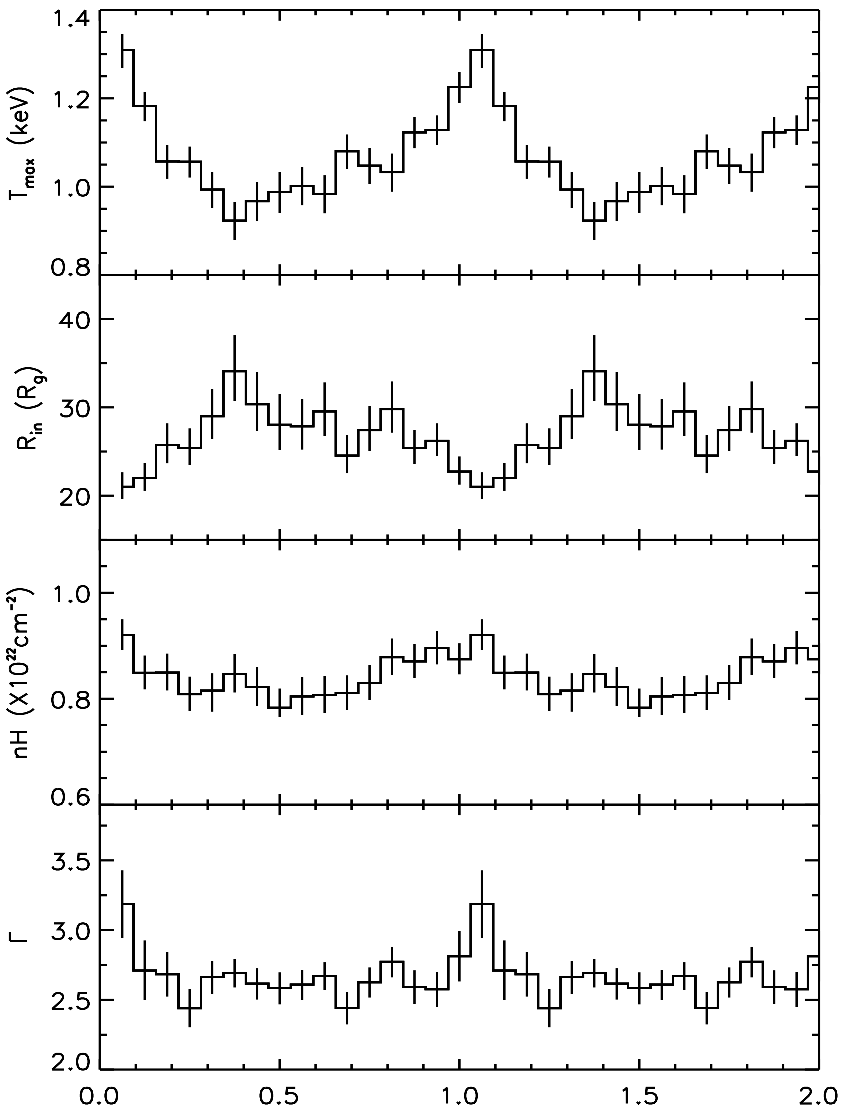

Figure 4.9: The variation of spectral parameters as a function of 16 phases of the bursts. The spectra were fit individually with DISKPN normalization frozen at the value obtained from simultaneous spectral fitting.

remains constant during an individual burst. This confirms that the periodic variation in the brightness of the source is intrinsic as no periodic variation in N_H was observed.

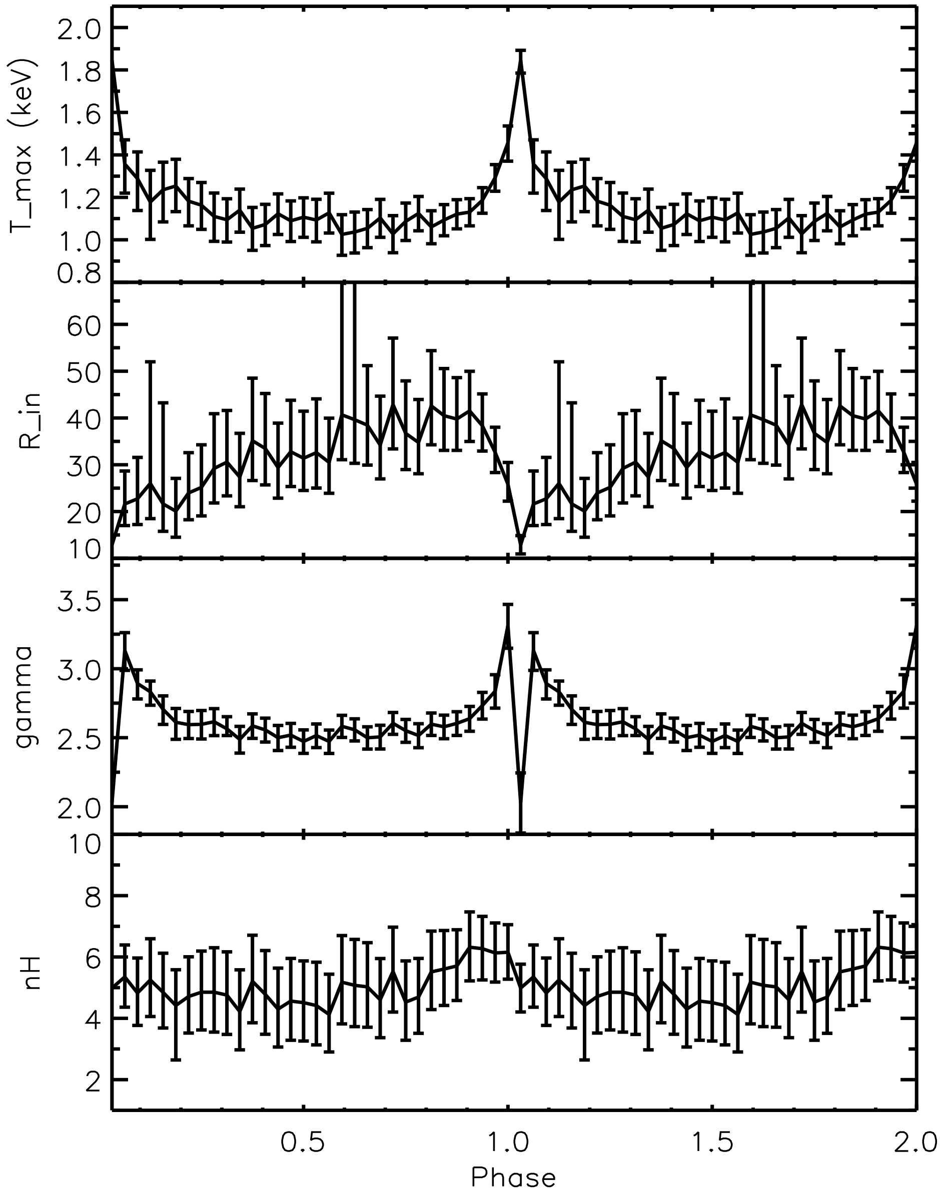

Figure 4.10: The variation of spectral parameters as a function of 32 phases of the 'heartbeats' seen in GRS 1915+105.

To study these spectral properties comparatively with GRS 1915+105, the entire procedure was repeated for the 'heartbeats' of GRS 1915+105. The source was observed by RXTE on May 13, 1997 and the light curve showed 'heartbeat' type oscillations. The observation Id is 20402-0-27-02. The variation in parameters with phases of the burst is shown in Fig (4.10). Each burst was divided into 32 equal phases for GRS 1915+105 instead of 16 phases for IGR J17091−3624 because GRS 1915+105 is a bright source, which allows spectral analysis for smaller intervals. A comparison of Fig (4.9) and (4.10) shows that the two source are not only similar in their apparent variability behavior, but also they show similar spectral properties. The variations in maximum temperature, inner disk radius and photon index is quite similar in both the sources, though the variations are more pronounced in GRS 1915+105 because of better statistics. Radiation pressure instability explains the variation of temperature in the source, however it does not explain why inner disk radius remains almost constant while the temperature in the disk increases during the burst. It is clear from this behavior that the radiation pressure instability is not sufficient to explain the 'heartbeats' in the two sources. This indicates the presence of some other mechanism which is responsible for the observed behavior of the inner disk radius. The discrepancy between observed and predicted amplitudes of the bursts is also indicative of presence of mechanisms other than RPI. Lin et al. (2009) have suggested that this mechanism may be linked to local Eddington rate which may result in observed changes in the inner disk radius.

4.5 Summary

GRS 1915+105 exhibits extreme variability and spectral changes over timescales as short as a few tens of seconds. Observations of similar variability in another black hole binary, IGR J17091−3624, establish that such an extreme variability of GRS 1915+105 is not due to some specific coincidences unique to one particular black hole binary, but is a more generic phenomenon. Here, the results are presented from the simultaneous fitting of 0.7-35.0 keV spectra during different phases of the 'heartbeat' oscillations in IGR J17091−3624, which indicate that the most likely difference between GRS 1915+105 and IGR J17091−3624 is in the spins of the respective black holes. While the black hole in GRS 1915+105 is known to be rotating with high spin, the black hole in IGR J17091−3624 is found to have a very low spin. In fact, for an inclination angle of 70° , which is favored by the data, the black hole could very well have a retrograde spin. In this case, IGR J17091−3624 would be the first known astrophysical source having a retrograde spin. Even though theoretically possible, such a scenario would be very challenging to explain from the point of view of evolution of such a system. Study of spectral parameters as a function of phases of the bursts shows that the two sources are not only similar in the appearance of the light curves with different variability classes, but also they show similar spectral variation with the phases of the bursts. This indicates a common mechanism in the two sources giving rise to similar variability behavior. With the help of phase-resolved spectroscopy and simultaneous spectral fitting, we were able to put important constraints on the system parameters. It was found that the source is a low mass black hole binary with a low spin ($a_* < 0.2$) at a distance of more than 20 kpc, by placing a similar constraint on peak luminosity as found by Neilsen et al. (2011) for GRS 1915+105. This work also shows that the simultaneous spectral fitting with a certain scheme of tying the parameters from different models can lead to tighter constraints on system parameters and a better understanding of accretion process dependent parameters.

Chapter 5

Quasi Periodic Oscillations

Black hole binaries are one of the highly variable astronomical objects with variability spanning a wide range of timescales. They are variable on timescales from milli-seconds to months and years. Their long term variability is best illustrated with commonly observed transient behavior where sources spend years in the quiescent states. On the other hand, their short term variability is best represented by quasi periodic oscillations (QPOs) seen in power density spectrum (PDS). QPOs appear as narrow features superimposed on the broad band continuum in PDS. Black hole binaries have shown QPOs in a broad range of frequencies 0.1-450 Hz (Remillard & McClintock, 2006) that has been divided into two categories; low frequency QPOs (0.1-30 Hz) and high frequency QPOs (40-450 Hz). It is expected that HFQPOs are related to the orbital motion of material in accretion disk because the orbital frequencies for the inner regions of disk around a black hole with mass of $\sim 10M_{\odot}$ and the frequencies of HFQPOs are of same order. In fact, typical frequencies of fast QPOs e.g. 150-450 Hz correspond to orbital frequencies at the ISCO for Schwarzschild black holes with mass 15-5 $M_{\odot}$ respectively (Remillard & McClintock, 2006). Though the exact modulation mechanism for HFQPOs is not yet clear, it is believed that these QPOs are the manifestations of various general relativistic effects in the orbits close to the black hole and hence are considered as vital tools to probe general relativity in strong field limit (Vincent et al., 2013; Rebusco et al., 2008). A detailed account of models on HFQPOs can be found in Stefanov (2014).

It is evident that the LFQPOs are not linked with the orbital motion of the material in the disk because the observed frequencies correspond to far outer regions of the accretion disk. The properties of these QPOs (e.g. low frequency break, centroid frequency, RMS amplitude) are strongly coupled with the changes in spectrum and luminosity (see Muno et al., 1999; Sobczak et al., 2000; Vignarca et al., 2003; Li et al., 2014), suggesting that these QPOs originate in the same inner region of the accretion disk. Despite the knowledge of empirical correlations of QPO properties with spectral parameters (e.g. Sobczak et al., 2000; Stiele et al., 2013), the exact physics is not very well understood. This chapter includes a brief description of LFQPOs followed by the details of a study performed to understand their origin. We make an attempt to study the mechanism of generation of QPOs by explaining its energy dependence with the help of simulation of light curves.

5.1 Low Frequency QPOs

There are adequate evidence revealing the link between the origin of LFQPOs and the power law component. A few of them are discussed here.

5.1.1 Relation between QPO properties and spectral parameters

Several empirical studies have been performed to understand QPO and their properties. The energy dependence of low frequency QPOs has been studied for several sources, e.g. GRS 1915+105 (Muno et al., 1999; Zhang et al., 2015; Rodriguez et al., 2004), H1743-322 (McClintock et al., 2009; Li et al., 2013b) GRO J1655-40 (Sobczak et al., 2000), XTE J1550-564 (Gierliński & Zdziarski, 2005; Li et al., 2013a) XTE J1650-500 (Gierliński & Zdziarski, 2005), GX 339-4 (Belloni et al., 2011), Cyg X-1 (Muñoz-Darias et al., 2010), and XTE J1752-223 (Muñoz-Darias et al., 2010). The increasing QPO amplitude with energy (e.g. Zhang et al., 2015; Li et al., 2013b; Rodriguez et al., 2004; Gierliński & Zdziarski, 2005) shows that the QPO is linked with the higher energy part of the spectrum and it is generally

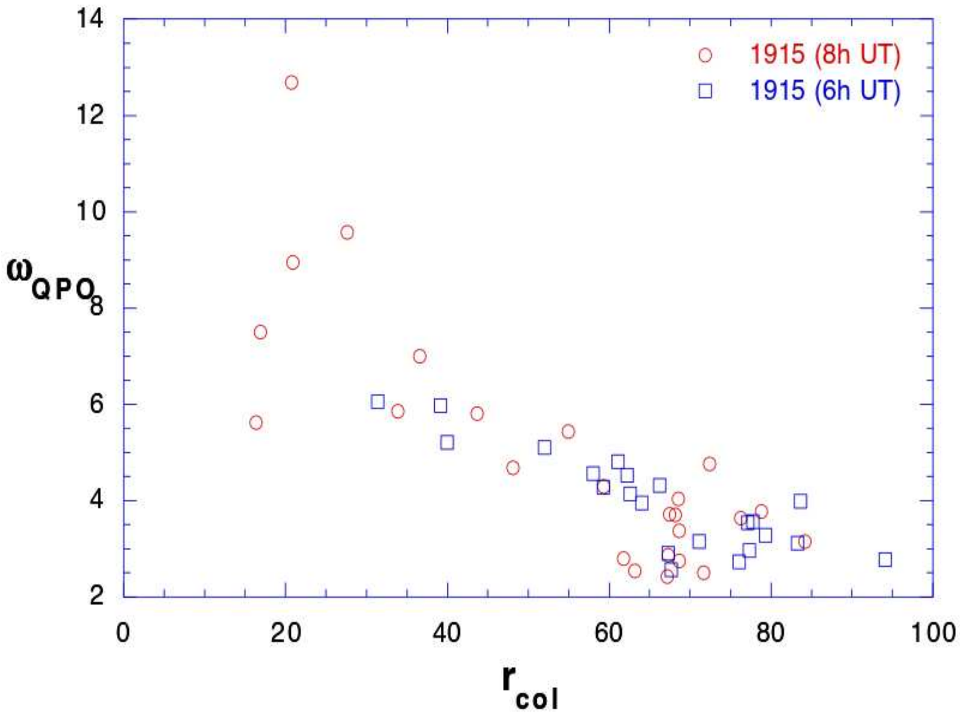

Figure 5.1: Figure showing the observed correlation between QPO frequency and the disk color radius. A tighter correlation is observed towards higher disk radius. Figure adapted from Rodriguez et al. (2002).

considered as an evidence supporting corona-origin for QPOs (Li et al., 2013b). In fact, several studies indicate that the power law component and the QPOs are generated from the same inner region by showing correlation between QPO properties and spectral parameters. For instance, Muno et al. (1999) studied QPOs from the source GRS 1915+105 with RXTE data and found LFQPOs in a range 0.5-10 Hz, apart from its HFQPO at 67 Hz. The authors have shown that 0.5-10 Hz QPOs are present during power law dominated states and the changes in luminosity are confined to changes in power law component. They showed that the QPOs with highest amplitudes occur at low values of disk flux. Morgan et al. (1997) suggest a more direct association between the QPO mechanism and the origin of Comptonizing electrons based on the rising amplitudes of QPO and sharp QPO profile at higher energies.

The features of energy spectra and power density spectra are found to be strongly correlated with one another by Markwardt et al. (1999) and they showed that 1-15 Hz QPOs appear when the power law component becomes hard and intense. The simultaneous presence of a strong, hard power law component during 1-15 Hz QPOs led them to suggest that the corona plays a vital role in the formation of QPOs. The correlation between QPO frequency and disk radius is shown by (Rodriguez et al., 2002, see Fig 5.1). Vadawale et al. (2001) studied simultaneous radio and X-ray observations of GRS 1915+105 during the presence of a huge radio flare. They showed that 0.5-10 Hz QPOs disappear and the Comptonization component becomes very weak during the dips observed in the light curves. The simultaneous disappearance of Comptonization component and the QPOs is another strong evidence connecting power law component and the origin of QPOs.

Overall, there are adequate number of evidence showing the origin of QPOs related to the Comptonization component, however the mechanism behind QPO modulations is far from being understood. Several models have been proposed to explain the observed properties of QPOs and a few are discussed here briefly.

5.1.2 Models for low frequency QPOs

Several models have been presented by different groups to explain LFQPOs and their observed properties. One of the most successful model is based on the relativistic Lense-Thirring precession of the inner hot flow (Stella & Vietri, 1998b; Wagoner et al., 2001b; Schnittman et al., 2006b; Ingram & Done, 2012, 2011). The model considers that the disk is truncated at a radius greater than R_{ISCO} during hard states and inner disk is replaced by a hot, geometrically thick, optically thin flow similar to ADAF (Narayan & Yi, 1995). The outer radius r_o of the hot flow marks the truncation of the disk. All the radii smaller than r_o contribute to the broad-band continuum at viscous frequencies and the Lense-Thirring precession of the entire hot flow superimposes the LFQPO on this continuum power (Ingram & Done, 2011). The model successfully explains the increase in QPO frequency and decrease in QPO width as the inner disk radius decreases.

The two component advective flow model (Chakrabarti & Titarchuk, 1995) proposes a disk with two distinct components: a component from the regions with viscosity above a critical value forming the Keplerian disk and a component from the regions with a lower viscosity which forms a shock wave due to centrifugal barrier. The post shock region acts as a Compton cloud producing power law component (Debnath et al., 2014). The shock oscillation model suggests that the LFQPOs are originated due to oscillation of this post shock region (Molteni et al., 1996; Chakrabarti et al., 2004; Garain et al., 2014).

Another model based on the accretion ejection instability suggests that a QPO is produced by a spiral pattern rotating at a frequency of a few tenths of the Keplerian frequency at the inner edge of the disk (Tagger & Pellat, 1999; Varnière et al., 2002; Rodriguez et al., 2002). A few other models include the radial and orbital oscillation model (Nowak & Wagoner, 1993; Nowak, 1994), global disk oscillation model (Titarchuk & Osherovich, 2000) and drift blob model (Hua et al., 1997; Böttcher & Liang, 1998, 1999).

Most of the available QPO models explain the frequencies and some of the observed correlations along with other timing and spectral properties. However, in most of the models variation of the spectral components is not accounted.

Observing a QPO as a direct oscillation of one or more spectral parameter could provide much deeper insights in the modulation mechanism and thus origin of the QPO. In this context, here we attempt to investigate the observed energy dependence of the LFQPO in GRS 1915+105 in terms of modulation of the spectral parameters. For this study, an observation of the source GRS 1915+105 is studied and details are discussed in the next section followed by our simulation procedure.

5.2 Observation

An observation of the confirmed black hole GRS 1915+105 carried out with NuSTAR on July 03, 2012 has been used for the present study. The data has been reduced with `NUSTARDAS` v1.4.1 available with HEASoft v 6.16. The data were screened and processed with *nupipeline* for the two modules separately. The source region was generated from a circular region of 90 arcseconds centered on the source. The background region was generated from a circular region of the same radius away from the source. The final products are generated with *nuproducts*. The light curves are generated with a binsize of 100 ms over the energy range of 3-80 keV. Smaller timebins resulted in many empty bins, therefore bin size was restricted to 100 ms.

5.3 Spectral Analysis

Spectral studies from the same observation has been shown by Miller et al. (2013). They showed that the spectrum is dominated by the power law component and it can be best described by a cut-off power law and its relativistically blurred reflection from the cold disk. In the present work, the spectrum is fitted with the same model i.e. `tbabs`$\times$`(kerrconv`$\otimes$`reflionx_hc) + cutoffpl`. In this model, reflection of cut-off power law is modeled by `reflionx_hc`, which is further blurred by `kerrconv`. Power law index and cut-off energy are tied across `reflionx_hc` and `cutoffpl`. The absorption is fitted with `tbabs` using corresponding abundances (‘wilm’, Wilms et al., 2000) and cross sections (‘vern’, Verner et al., 1996). The model gives a statistically acceptable fit to the spectrum with $\Delta\chi^2$ value of 1.06. The constant used to account for the calibration uncertainties of the two detectors is found to be 1.02. The best fit parameters are shown in Table (5.1). This best spectral fit is later used while simulating light curves. The spectra from both the modules fitted with the best-fit model of Miller et al. (2013) is shown in Fig (5.2).

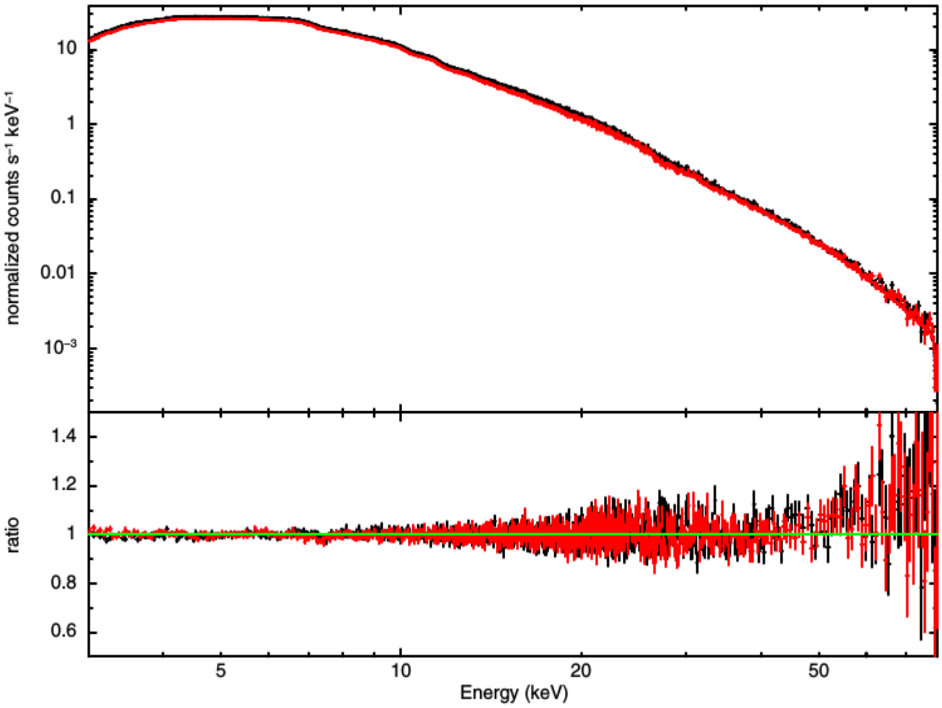

Figure 5.2: NuSTAR spectrum fitted simultaneously for FPMA and FPMB with the model `tbabs`$\times$`(kerrconv`$\otimes$`reflionx_hc) + cutoffpl`. Figure adapted from Miller et al. (2013).

5.4 Timing Analysis

Zhang et al. (2015, hereafter Z15) have presented the timing analysis of the same observation and detected a QPO at $\sim$1.5 Hz along with a peak at $\sim$0.75 Hz, which is suggested to be a subharmonic of the former by Z15. PDS for the observation is shown in Fig (5.3). In the present study, the subharmonic peak and the low frequency noise are not considered while simulating light curves. Spikes are seen

Table 5.1: The best fit spectral parameters calculated with the model `tbabs`$\times$(`kerrconv`$\otimes$`reflionx_hc + cutoffpl`). Errors indicate 90% confidence intervals. N_{ref} and N_{pl} represent the normalization for `reflionx_hc` and `cutoffpl` respectively.

Parameter	Best fit value
N_H ($\times 10^{22}$cm^{-2})	$4.40^{+0.04}_{-0.04}$
Index 1	$9.94^{+0.04}_{-0.06}$
Index 2	0
R_{in} (R_g)	$6.94^{+0.04}_{-0.06}$
a_*	$0.982887^{+0.000006}_{-0.000041}$
Γ	$1.70^{+0.001}_{-0.001}$
Xi	982^{+17}_{-21}
Inclination (i)	70.0
Cut-off Energy	$35.28^{+0.19}_{-0.16}$
N_{ref} ($\times 10^{-5}$)	$1.27^{+0.40}_{-0.02}$
N_{pl}	$1.86676^{+0.009}_{-0.007}$

in the PDS at every 1 Hz, known to be artifacts in the earlier observations of NuSTAR. These spikes are ignored in XSPEC while fitting PDS with multiple lorentzians. Z15 showed that the QPO remains at a frequency of ∼1.5 Hz, however sharply increases to ∼1.9 Hz after the first ∼40 ks of observation accompanied by a rise in the count rate. Therefore, spectral and timing analysis are restricted to the first 40 ks of observation, where the count rate and the QPO frequency remain quite stable. The effective exposure times for analysis are 9.71 ks and 10.01 ks for FPMA and FPMB respectively.

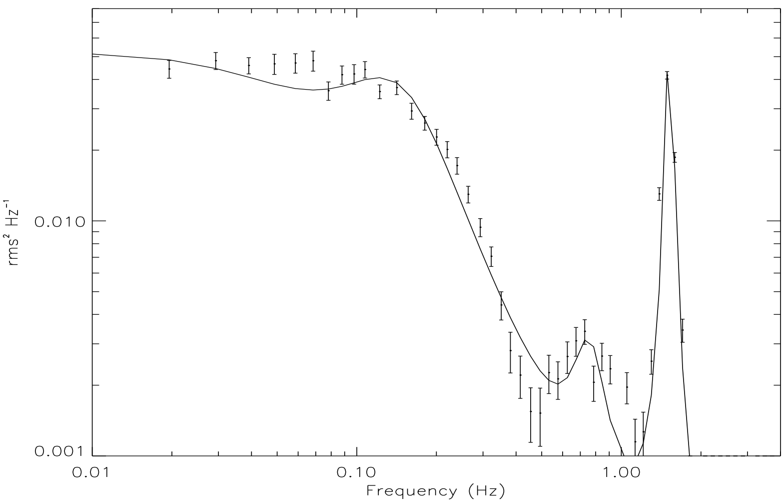

Figure 5.3: Figure shows the observed PDS in the energy range of 3-80 keV. A QPO is seen at ∼1.5 Hz.

Z15 studied the energy dependence of the QPO and found that the RMS amplitude of the QPO increases with energy. They also reported a flattening around 10-20 keV. The energy dependence is verified by generating the light curves and PDS in different energy bands (3−4 keV, 4−5 keV, 5−6 keV, 6−7 keV, 7−9 keV, 9−12 keV, 12−15 keV, 15−19 keV, and 19-30 keV). In order to improve the statistics, the light curves from FPMA and FMPB are added together for each energy bin and PDS are generated from the added light curves. Multiple lorentzians are used to fit the PDS and the normalization of the lorentzian representing QPO is used as RMS power of the QPO. PDS fitted with multiple lorentzians are shown in Fig (5.4) for different energy ranges. Fig (5.5) shows the increasing power of the QPO along with a shallow dip or flattening between 10-20 keV as reported by Z15.

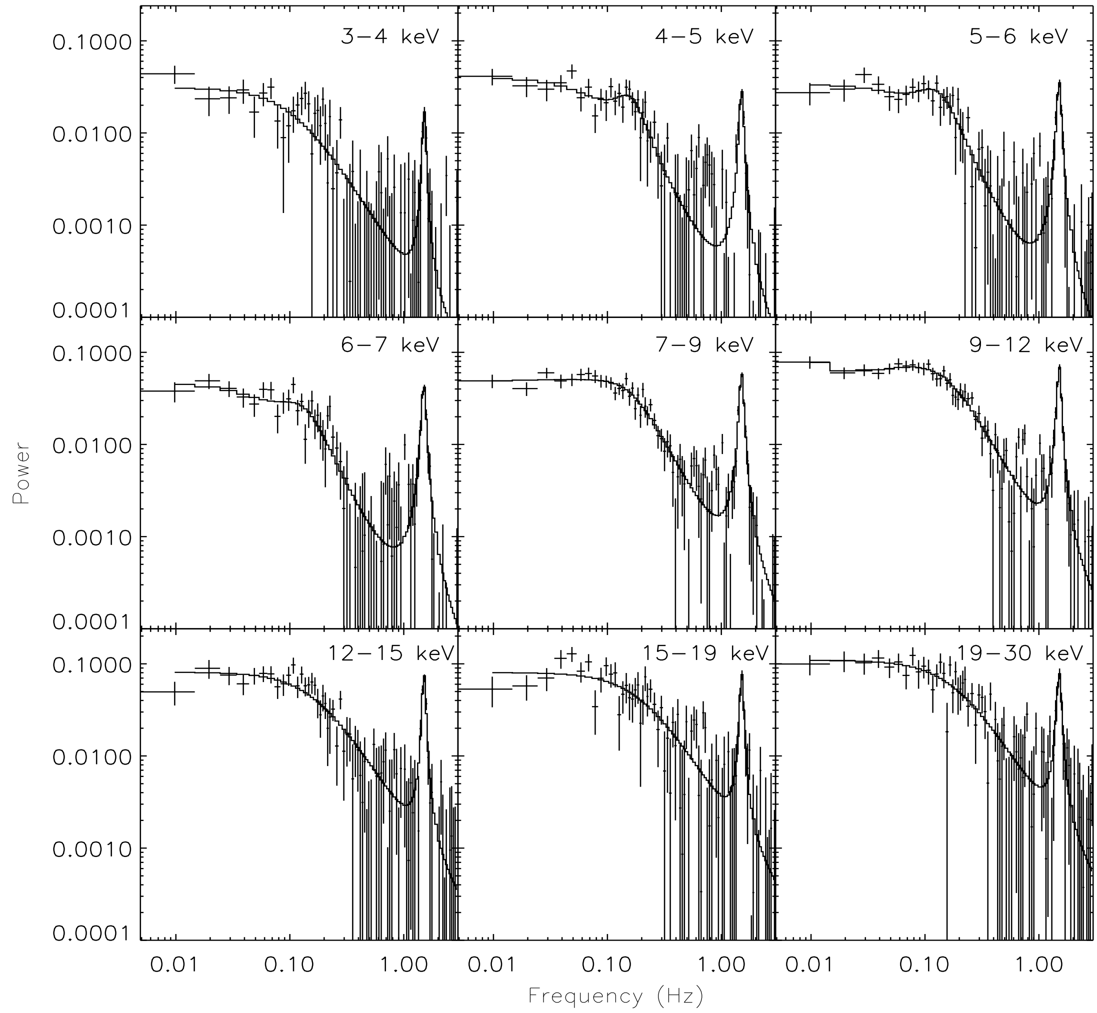

Figure 5.4: Observed PDS in different energy ranges fitted with multiple lorentzians. Power is given in units of 'rms^2 Hz^{-1}' The energy range is mentioned in top right corner of each of the panels.

5.5 Light Curve Simulation

Different spectral models can give equally statistically acceptable fit to an observed spectrum with physically acceptable set of parameters. However, timing properties can play an important role to further test the compatibility of spectrum and model. In the present work the compatibility of QPO properties with the spectral modeling has been studied along with the mechanism behind generation

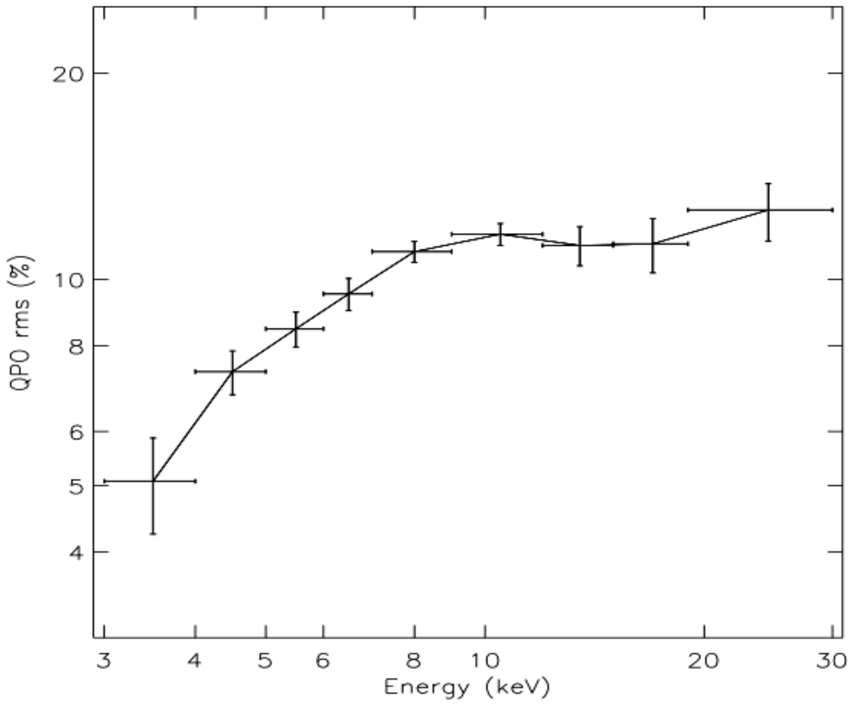

Figure 5.5: The figure shows the energy dependence of the QPO. A shallow dip or flattening is seen between 10-20 keV.

of QPO. The best fit model consists of only one primary continuum component i.e. `cutoffpl` covering the full energy range. Therefore, the model does not allow the interpretation of QPO in terms of oscillation of one of the spectral components as suggested by Rao et al. (2000) and Vadawale et al. (2001, 2003). Therefore, we consider the variation of one or more spectral parameters and using this we investigate the observed energy dependence of the QPO. We start by simulating the light curve and a detailed description is given here.

The hypothesis of varying spectral parameters with the phases of QPO is tested by simulating the light curves consisting of QPO and comparing the obtained energy dependence of QPO with the observed one. Light curves are simulated with a binsize of 100 ms, same as the binsize of the observed light curve. The parameters are assumed to vary sinusoidally in a range centered at the best fit value. A small random variation is superimposed on the sinusoidal variation to be a bit more realistic. The light curves are simulated over energy bands same as those used to generate energy dependence of the observed QPO.

A list of spectral parameters is given in Table (5.1). We consider the variation of four spectral parameters viz. spectral index (Γ), normalization of cut-off power law (N_{pl}), normalization of reflection component (N_{ref}) and ionization parameter (Xi). The cut-off energy can be assumed to vary with the QPO phases, however its variation does not affect the model in the energy range of interest. Also, the parameters of `kerrconv` are not assumed to vary with phases of the QPO. At first, the variation of single parameter is studied and then the simultaneous variation of multiple parameters is considered. Fig (5.9) shows the variation of three parameters, Γ, N_{ref}, N_{pl}.

It is assumed that a parameter α obtained from the best-fit spectral model varies at a frequency close to the observed QPO frequency ($\bar{\nu}$). The amplitudes of the sinusoidal variation and random fluctuation are p_α and q_α respectively such that $q_\alpha =$ r p_α. The simulation is repeated for r=0.1, 0.2, and 0.3 and it is found that the results remain unaffected. Therefore, we present the results hereafter for r=0.1 unless otherwise mentioned.

- Let m_α be the best fit value of parameter α.

- The spectral model is evaluated in `XSPEC` with the parameter α assuming values in the range $m_\alpha \pm p_\alpha$, keeping the rest of the parameters at their best fit values. Model counts, including the effects of detector response matrix as well as effective area, are obtained in each of the energy bins and are tabulated.

- The light curve is simulated with a bin size of 100 ms for a duration of $\sim$ 10 ks to match the exposure time of the observation.

- For each interval ($\sim$ 2 s) a random frequency of oscillation (ν) is drawn from a lorentzian distribution with the mean $\bar{\nu}$ (=1.5 Hz) and the FWHM values same as those for the observed QPO. The frequency remains the same throughout an interval. We have also verified that the overall results remain unaffected if the frequency is changed more often within one interval.

- The phase of oscillation for each time bin i is obtained by

$$\phi_i = 2\ \pi\ \nu\ \Delta t\ +\ \phi_{i-1}$$

where Δt is the bin size and ϕ_{i-1} is the phase for previous time bin. Continuity of the phases across intervals is also maintained in the same manner.

- The value assumed by parameter α for the i-th timebin is calculated as

$$\alpha_i = p_\alpha\ sin(\phi_i) + q_\alpha\ z$$

where z is a standard normal variate.

- Mean counts in the time bin i for a given energy bin j ($\bar{C}_{ji}$) corresponding to value α_i is obtained from the table generated in the first step. The energy bin j is kept same as that used to extract the observed light curves.

- Random number is generated from Poisson distribution with mean $\bar{C}_{ji}$ and is recorded as counts in the i-th time bin of the light curve in energy bin j.

- Power density spectra are generated for these simulated light curves using `POWSPEC` and are fitted in `XSPEC` as usual.

5.6 Simulation Results

A 9-12 keV light curve simulated by varying spectral index and its PDS are shown in Fig (5.6). The lower-left panel shows the zoomed-in view of a section of light curve. The absence of low-frequency continuum and the subharmonic peak can be observed in the simulated PDS. Results of simulation are discussed in the following two sections.

5.6.1 Simulation with One Parameter

The results obtained from the variation of single parameters are shown in Fig (5.7). The observed energy dependence is shown with black solid line in all the panels. Multiple lines in each panel correspond to different amplitude of variation of

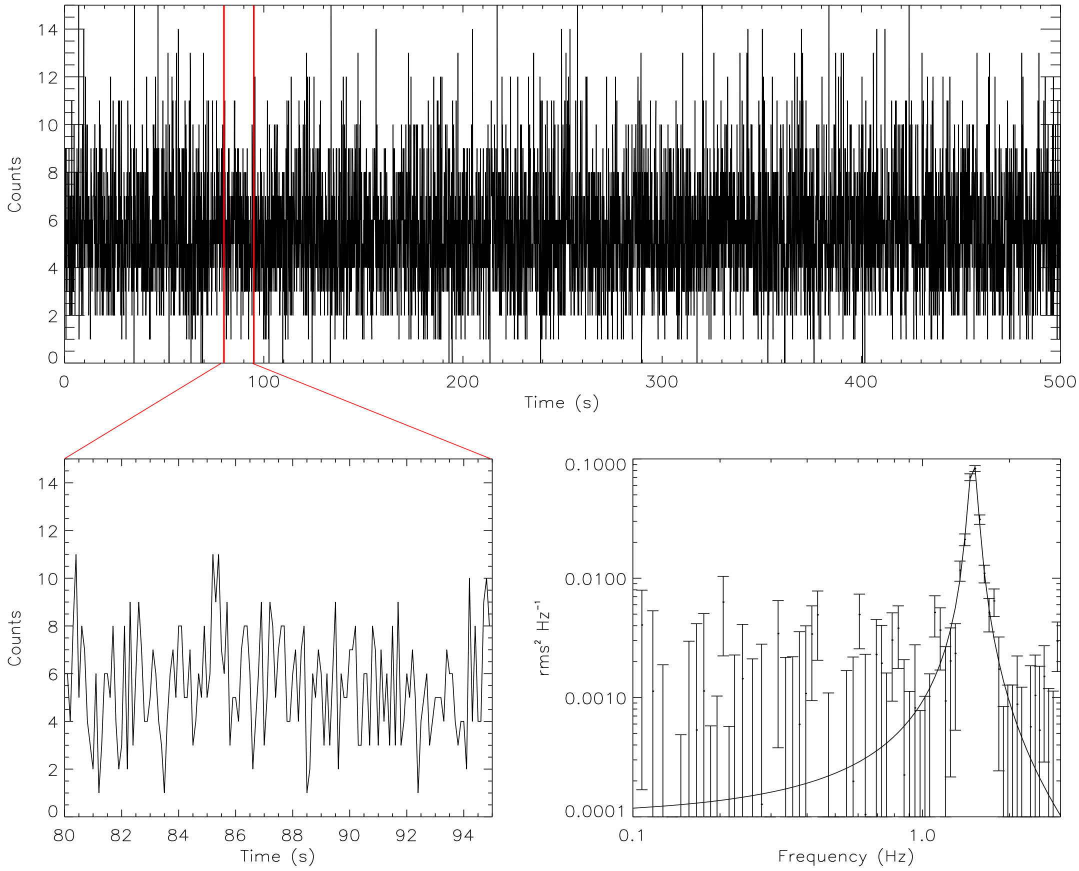

Figure 5.6: The upper panel shows the first 500 seconds of a 9-12 keV light curve simulated by modulating the spectral index. A zoomed-in view of a section of the light curve is shown in the lower-left panel. PDS of the full light curve is shown in lower right panel.

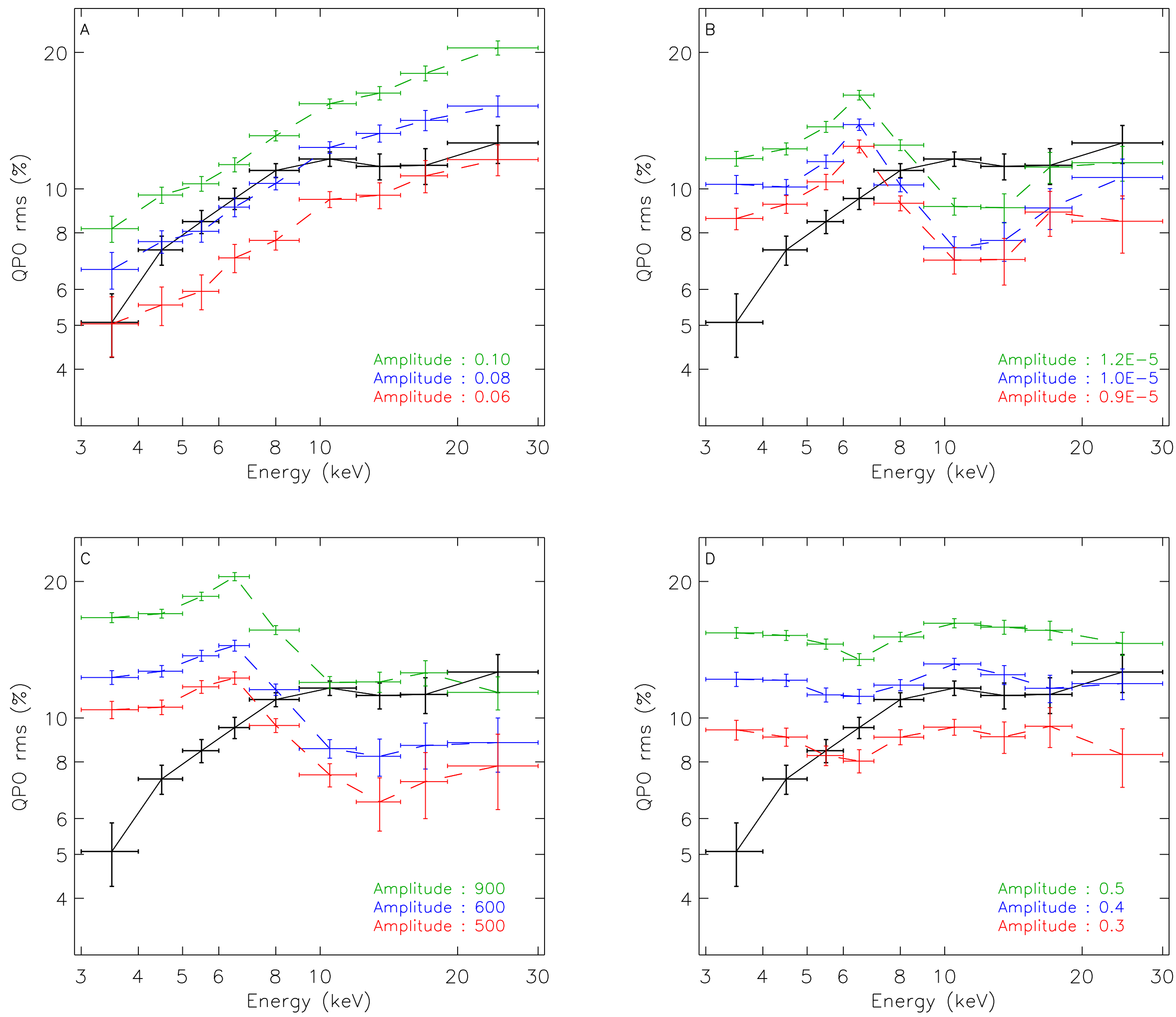

Figure 5.7: Figure shows the simulated energy dependence of QPO obtained by modulation of spectral index (A), normalization of reflionx_hc (B), ionization parameter (C) and normalization of cut-off power law (D). The dashed lines correspond to simulation results for different amplitudes of modulation. The observed energy dependence is shown with black solid line in all the panels.

parameters. It is clear that the energy dependence obtained with the variation of spectral index only matches with the overall increasing trend of QPO power with energy. However, a dip or flattening is not seen between 10-20 keV in the simulated results. Variation of other three parameters does not reproduce the observed energy dependence. Particularly, the variation of normalization of cut-off power law remains flat and hence, does not provide any energy dependence. Absence of dip or flattening in the simulation results suggests that the variation of spectral index is essential during QPO phases, however it is not the only source of variability.

5.6.2 Simulation with Two Parameters

We further test the hypothesis by simulating the light curves considering the variation of more than one parameter simultaneously. The simulation was repeated for the variation of two and three parameters and the results are shown in Fig (5.8) and (5.10) respectively. Since the reflection component represents the Comptonization component reflected from the disk, it is expected that the former would be stronger for a harder spectrum. Or in other words, the reflection component should be anti-correlated with the spectral index. Therefore, the parameters of reflection component (N_{ref} and Xi) were varied out of phase with spectral index in the simulation of light curves. Panel A of Fig (5.8) shows the energy dependence obtained from the variation of reflection normalization (N_{ref}) and spectral index and Panel B shows the results for ionization parameter (Xi) and spectral index. A comparison of Panel A of Fig (5.7) and Fig (5.8) shows that the variation of spectral index and normalization of reflection reproduce the observed energy dependence more closely than the variation of spectral index alone. We also studied the energy dependence with the light curves simulated by varying 1) normalization of cut-off power law and normalization of reflection component and 2) normalization of cut-off power law and ionization parameter. The variation of the two set of parameters does not reproduce the observed increasing trend of QPO power.

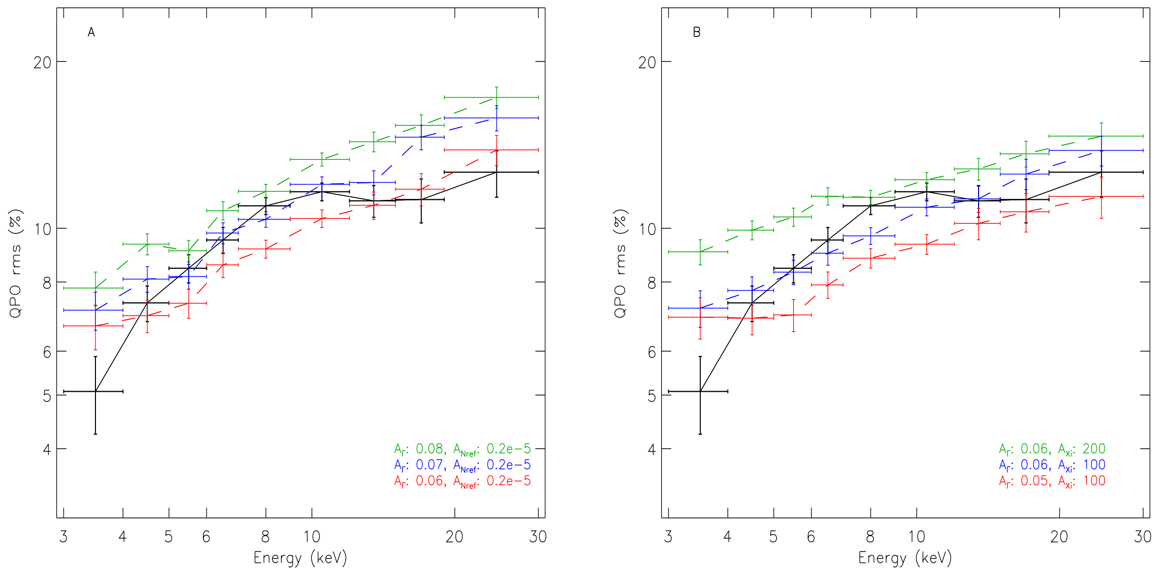

Figure 5.8: Plot showing the energy dependence of QPO with the simulated light curves by varying two parameter simultaneously. Panel A shows the results obtained from the variation of normalization of reflection and spectral index. Panel B shows the result for the variation of ionization parameter and spectral index. The dashed lines correspond to simulation results for different amplitudes of modulation. The observed energy dependence is shown with black solid line in both the panels.

5.6.3 Simulation with Three Parameters

Fig (5.9) shows the variation of the three spectral parameters with the vertical lines separating the neighboring intervals. Indicative results from the variation of three parameters are shown in Fig (5.10). The energy dependence matches with the observed one more closely. However, we do not attempt to exactly reproduce the observed pattern as this would require a detailed fine tuning of number of varying parameters, amplitudes of variation and phase lags etc. Overall, it can be concluded that the spectral model is compatible with the observed energy dependence of QPO by considering the variation of spectral index at frequencies close to QPO frequency.

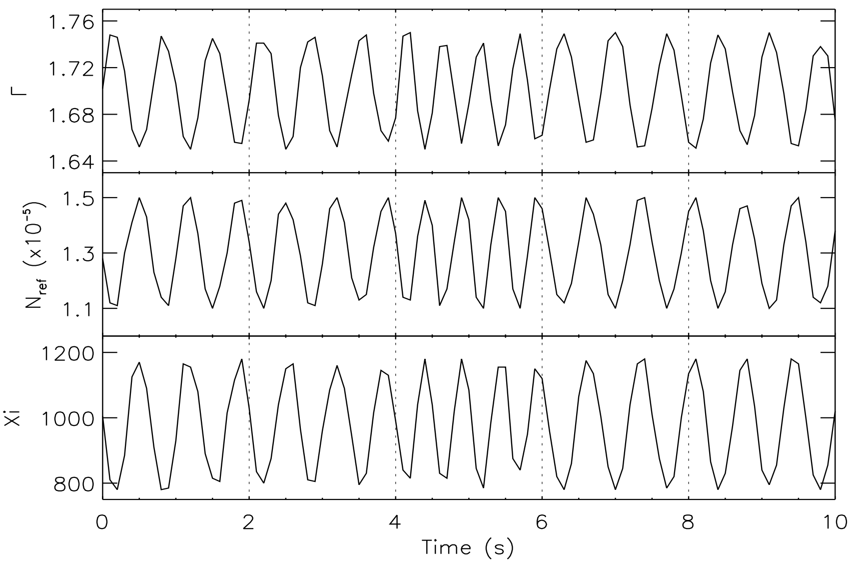

Figure 5.9: The figure shows the variation of three spectral parameters; spectral index (Γ), reflionx_hc normalization (N_{ref}), and ionization parameter (Xi). The reflection normalization and ionization are varied in same phase which are assumed to be anti-correlated to the phase of spectral index variation. The dashed lines separate the intervals corresponding to different frequencies of modulation.

Among the other existing models for the low frequency QPOs, the model based on Lense-Thirring precession is considered the most successful model. It successfully explains the overall shape of the PDS and the variation of QPO frequency with the changes in spectral hardness, which is further linked with the

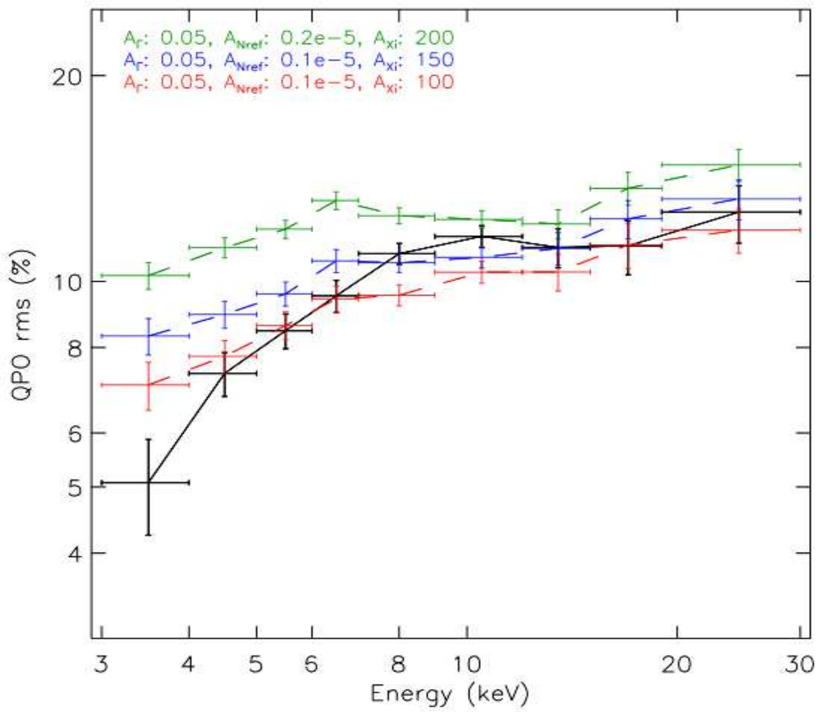

Figure 5.10: The figure shows the energy dependence of QPO power obtained from the simulated light curves generated by modulation of three parameters. Amplitudes of modulation for Γ, N_{ref}, and Xi are mentioned in the figure. The black solid line shows the observed energy dependence.

truncation radius of the inner disk (Ingram & Done, 2010). However, the energy dependence of QPO is not apparently clear. The similar situation exists with a magnetohydrodynamic model for QPO based on the accretion ejection instability (Tagger & Pellat, 1999; Varnière et al., 2002; Rodriguez et al., 2002). The shock oscillation model (Molteni et al., 1996; Chakrabarti et al., 2004; Garain et al., 2014) does produce the spectral variation and it could be compatible with the energy dependent QPO power. However, the simulation results obtained from the present spectral model cannot be directly compared with the predictions of shock oscillation model. It might be necessary to perform similar simulation with appropriate model and then verify the results.

Another observation is the flattening of QPO spectrum at 10-20 keV which cannot be reproduced with variation of only spectral index. The flattening seems to be more common as it has been observed at many other occasions. Similar feature is also found in few other sources (Li et al., 2013b). We have verified that the same feature is found in the RXTE observations of GRS 1915+105 during the 'plateau' states. We fit the spectra during these observations with the present spectral model consisting of cut-off power law and relativistically blurred reflection. The best fit spectral parameters are similar to that found for the present NuSTAR spectrum. We performed similar simulations using RXTE spectra and could reproduce the overall trend of increasing power of QPO. However, the flattening is not found in the simulation results. The observed flattening might be an indicator of the presence of more than one continuum component as suggested by Rodriguez et al. (2004).

It is noticeable here that the values of rms amplitude obtained from NuSTAR are affected by dead time and the calculated values are smaller than its real values (see Bachetti et al., 2015). However, the present work mainly focusses on the energy dependence of rms amplitude. The increasing rms amplitude with energy seems to be a generic behavior and it has been shown by many authors using data from NuSTAR (e.g. Zhang et al., 2015) and RXTE (e.g. Li et al., 2013b; Rodriguez et al., 2004) as well. In the present work, the energy dependence is found to be reproduced with oscillation of power law index. Therefore, the energy dependence will be reproduced with the simulation even if the observed rms amplitude is replaced with dead time corrected values. This is again clear from Fig (5.7 ,5.8, and 5.10) as the increasing trend is reproduced with different amplitudes of oscillation of parameters.

Overall our simulation results can put significant constraints on the modulation mechanism assumed in various present theoretical models of QPO. Recently, Axelsson & Done (2015) showed frequency-resolved spectroscopy to understand QPOs. The phase-resolved spectroscopy similar to that shown by Ingram & van der Klis (2015) can also be promising, but with full energy resolution spectra. Forthcoming Indian astronomy mission Astrosat (Singh et al., 2014) will provide ample opportunities for such QPO phase-resolved spectroscopy owing to its event mode data over broad energy range.

5.7 Phase-resolved Spectroscopy for QPO Phases

Phase-resolved spectroscopy is a promising method to study periodic/quasi-periodic signals and evolution of spectral parameters with phases. This method proved to be very crucial in the study of quasi periodic 'heartbeats' discussed in the previous chapter. The method is expected to give important insights into QPO mechanism as well however, there are several constraints in the phase-resolved spectroscopy for QPOs. Generally, QPOs observed in black hole binaries are weaker (about $<$30% RMS) and the features are not visibly distinguishable from the other frequency components in the light curve. Consequently, it is difficult to separate the QPO phases except in the case of very strong QPOs e.g. in Miller & Homan (2005) where the QPO features visibly dominate the light curve. Another obstacle in such studies is the timescale of this phenomenon. Given the frequency range of LFQPOs (0.1-30 Hz, Remillard & McClintock, 2006), spectra of phases have to be generated that last typically few milli-seconds. The statistics is generally limited by less number of photons at such timescales and hence, study is restricted to very bright sources. Among the available facilities, RXTE data is mostly used for QPO studies, however its Standard 2 data cannot be used to study

QPO phases as its timing resolution is 16 seconds. Although, event and binned mode data provide better timing resolution, the spectrum lacks energy resolution. Moreover, the origin of QPO has always been linked with the Comptonization component (e.g. Morgan et al., 1997; Muno et al., 1999; Markwardt et al., 1999) that dominate towards higher energy. Therefore, the availability of higher energy coverage is inevitable in order to study QPO and Comptonization component together. Overall, phase-resolved spectroscopy requires better timing resolution, higher energy coverage and a bright source. This became possible with the mission NuSTAR which gives good time resolution of the order of 0.1 ms and a harder energy coverage of 3-80 keV. The higher energy coverage with a better timing resolution makes NuSTAR data very helpful for the phase-resolved spectroscopy of QPO phases.

We performed the phase-resolved spectroscopy for the same NuSTAR observation that is used in the simulation. Since the simulation, timing and spectral studies are performed for the first interval, phase-resolved spectroscopy is also performed from the same interval. Following section explains the extraction of QPO profile, which is further used for defining phases and generating their spectrum.

5.7.1 Extraction of QPO Profile

We need to define QPO phases before extracting spectra and performing phase-resolved spectroscopy. However, it is generally difficult in case of QPOs owing to its weak strength and quasi periodicity. Also, QPO modulations are generally accompanied by other variability features in the light curves. Therefore, different authors have used various techniques. For instance, Miller & Homan (2005) studied RXTE observations of GRS 1915+105 and presented the phase-resolved spectroscopy for QPO. The QPO is strong in their observations ($\sim$ 14% RMS amplitude) and the modulations dominate the variability in the light curve. In order to define the QPO phases, they divided the light curve based on count rate and generated spectra for high and low phases. Recently, Ingram & van der Klis (2015) studied QPO from GRS 1915+105 using RXTE data and utilized the

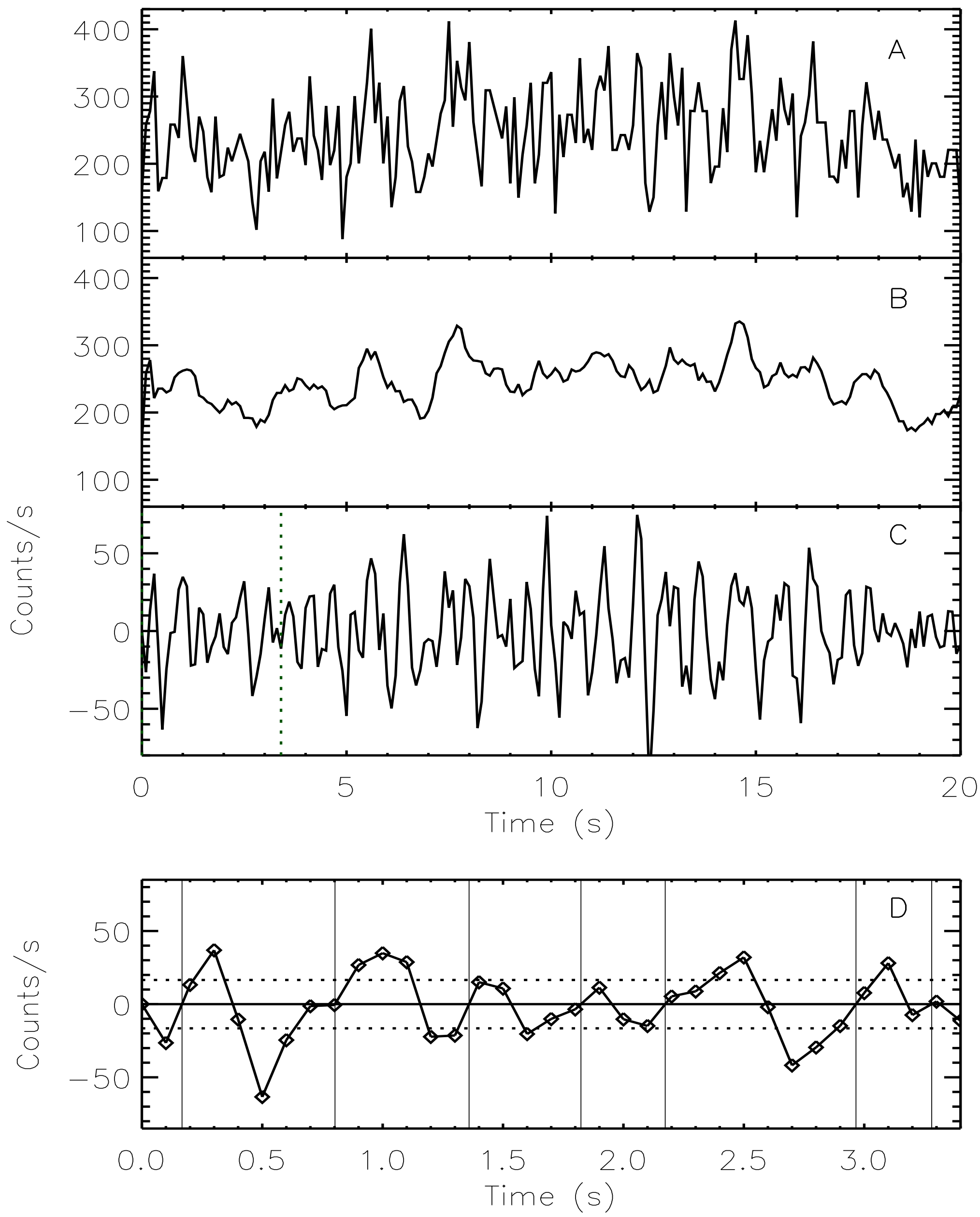

Figure 5.11: A multi-panel plot showing observed light curve (A), averaged light curve (B) exhibiting long term variations, QPO profile (C) and a zoomed-in view of a section demarcated by dotted lines (D). The vertical lines in panel (D) are drawn at zero-crossing times separating neighboring QPO cycles. The solid horizontal line is drawn at the mean value in panel D. Horizontal dashed lines are drawn at half of the standard deviation from the mean value in both the sides.

presence of harmonic peak to extract QPO profile and define QPO phases. The authors were able to reconstruct QPO waveform by using the phase difference and amplitude ratios of the first two harmonics. In the present case of NuSTAR observation, the QPO is weak ($\sim$ 8% RMS amplitude) and therefore, phases of QPO are defined using a different approach. It is clear from Fig (5.3) that the observed PDS consists of low-frequency continuum and a subharmonic peak around $\sim$0.75 Hz along with the QPO at $\sim$1.5 Hz. In order to extract the modulations due to QPO, a small range of frequencies centered at 1.5 Hz have to be retained. Therefore, we separated the QPO modulations from the other variability features in the following manner.

Since the light curve is binned at 100 ms and the QPO period is 666 ms, the light curve is averaged by a factor of 7. This averaged light curve contains all the long term variability. Panel A and B of Fig (5.11) show the first 20 seconds of the original and averaged light curves respectively. The subtraction of averaged light curve from the original light curve results in a light curve which is free from long term variability. We average the resulting light curve again by a factor of 3 to remove faster variability. The final light curve which consists of the QPO profile, shown in panel C of Fig (5.11), is expected to retain only QPO modulations. Panel D shows a zoomed-in view of a section of final light curve. The PDS of final light curve is expected to retain frequency components in range of (1/0.7 s^{-1}) to (1/0.3 s^{-1}) i.e. 1.42-3.33 Hz. The QPO profile shown in panel D clearly shows modulations in the light curve. This is verified by generating its PDS which is shown in Fig (5.12). The continuum and low-frequencies are absent in the PDS and it shows only QPO frequencies. The QPO profile is further used to define phases.

5.7.2 Spectral Analysis

QPO cycles can be separated by finding peaks, however peak identification can be ambiguous in this case. Therefore, zero-crossing times with positive slope are found from the QPO profile. The interval between consecutive zero-crossing times gives the length of a QPO cycle. In this way QPO cycles are identified and divided

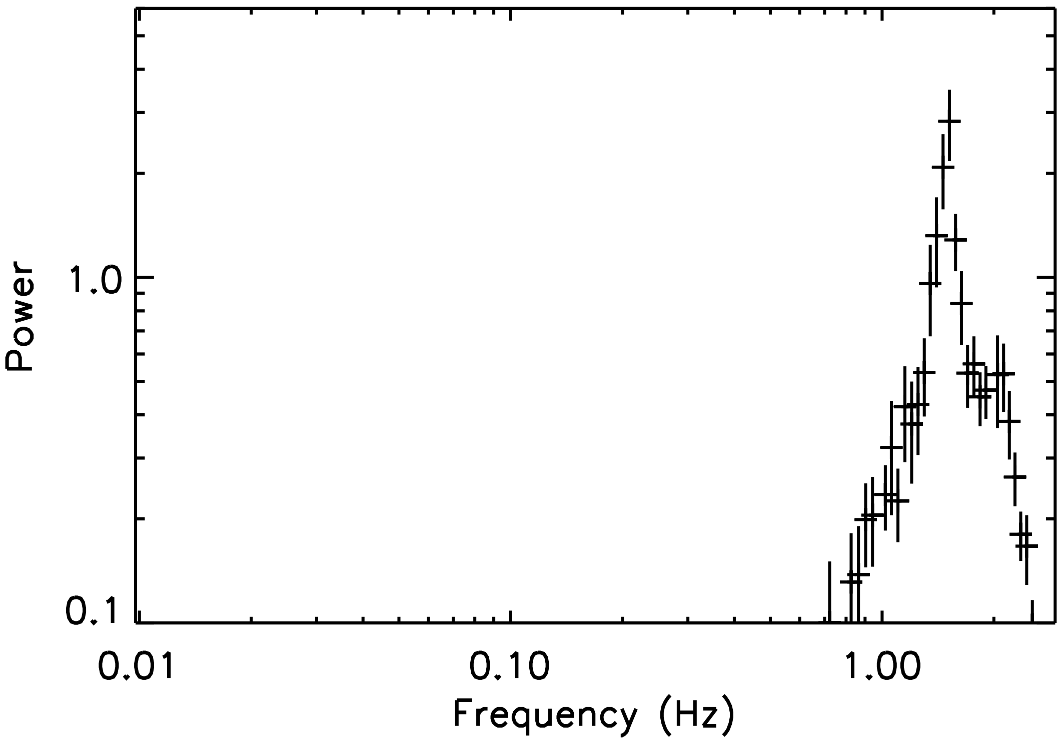

Figure 5.12: Power density spectrum for QPO modulations. The absence of low-frequency continuum and subharmonic peak is evident in the PDS.

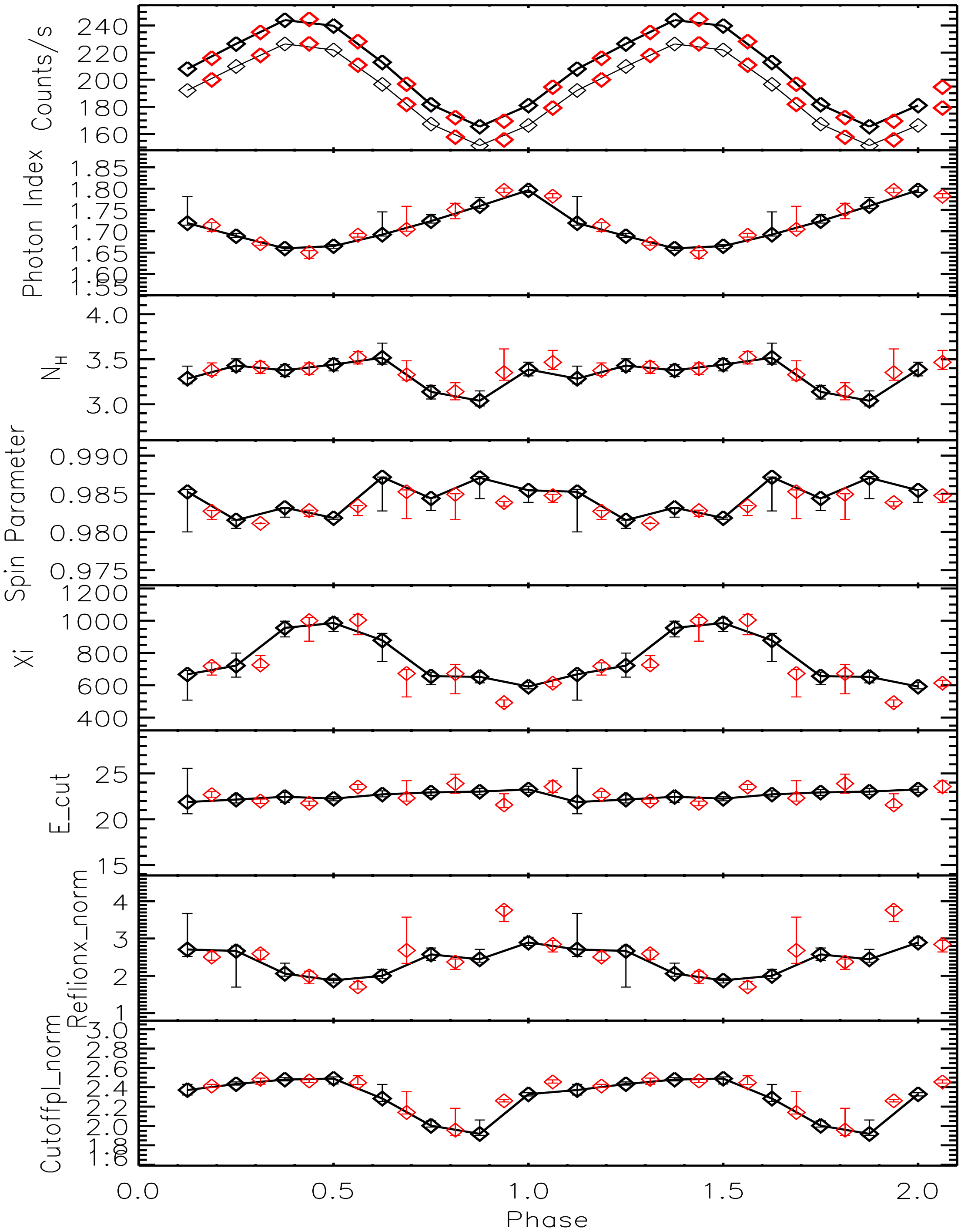

Figure 5.13: A multi-panel plot showing variation of spectral parameters with phases of QPO. The results are obtained from the phase-resolved spectroscopy performed for QPO phases. The first panel shows the count rate obtained from the two modules. The points shown with red are obtained by shifting the phases of the QPO by a fixed amount. N_H and `reflionx_hc` normalization are given in units of 10^{22} cm^{-2} and 10^{-5} respectively.

into 8 phases of equal length. Good Time Interval (GTI) files are created for 8 phases and spectra are extracted for FPMA and FPMB separately. Each spectra is fitted separately with the same model as explained in section 5.3. Emissivity indices are frozen at the values obtained from the time-integrated spectra. Also, inclination angle is frozen at 70°. All spectra give a statistically acceptable fit. Fig (5.13) shows variation of the spectral parameters with QPO phases. A cyclic variation centered at a value of about 1.7 is observed in the spectral index, which is consistent with the value obtained from phase-integrated spectrum. This justifies our assumption of varying spectral index in the simulation of light curve. It is noticed that the spin parameter from all the phase spectra is close to 0.98. This result along with the results shown by Miller et al. (2013) show that the hard state spectra studied in this observation, gives a very accurate measurement of spin with the help of reflection component, though the disk may be truncated at a larger radius.

5.8 Summary

Increasing trend of the LFQPO power with energy is well known (e.g. Tomsick & Kaaret, 2001; Rodriguez et al., 2004, 2008; Zdziarski et al., 2005; Sobolewska & Życki, 2006). However, origin of this trend in terms of variation of the spectral components has not been investigated so far. Here we attempt to explain the energy dependence of LFQPO observed during the first NuSTAR observation of GRS 1915+105. We simulate the light curve for variation of various spectral parameters and compare the resultant energy dependence with the observed one. We find that the variation of the spectral index reproduces the overall trend of the increasing QPO power with energy. Variation of any other parameter does not reproduce the observed trend. Our results provide strong constraints on the models explaining mechanism behind QPO modulations. As a result of this study, the variation of spectral index has surfaced as an important element of the mechanism behind QPO generation, which is further confirmed with the phase-resolved spectroscopy.

Chapter 6

Summary and Future Scope

6.1 Summary

Stellar mass black holes are the end products of evolution of a massive star. Towards the end stages of stellar evolution, the outward thermal pressure reduces and the core of the star is crushed under the gravity of its own mass. The core collapse of a massive star can result in a black hole or a neutron star. If the remnant is very compact such that its size is smaller than Schwarzschild radius, the end product is a black hole. Stellar mass black holes generated from the core collapse of a massive star are expected to have mass in a range of 3-20 $M_{\odot}$. The estimates of mass for the observed black holes in the binary systems lie well within this limit (see RM06). Since no information or photon can escape from the regions within the event horizon, it is difficult to detect a single stellar mass black hole. However, their detection becomes relatively easier if the black hole is a member of mass transferring binary system. In fact, all the binaries transfer mass during certain stages of binary evolution. The mass transferred from the companion star has high specific angular momentum. The conservation of angular momentum and the compactness of the accreting star facilitates the formation of accretion disk around black hole. Material in the accretion disks revolves in circular Keplerian orbits with a small radially inward drift. Accretion disks are the most efficient machines to extract the gravitational potential energy of the material in the disk. A fraction of the extracted energy is radiated in the form of

X-rays.

A significant fraction of the observed X-rays is originated from the inner regions of accretion disk. This is the region where temperature is very high and the gravitational field of the black hole is strongest. Therefore, study of these sources in X-rays gives an opportunity to study the behavior of matter in the extreme conditions of temperature and gravitational field, which cannot be generated in a laboratory. Accretion disks are of great importance not only in the detection of stellar mass black holes, but also for our understanding of the physics of accretion.

Accreting black hole binaries have shown a wide variety of spectral and timing properties. Although, variations in spectral behavior is seen in almost all the black hole binaries, extreme variability is seen only in few black hole sources. Variability of spectrum is explained with different spectral states, occurrence of which are generally understood with the disk truncation model. The model suggests that the disk extends close towards the black hole and it may even approach ISCO during the soft states. However, the disk remains truncated at a higher radius during the hard states. The inner disk is replaced by a radially inefficient flow similar to ADAF (Narayan and Yi, 1995). The model has been very successful to explain different spectral states in terms of variation of the truncation radius. Recently, few observational results showed the inner disk radius at smaller Schwarzschild radii during hard states. The work shown in Chapter 3 shows that our results strongly support the disk truncation model. A black hole candidate MAXI J1659−152, discovered during early hard stages with MAXI is studied. The source remained in the outburst state for about one and a half months and the outburst is covered extensively with Swift and RXTE. We study 80 spectra from Swift observations and fit them simultaneously in groups. Evolution of different spectral parameters is studied during the outburst. It is found that the inner disk radius is truncated during early hard stages of the outburst and it decreases as the source transitions towards softer states. Our results support the disk truncation model among the growing evidence against it. Mass of the black hole is estimated to be $8.1\pm2.9\ M_{\odot}$.

Along with a variety of spectra, black hole binaries are also known for showing different variability behavior. However, extreme variability is exhibited by only a few sources. In the present thesis, a certain class of variability called 'heartbeats' is studied for the two sources viz. GRS 1915+105 and IGR J17091−3624. The legendary source GRS 1915+105 is known for showing extreme variability, however IGR J17091−3624 was observed to show variability similar to GRS 1915+105 during its 2011 outburst. 'Heartbeats' of the the two sources are studied comparatively with the help of phase-resolved spectroscopy for the phases of the bursts. Spectra were studied both with relativistic and non-relativistic models, which finally leads to the important constraints on mass, inclination angle, spin and distance of IGR J17091−3624. It is found that the source is a low mass black hole with mass $< 5M_{\odot}$. The distance to the binary is estimated to be > 20 kpc with an inclination angle $> 53°$. We find that the source is low spin black hole with spin parameter < 0.2, including negative values of spin parameter, which suggests a retrograde spin of the black hole. Although both the sources show similar variability behavior, IGR J17091−3624 is about 20 times fainter than GRS 1915+105. The faintness of IGR J17091−3624 remains unexplained if high mass accretion rate is believed to give rise to extreme variability. We suggest that the low or retrograde spin of the IGR J17091−3624 can be a possible explanation for its faintness as compared to GRS 1915+105, which has very high spin of >0.98 (McClintock et al. 2006).

Another important timing property commonly seen in black hole binaries is the occurrence of quasi periodic oscillations (QPOs). These are generally observed as narrow peaks in power density spectrum superimposed on broad band continuum. Several authors have presented the correlation between QPO properties and spectral parameters, suggesting a link between generation of QPO and Comptonization component of spectrum. However, the mechanism of generation of QPO is not understood. In the present thesis, an attempt is made to understand the mechanism behind QPO modulations by studying an observation of GRS 1915+105 taken with NuSTAR. The source shows a QPO at ~ 1.5 Hz, which exhibits increasing power with energy. The spectrum is power law dominated and it is very well explained with a model consisting of a cutoff power law and its reflection (see Miller et al., 2013). Since power law is the only primary spectral component, it is expected that the QPO is generated as result of modulation of some of the spectral parameter(s). In order to test this hypothesis, attempts are made to explain energy dependence of QPO power by simulating light curves in different energy bands. Light curves are generated by varying spectral parameter at frequencies close to the QPO frequency and reading counts from the best-fit spectral model. The variation of four spectral parameters viz. spectral index, ionization parameter, normalization of cutoff power law and normalization of reflection is considered and it is found that the variation of spectral index reproduces the overall increasing trend of QPO power. the simulation of light curves is repeated by considering the variation of three spectral parameters together. Although variation of spectral index is found to be essential in order to explain the observed energy dependence, it is not sufficient to exactly reproduce the observed results. The simulation results are important as they put significant constraints on the models explaining the QPO mechanism.

6.2 Future Scope

Phase-resolved spectroscopy and simultaneous spectral fitting have contributed significantly in the work presented in this thesis. The method has been used to study 'heartbeat' patterns in the two sources GRS 1915+105 and IGR J17091−3624, and important results were obtained. The study can be easily extended to other variability classes of both the sources. This will not only help to understand spectral variation of a variability class, but also a comparison can be made among different variability classes. The phase-resolved spectroscopy for other variability classes of the two sources will further help to explore similarities and differences between them in more detail. As discussed in Chapter 4, simultaneous energy coverage from two instruments XMM-Newton and RXTE was of great importance to find constraints on the spectral parameters. However, it is generally difficult to find the simultaneous observations during a specific variability class from two instruments with energy coverage complementing each other. Therefore, we are looking forward to ASTROSAT data, which provides simultaneous energy coverage with different instruments onboard. This feature of ASTROSAT is quite promising to plan studies as discussed in Chapter 4, without having to wait for the availability of simultaneous observations from two different space missions.

The work on phase-resolved spectroscopy for the phases of QPO is described in Chapter 5. Given the order of frequencies (0.1-30 Hz) of observed low frequency QPOs, it is required to generate spectra for QPO phases that last typically few milli-seconds. Spectroscopy is generally limited by small number of counts at such a timescale. This, in fact is the reason why we restricted the binsize for NuSTAR light curves to 100 ms. However, ASTROSAT data will be of great help in this regard as it has a large area proportional counter (LAXPC), which is expected to provide better statistics at smaller timescales. In addition, LAXPC provides higher energy coverage (3-80 keV) as compared to PCA onboard RXTE. The simultaneous lower energy coverage (0.3-8 keV) by Soft X-ray imaging Telescope (SXT) is another great advantage as low energy coverage is very crucial to constrain the accretion disk component in spectra of black hole binaries.

Another important concept highlighted by the study is the link between faintness and the low spin of the black hole. This is again supported by the fact that many black hole binaries hosting a highly spinning black hole are generally brighter sources e.g GRS 1915+105, Cyg X-1 etc. This notion will be tested by finding spin estimates particularly for fainter black hole binaries.

The work on a QPO seen in the source GRS 1915+105 is discussed in Chapter 5 of the thesis, wherein an attempt is made to understand the modulation mechanism for QPOs by simulating light curves. The simulation procedure reads counts from the best-fit model to generate light curves and subsequently to study energy dependence of QPO power. Therefore, the work presents an additional criteria to test the validity of spectral model. Or in other words, a given model can be considered as the best explanation for the observed data if it fits spectrum, gives physically acceptable parameters and reproduces the energy dependence of QPO.

The simulation results strongly indicate towards variation of spectral index.

Two Component Accretion Flow (TCAF) model can provide an explanation of spectral index variation as it explains QPO in terms of oscillation of post shock region. Therefore, we plan to study energy dependence of the observed QPO by simulating light curves with counts taken from observed spectrum fitted with TCAF model. This will help in developing a better understanding of QPO mechanism.

Chapter 7

List of Publications

Publications in Journals

1. **Anjali Rao** & Santosh V. Vadawale, *Why is IGR J17091−3624 so faint? Constraints on distance, mass and spin from 'phase-resolved' spectroscopy of the heartbeat oscillations*, 2012, Astrophysical Journal Letters, **757**, L12 doi: 10.1088/2041-8205/757/1/L12.

2. **Anjali Rao Jassal** & Santosh V. Vadawale, *Variation of the inner disk radius during the onset of 2010 outburst of MAXI J1659−152*, 2015, Research in Astronomy and Astrophysics, **15**, 45-54
doi: 10.1088/1674-4527/15/1/005.

3. **Anjali Rao Jassal**, Santosh V. Vadawale, Mithun N. P. S and Ranjeev Misra, *Investigating the connection between quasi periodic oscillations and spectral components with NuSTAR data of GRS 1915+105*, 2015, accepted for publication in The Astrophysical Journal.

4. **Anjali Rao Jassal**, Santosh V. Vadawale, and Mithun N. P. S, *Phase resolved spectroscopy for the quasi periodic oscillation in GRS 1915+105 with NuSTAR data*, in preparation.

References

Abbey, T., Carpenter, J., Read, A., et al. 2006, in ESA Special Publication, Vol. 604, The X-ray Universe 2005, ed. A. Wilson, 943

Altamirano, D., & Belloni, T. 2012, *Astrophys. J. Lett.*, 747, L4

Altamirano, D., Wijnands, R., Belloni, T., & Motta, S. 2012, The Astronomer's Telegram, 3913, 1

Altamirano, D., Belloni, T., Linares, M., et al. 2011, *Astrophys. J. Lett.*, 742, L17

Axelsson, M., & Done, C. 2015, ArXiv e-prints

Bachetti, M., Harrison, F. A., Cook, R., et al. 2015, *Astrophys. J.*, 800, 109

Belloni, T., Klein-Wolt, M., Méndez, M., van der Klis, M., & van Paradijs, J. 2000, *Astron. Astrophys.*, 355, 271

Belloni, T. M. 2010, in Lecture Notes in Physics, Berlin Springer Verlag, Vol. 794, Lecture Notes in Physics, Berlin Springer Verlag, ed. T. Belloni, 53

Belloni, T. M., Motta, S. E., & Muñoz-Darias, T. 2011, Bulletin of the Astronomical Society of India, 39, 409

Belloni, T. M., Muñoz-Darias, T., & Kuulkers, E. 2010, The Astronomer's Telegram, 2926, 1

Böttcher, M., & Liang, E. P. 1998, *Astrophys. J.*, 506, 281

—. 1999, *Astrophys. J. Lett.*, 511, L37

Bradt, H. V., Rothschild, R. E., & Swank, J. H. 1993, *Astron. Astrophys. Suppl.*, 97, 355

Burrows, D. N., Hill, J. E., Nousek, J. A., et al. 2005, *Space Sci. Rev.*, 120, 165

Cabanac, C., Fender, R. P., Dunn, R. J. H., & Körding, E. G. 2009, *Mon. Not. Roy. Astron. Soc.*, 396, 1415

Cabanac, C., Henri, G., Petrucci, P.-O., et al. 2010, *Mon. Not. Roy. Astron. Soc.*, 404, 738

Capitanio, F., Del Santo, M., Bozzo, E., et al. 2012, *Mon. Not. Roy. Astron. Soc.*, 422, 3130

Capitanio, F., Bazzano, A., Ubertini, P., et al. 2006, *Astrophys. J.*, 643, 376

Capitanio, F., Giroletti, M., Molina, M., et al. 2009, *Astrophys. J.*, 690, 1621

Casella, P., Belloni, T., Homan, J., & Stella, L. 2004, *Astron. Astrophys.*, 426, 587

Castro-Tirado, A. J., Brandt, S., & Lund, N. 1992, *IAU Circ.*, 5590, 2

Chakrabarti, S., & Titarchuk, L. G. 1995, *Astrophys. J.*, 455, 623

Chakrabarti, S. K., Acharyya, K., & Molteni, D. 2004, *Astron. Astrophys.*, 421, 1

Debnath, D., Chakrabarti, S. K., & Mondal, S. 2014, *Mon. Not. Roy. Astron. Soc.*, 440, L121

Done, C., & Diaz Trigo, M. 2010, *Mon. Not. Roy. Astron. Soc.*, 407, 2287

Done, C., Wardziński, G., & Gierliński, M. 2004, *Mon. Not. Roy. Astron. Soc.*, 349, 393

Done, C., & Zycki, P. T. 1999, *Mon. Not. Roy. Astron. Soc.*, 305, 457

Duro, R., Dauser, T., Wilms, J., et al. 2011, *Astron. Astrophys.*, 533, L3

Esin, A. A., McClintock, J. E., & Narayan, R. 1997, *Astrophys. J.*, 489, 865

Fender, R., & Belloni, T. 2004, *Annual Review of Astronomy and Astrophysics*, 42, 317

Garain, S. K., Ghosh, H., & Chakrabarti, S. K. 2014, *Mon. Not. Roy. Astron. Soc.*, 437, 1329

Gehrels, N., Chincarini, G., Giommi, P., et al. 2004, *Astrophys. J.*, 611, 1005

Giacconi, R., & Rossi, B. 1960, *J. Geophys. Res.*, 65, 773

Gierliński, M., & Zdziarski, A. A. 2005, *Mon. Not. Roy. Astron. Soc.*, 363, 1349

Gierliński, M., Zdziarski, A. A., Poutanen, J., et al. 1999, *Mon. Not. Roy. Astron. Soc.*, 309, 496

Greiner, J., Cuby, J. G., McCaughrean, M. J., Castro-Tirado, A. J., & Mennickent, R. E. 2001, *Astron. Astrophys.*, 373, L37

Harrison, F. A., Craig, W. W., Christensen, F. E., et al. 2013, *Astrophys. J.*, 770, 103

Hiemstra, B., Méndez, M., Done, C., et al. 2011, *Mon. Not. Roy. Astron. Soc.*, 411, 137

Homan, J., & Belloni, T. 2005, *Astrophys. Space Sci.*, 300, 107

Hua, X.-M., Kazanas, D., & Titarchuk, L. 1997, *Astrophys. J. Lett.*, 482, L57

Ingram, A., & Done, C. 2010, *Mon. Not. Roy. Astron. Soc.*, 405, 2447

—. 2011, *Mon. Not. Roy. Astron. Soc.*, 415, 2323

—. 2012, *Mon. Not. Roy. Astron. Soc.*, 419, 2369

Ingram, A., & van der Klis, M. 2015, *Mon. Not. Roy. Astron. Soc.*, 446, 3516

Jahoda, K., Swank, J. H., Giles, A. B., et al. 1996, in Society of Photo-Optical Instrumentation Engineers (SPIE) Conference Series, Vol. 2808, EUV, X-Ray, and Gamma-Ray Instrumentation for Astronomy VII, ed. O. H. Siegmund & M. A. Gummin, 59–70

Jansen, F., Lumb, D., Altieri, B., et al. 2001, *Astron. Astrophys.*, 365, L1

Jassal, A. R., & Vadawale, S. V. 2015, Research in Astronomy and Astrophysics, 15, 45

Jonker, P. G., Miller-Jones, J. C. A., Homan, J., et al. 2012, *Mon. Not. Roy. Astron. Soc.*, 423, 3308

Kalamkar, M., Homan, J., Altamirano, D., et al. 2011, *Astrophys. J. Lett.*, 731, L2

Kaur, R., Kaper, L., Ellerbroek, L. E., et al. 2012, *Astrophys. J. Lett.*, 746, L23

Kennea, J. A., Romano, P., Mangano, V., et al. 2011, *Astrophys. J.*, 736, 22

King, A. L., Miller, J. M., Raymond, J., et al. 2012, *Astrophys. J. Lett.*, 746, L20

Krimm, H. A., Barthelmy, S. D., Baumgartner, W., et al. 2011, The Astronomer's Telegram, 3144, 1

Kuulkers, E., Lutovinov, A., Parmar, A., et al. 2003, The Astronomer's Telegram, 149, 1

Kuulkers, E., Kouveliotou, C., Belloni, T., et al. 2013, *Astron. Astrophys.*, 552, A32

Lasota, J.-P. 2001, *New Astronomy Reviews*, 45, 449

Levine, A. M., Bradt, H., Cui, W., et al. 1996, *Astrophys. J. Lett.*, 469, L33

Li, L.-X., Zimmerman, E. R., Narayan, R., & McClintock, J. E. 2005, *Astrophys. J. Supplement.*, 157, 335

Li, Z. B., Gao, H. Q., Zhang, Z., et al. 2014, *Mon. Not. Roy. Astron. Soc.*, 440, 143

Li, Z. B., Qu, J. L., Song, L. M., Ding, G. Q., & Zhang, C. M. 2013a, *Mon. Not. Roy. Astron. Soc.*, 428, 1704

Li, Z. B., Zhang, S., Qu, J. L., et al. 2013b, *Mon. Not. Roy. Astron. Soc.*, 433, 412

Lin, D., Remillard, R. A., & Homan, J. 2009, *Astrophys. J.*, 696, 1257

Liu, B. F., Mineshige, S., Meyer, F., Meyer-Hofmeister, E., & Kawaguchi, T. 2002, *Astrophys. J.*, 575, 117

Makishima, K., Maejima, Y., Mitsuda, K., et al. 1986, *Astrophys. J.*, 308, 635

Mangano, V., Hoversten, E. A., Markwardt, C. B., et al. 2010, GRB Coordinates Network, 11296, 1

Markwardt, C. B., Swank, J. H., & Taam, R. E. 1999, *Astrophys. J. Lett.*, 513, L37

Matsuoka, M., Kawasaki, K., Ueno, S., et al. 2009, *Pub. Astron. Soc. Japan*, 61, 999

McClintock, J. E., Remillard, R. A., Rupen, M. P., et al. 2009, *Astrophys. J.*, 698, 1398

McClintock, J. E., Shafee, R., Narayan, R., et al. 2006, *Astrophys. J.*, 652, 518

Meyer, F., Liu, B. F., & Meyer-Hofmeister, E. 2000, *Astron. Astrophys.*, 361, 175

Meyer-Hofmeister, E., & Meyer, F. 2003, *Astron. Astrophys.*, 402, 1013

Middleton, M., Done, C., Gierliński, M., & Davis, S. W. 2006, *Mon. Not. Roy. Astron. Soc.*, 373, 1004

Miller, J. M., & Homan, J. 2005, *Astrophys. J. Lett.*, 618, L107

Miller, J. M., Homan, J., Steeghs, D., et al. 2006, *Astrophys. J.*, 653, 525

Miller, J. M., Pooley, G. G., Fabian, A. C., et al. 2012, *Astrophys. J.*, 757, 11

Miller, J. M., Parker, M. L., Fuerst, F., et al. 2013, *Astrophys. J. Lett.*, 775, L45

Miller, J. M., Tomsick, J. A., Bachetti, M., et al. 2015, *Astrophys. J. Lett.*, 799, L6

Mirabel, I. F., & Rodríguez, L. F. 1994, *Nature*, 371, 46

Mitsuda, K., Inoue, H., Koyama, K., et al. 1984, *Pub. Astron. Soc. Japan*, 36, 741

Molteni, D., Sponholz, H., & Chakrabarti, S. K. 1996, *Astrophys. J.*, 457, 805

Morgan, E. H., Remillard, R. A., & Greiner, J. 1997, *Astrophys. J.*, 482, 993

Motta, S., Muñoz-Darias, T., Casella, P., Belloni, T., & Homan, J. 2011, *Mon. Not. Roy. Astron. Soc.*, 418, 2292

Muñoz-Darias, T., Motta, S., Pawar, D., et al. 2010, *Mon. Not. Roy. Astron. Soc.*, 404, L94

Muñoz-Darias, T., Motta, S., Stiele, H., & Belloni, T. M. 2011, *Mon. Not. Roy. Astron. Soc.*, 415, 292

Muno, M. P., Morgan, E. H., & Remillard, R. A. 1999, *Astrophys. J.*, 527, 321

Narayan, R., & Yi, I. 1994, *Astrophys. J. Lett.*, 428, L13

—. 1995, *Astrophys. J.*, 452, 710

Negoro, H., Yamaoka, K., Nakahira, S., et al. 2010, The Astronomer's Telegram, 2873, 1

Neilsen, J., Remillard, R. A., & Lee, J. C. 2011, *Astrophys. J.*, 737, 69

—. 2012, *Astrophys. J.*, 750, 71

Nishimura, J., Mitsuda, K., & Itoh, M. 1986, *Pub. Astron. Soc. Japan*, 38, 819

Nowak, M. A. 1994, *Astrophys. J.*, 422, 688

Nowak, M. A., & Wagoner, R. V. 1993, *Astrophys. J.*, 418, 187

Parker, M. L., Tomsick, J. A., Miller, J. M., et al. 2015, *Astrophys. J.*, 808, 9

Plant, D. S., Fender, R. P., Ponti, G., Muñoz-Darias, T., & Coriat, M. 2013, arXiv: 1309.4781

—. 2014, *Mon. Not. Roy. Astron. Soc.*, 442, 1767

—. 2015, *Astron. Astrophys.*, 573, A120

Plotkin, R. M., Gallo, E., Markoff, S., et al. 2015, *Mon. Not. Roy. Astron. Soc.*, 446, 4098

Poutanen, J., & Svensson, R. 1996, *Astrophys. J.*, 470, 249

Qiao, E., & Liu, B. F. 2009, *Pub. Astron. Soc. Japan*, 61, 403

Rao, A., & Vadawale, S. V. 2012, *Astrophys. J. Lett.*, 757, L12

Rao, A. R., Naik, S., Vadawale, S. V., & Chakrabarti, S. K. 2000, *Astron. Astrophys.*, 360, L25

Rebusco, P., Churazov, E., Sunyaev, R., Böhringer, H., & Forman, W. 2008, *Mon. Not. Roy. Astron. Soc.*, 384, 1511

Reid, M. J., McClintock, J. E., Steiner, J. F., et al. 2014, *Astrophys. J.*, 796, 2

Reis, R. C., Fabian, A. C., & Miller, J. M. 2010, *Mon. Not. Roy. Astron. Soc.*, 402, 836

Reis, R. C., Miller, J. M., King, A. L., & Reynolds, M. T. 2012a, The Astronomer's Telegram, 4382, 1

Reis, R. C., Miller, J. M., Reynolds, M. T., Fabian, A. C., & Walton, D. J. 2012b, *Astrophys. J.*, 751, 34

Remillard, R. A., & McClintock, J. E. 2006, *Annual Review of Astronomy and Astrophysics*, 44, 49

Remillard, R. A., McClintock, J. E., Orosz, J. A., & Levine, A. M. 2006, *Astrophys. J.*, 637, 1002

Remillard, R. A., Muno, M. P., McClintock, J. E., & Orosz, J. A. 2002, *Astrophys. J.*, 580, 1030

Revnivtsev, M., Gilfanov, M., Churazov, E., & Sunyaev, R. 2003, The Astronomer's Telegram, 150, 1

Reynolds, M. T., & Miller, J. M. 2013, *Astrophys. J.*, 769, 16

Reynolds, M. T., Miller, J. M., Homan, J., & Miniutti, G. 2010, *Astrophys. J.*, 709, 358

Rodriguez, J., Corbel, S., Caballero, I., et al. 2011, *Astron. Astrophys.*, 533, L4

Rodriguez, J., Corbel, S., Hannikainen, D. C., et al. 2004, *Astrophys. J.*, 615, 416

Rodriguez, J., Varnière, P., Tagger, M., & Durouchoux, P. 2002, *Astron. Astrophys.*, 387, 487

Rodriguez, J., Shaw, S. E., Hannikainen, D. C., et al. 2008, *Astrophys. J.*, 675, 1449

Romano, P., Campana, S., Chincarini, G., et al. 2006, *Astron. Astrophys.*, 456, 917

Rothschild, R. E., Blanco, P. R., Gruber, D. E., et al. 1998, *Astrophys. J.*, 496, 538

Rykoff, E. S., Miller, J. M., Steeghs, D., & Torres, M. A. P. 2007, *Astrophys. J.*, 666, 1129

Schnittman, J. D., Homan, J., & Miller, J. M. 2006a, *Astrophys. J.*, 642, 420

—. 2006b, *Astrophys. J.*, 642, 420

Shakura, N. I., & Sunyaev, R. A. 1973, *Astron. Astrophys.*, 24, 337

Shidatsu, M., Ueda, Y., Tazaki, F., et al. 2011, *Pub. Astron. Soc. Japan*, 63, 785

Singh, K. P., Tandon, S. N., Agrawal, P. C., et al. 2014, in Society of Photo-Optical Instrumentation Engineers (SPIE) Conference Series, Vol. 9144, Society of Photo-Optical Instrumentation Engineers (SPIE) Conference Series, 1

Sobczak, G. J., McClintock, J. E., Remillard, R. A., et al. 2000, *Astrophys. J.*, 531, 537

Sobolewska, M. A., & Życki, P. T. 2006, *Mon. Not. Roy. Astron. Soc.*, 370, 405

Stefanov, I. Z. 2014, *Mon. Not. Roy. Astron. Soc.*, 444, 2178

Steiner, J. F., McClintock, J. E., Remillard, R. A., Narayan, R., & Gou, L. 2009a, *Astrophys. J. Lett.*, 701, L83

Steiner, J. F., Narayan, R., McClintock, J. E., & Ebisawa, K. 2009b, *Pub. Astron. Soc. Pac.*, 121, 1279

Stella, L., & Vietri, M. 1998a, *Astrophys. J. Lett.*, 492, L59

—. 1998b, *Astrophys. J. Lett.*, 492, L59

Stiele, H., Belloni, T. M., Kalemci, E., & Motta, S. 2013, *Mon. Not. Roy. Astron. Soc.*, 429, 2655

Sunyaev, R. A., & Titarchuk, L. G. 1980, *Astron. Astrophys.*, 86, 121

Taam, R. E., & Lin, D. N. C. 1984, *Astrophys. J.*, 287, 761

Tagger, M., & Pellat, R. 1999, *Astron. Astrophys.*, 349, 1003

Titarchuk, L., & Osherovich, V. 2000, *Astrophys. J. Lett.*, 542, L111

Tomsick, J. A., & Kaaret, P. 2001, *Astrophys. J.*, 548, 401

Tomsick, J. A., Yamaoka, K., Corbel, S., et al. 2009, *Astrophys. J. Lett.*, 707, L87

Vadawale, S. V., Rao, A. R., Naik, S., et al. 2003, *Astrophys. J.*, 597, 1023

Vadawale, S. V., Rao, A. R., Nandi, A., & Chakrabarti, S. K. 2001, *Astron. Astrophys.*, 370, L17

van der Horst, A. J., Curran, P. A., Miller-Jones, J. C. A., et al. 2013, *Mon. Not. Roy. Astron. Soc.*

Varnière, P., Rodriguez, J., & Tagger, M. 2002, *Astron. Astrophys.*, 387, 497

Verner, D. A., Ferland, G. J., Korista, K. T., & Yakovlev, D. G. 1996, *Astrophys. J.*, 465, 487

Vignarca, F., Migliari, S., Belloni, T., Psaltis, D., & van der Klis, M. 2003, *Astron. Astrophys.*, 397, 729

Vincent, F. H., Meheut, H., Varniere, P., & Paumard, T. 2013, *Astron. Astrophys.*, 551, A54

Wagoner, R. V. 2012, *Astrophys. J. Lett.*, 752, L18

Wagoner, R. V., Silbergleit, A. S., & Ortega-Rodríguez, M. 2001a, *Astrophys. J. Lett.*, 559, L25

—. 2001b, *Astrophys. J. Lett.*, 559, L25

Wilms, J., Allen, A., & McCray, R. 2000, *Astrophys. J.*, 542, 914

Yamaoka, K., Allured, R., Kaaret, P., et al. 2012, *Pub. Astron. Soc. Japan*, 64, 32

Zdziarski, A. A. 2014, *Mon. Not. Roy. Astron. Soc.*, 444, 1113

Zdziarski, A. A., Gierliński, M., Mikołajewska, J., et al. 2004, *Mon. Not. Roy. Astron. Soc.*, 351, 791

Zdziarski, A. A., Gierliński, M., Rao, A. R., Vadawale, S. V., & Mikołajewska, J. 2005, *Mon. Not. Roy. Astron. Soc.*, 360, 825

Zdziarski, A. A., Johnson, W. N., & Magdziarz, P. 1996, *Mon. Not. Roy. Astron. Soc.*, 283, 193

Zhang, L., Chen, L., Qu, J.-l., & Bu, Q.-c. 2015, *Astron. J.*, 149, 82

Życki, P. T., Done, C., & Smith, D. A. 1999, *Mon. Not. Roy. Astron. Soc.*, 309, 561

The Astrophysical Journal Letters, 757:L12 (5pp), 2012 September 20 doi:10.1088/2041-8205/757/1/L12

WHY IS IGR J17091−3624 SO FAINT? CONSTRAINTS ON DISTANCE, MASS, AND SPIN FROM "PHASE-RESOLVED" SPECTROSCOPY OF THE "HEARTBEAT" OSCILLATIONS

Anjali Rao and S. V. Vadawale
Physical Research Laboratory, Ahmedabad-380009, India; anjali@prl.res.in
Received 2012 May 22; accepted 2012 August 10; published 2012 September 4

ABSTRACT

IGR J17091−3624 is a transient X-ray source and is believed to be a Galactic black hole candidate. Recently, it has received considerable attention due to the detection of peculiar variability patterns known as "heartbeats," which are quasi-periodic mini-outbursts repeated over timescales ranging between 5 and 70 s. So far, such variability patterns have been observed only in GRS 1915+105 and these are classified as ρ- and ν-variability classes. Here, we present the results of "phase-resolved" spectroscopy of the "heartbeat" oscillations of IGR J17091−3624 using data from simultaneous observations made by *RXTE* and *XMM-Newton*. We find that the 0.7–35 keV spectra can be fitted with a "canonical" model for black hole sources consisting of only two components—a multi-temperature disk blackbody and a power law (or its equivalent). We attempt to constrain the system parameters of the source by simultaneously fitting spectra during different phases of the burst profile while tying the system parameters across the phases. The results indicate that the source is a high inclination binary ($i > 53°$). Further, the observed low flux from the source can be explained only if the black hole spin is very low, along with constraints on the black hole mass ($<5\ M_{\odot}$) and distance (>20 kpc). For higher inclination angles, which is favored by the data, the black hole spin is required to be negative. Thus, low or retrograde spin could be the reason for the low luminosity of the source.

Key words: accretion, accretion disks – black hole physics – X-rays: binaries – X-rays: individual (IGR J17091-3624)

1. INTRODUCTION

The micro-quasar GRS 1915+105 is an enigmatic black hole binary (BHB) exhibiting enormous variability which has been classified into more than 14 different variability classes (Belloni et al. 2000; Fender & Belloni 2004). It is believed that the extreme variability and rapid state changes observed in GRS 1915+105 are due to a very high accretion rate, which is close to, or at times higher than, the Eddington accretion rate (Done et al. 2004). It is also known for exhibiting large superluminal radio flares and steady radio emission which are always associated with specific X-ray variability classes (Mirabel et al. 1998; Fender et al. 1999; Vadawale et al. 2003). Such an extreme and correlated multi-wavelength variability makes GRS 1915+105 a unique BHB. In this context, IGR J17091−3624, a new X-ray transient source believed to be a BHB, generated considerable interest recently. It was detected by *INTEGRAL*/IBIS in 2003 (Kuulkers et al. 2003). It has exhibited repeated outbursts with periods of two to four years in 1994, 1996, 2001, 2003, 2007, and 2011 (Revnivtsev et al. 2003; Kuulkers et al. 2003; Capitanio et al. 2006, 2009; Krimm et al. 2011; Krimm & Kennea 2011). The recent 2011 outburst of IGR J17091−3624 was unusually long and the source was found to be active even after one year (Altamirano et al. 2012). During this outburst, IGR J17091−3624 revealed its highly variable nature and showed variability patterns so far observed only in GRS 1915+105. The most prominent of these patterns was the "heartbeat" pattern, similar to the ρ-class in GRS 1915+105. Altamirano et al. (2011) documented the first six months of *RXTE* observations and showed that not only ρ-class but many other variability patterns similar to ν-, α-, λ-, β-, μ-, and χ- classes have been observed during this outburst of IGR J17091−3624. Altamirano & Belloni (2012) also detected a high-frequency quasi-periodic oscillation (HFQPO) in this source with a frequency of 66 Hz, which is almost identical to the frequency of HFQPO in GRS 1915+105. Despite striking morphological similarities, the most perplexing difference between the two sources lies in their observed intensities. While GRS 1915+105 is one of the brightest X-ray sources with a typical brightness of ~0.5–2 Crab, IGR J17091−3624 is about 20 times fainter. In the present scenario, mass, distance, and inclination for this source are rather poorly constrained, with reports so far suggesting a mass range of $<3\ M_{\odot}$ (Altamirano et al. 2011) to $\sim 15\ M_{\odot}$ (Altamirano & Belloni 2012) and a distance range of ~11 kpc (Rodriguez et al. 2011) to ~20 kpc (Pahari et al. 2011). Nevertheless, the apparent faintness of IGR J17091−3624 is difficult to explain even after assuming the smallest possible mass of 3 $M_{\odot}$ for a black hole (Fryer & Kalogera 2001) and the largest possible distance of ~25 kpc for a Galactic source. Here, we attempt to investigate the possible reasons for this apparent faintness of IGR J17091−3624 by simultaneously fitting spectra at different phases. The main idea is that the system parameters cannot change over the phase of the oscillations. Therefore, a simultaneous fitting of spectra at different phases, with system parameters tied across phases, may put a better constraint on them. This, along with a proposal that the "heartbeats" can be used as a "standard candle," leads to a primary conclusion that the faintness of IGR J17091−3624 is due to its low or negative spin.

2. OBSERVATIONS AND DATA ANALYSIS

We have used data from long simultaneous observations of IGR J17091−3624 made on 2011 March 27 with *RXTE* (ObsID: 96420-01-05-000, total exposure ~21 ks) and *XMM-Newton* (ObsID: 0677980201, total exposure ~39 ks) with net simultaneous exposure of ~15 ks. The data reduction for the *RXTE*/PCA observation was carried out with HEASoft version 6.8 following standard analysis procedure for

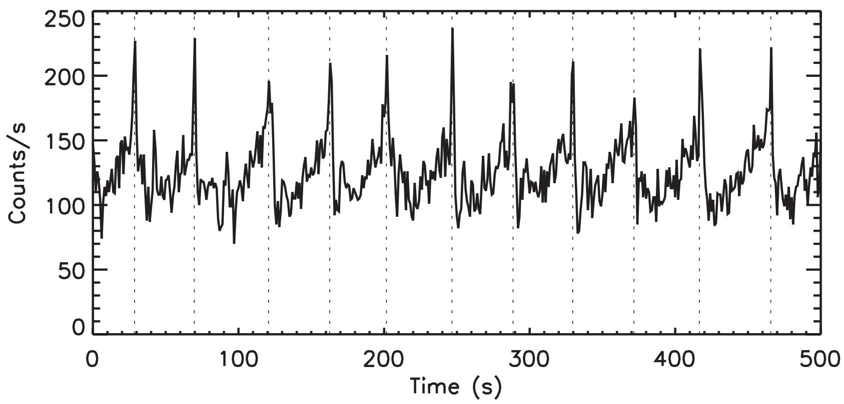

Figure 1. *RXTE*/PCA light curve of IGR J17091−3624 from observation 96420-01-05-000. The light curve was extracted with a bin size of 1 s from PCU2 covering an energy range of 2.0–60.0 keV. The vertical lines show the identified peak times of bursts.

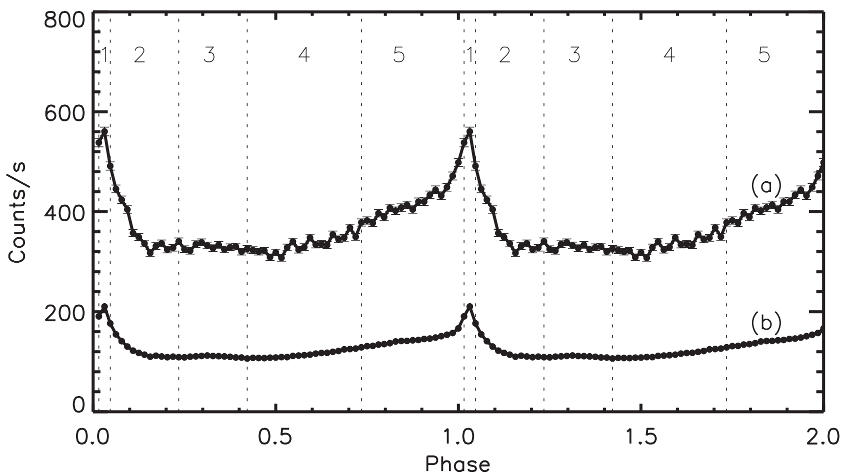

Figure 2. Phase-folded light curves from *XMM-Newton* and *RXTE*, labeled (a) and (b), respectively. Dotted vertical lines show demarcations for the five phases used for the simultaneous spectral fitting.

Good Xenon data. We extracted 1 s light curve from PCU2 data. It showed the typical ν-class oscillations with periods ranging from 30 to 50 s (Figure 1). It contained a total of 385 bursts. We carried out "phase-resolved" spectroscopy for these bursts in the energy range of 3.0–35.0 keV for *RXTE*/PCA and 0.7–12.0 keV for *XMM*/PN data as described below. The peak time for each burst was identified in a semiautomatic manner using an IDL script and the peak-to-peak interval between consecutive bursts was divided into 64 phases of equal length. The start and stop times of each phase, recorded in *RXTE* mission time for 385 bursts, were used to extract spectra for each phase. Total counts for all 64 spectra and their corresponding exposure times were then used to generate the "phase-folded" light curve (Figure 2). The 64 phase bins were grouped into five phases as shown in Figure 2 and the spectra extracted for these five phases were used for simultaneous spectral fitting. The grouping was carried out mainly by the visual inspection of the folded *RXTE*/PCA light curve. The *XMM* observation was carried out in the *fast timing* mode of EPIC-MOS and the *burst* mode of EPIC-PN, and we followed the standard analysis procedures for these modes using *SAS v11.0.0* and the latest calibration files. We used data from *XMM*-PN only because MOS2 data could not be checked for possible pileup (generation of pattern plot always resulted in error) whereas MOS1 data are not useful in timing mode because of a dead pixel in the CCD. For PN data, the observed and the expected pattern behavior differed below 0.7 keV and hence the energy range for rest of the analysis was restricted to 0.7–12.0 keV. Start and stop times of the 64 phases of all bursts from *RXTE* mission were converted into *XMM* mission time using the *xTime* tool, available at HEASARC, which were used to build gti files using SAS task *gtibuild*. These gti files were used for extracting the 64 phase spectra using the task *evselect*. The "phase-folded" light curve was generated using the total counts and the exposure times, as described earlier. The subtle features were averaged out as a consequence of the quasi-periodicity and co-adding, but the overall profile of the "phase-folded" light curve followed a typical burst cycle. Further, it was seen that the oscillations were more pronounced in the *XMM* light curve, indicating that the accretion disk radiation was primarily participating in the oscillations and not the Comptonized emission from the corona which dominates at higher energies. Source spectra from the five grouped phases were extracted using RAWX columns between 32 and 42 for single and double pixel events (pattern $\leqslant 4$). SAS tools *rmfgen* and *arfgen* were used to generate redistribution matrices and ancillary files, respectively, and the same files were used for the spectra of all phases. The background spectrum was extracted from RAWX columns between 5 and 7 after confirming that the region was not contaminated significantly with source photons in the selected energy range. A single background spectrum was used for the five phases. All spectra were rebinned using sastask *specgroup* to have a minimum of 25 counts per channel.

2.1. Simultaneous Spectral Fitting

Once we extracted the spectra for the five phases for both Proportional Counter Array (PCA) and PN, the 10 spectra were fitted simultaneously with various parameters tied as follows. The 10 spectra were loaded into XSPEC as 10 data groups. For a given phase, all parameters for PCA and PN spectra were tied together except for the normalization constant which was frozen at 1.0 for PN whereas for PCA it was kept free but tied across the five phases. For a particular spectral model, we tied all parameters representing system property, such as mass, distance, inclination, spin or combination of these, across the five phases. The parameters describing the accretion process such as the inner disk temperature or accretion rate, inner disk radius, etc., were fitted independently for each phase.

3. RESULTS AND DISCUSSION

Wide-band X-ray spectrum of a BHB generally consists of two dominant components: a multi-color disk and a high-energy tail arising from Compton scattering in an optically thin region surrounding the disk. We used DISKPN (Gierliński et al. 1999) as a simplified disk model, primarily because its parameters are cleanly separated in accretion-process-dependent parameters (disk temperature and inner disk radius) and system parameters (normalization). For a general relativistic description of the multi-temperature disk spectrum, we used KERRBB (Li et al. 2005), which is widely used for its accurate modeling of disk spectrum and to investigate black hole spin. The high-energy tail of the spectrum is typically modeled as POWERLAW to approximate the Comptonized component. However, Steiner et al. (2009b) proposed a more physical model SIMPL to empirically describe the Comptonized component. Here, we have used SIMPL along with one of the two disk models (DISKPN and KERRBB) to fit the spectra in the five phases simultaneously, as described below.

3.1. Model: DISKPN

For the first part of the analysis, we fitted *RXTE*-PCA and *XMM*-PN spectra for the five phases simultaneously with CONST*PHABS*(SIMPL⊗DISKPN). The parameter CONST was used to account for possible calibration uncertainties between the two instruments. Normalizations of DISKPN were tied across the five phases, whereas rest of the parameters were allowed to vary independently. Though the interstellar absorption can be considered a part of the system parameters, we allowed it to vary to account for any phase-dependent absorption intrinsic to the source. We, however, found that the $N_{\rm H}$ values for the five phases were not significantly different and the fitted values of $N_{\rm H}$ were in agreement with the values reported by Rodriguez et al. (2011) and Krimm et al. (2011). Table 1 provides the results of spectral fits. It can be seen that the inner disk temperature is highest for phase 1 corresponding to the peak of the bursts, implying higher accretion rate as expected. We verified that neither the Fe line nor the reflection component was required to fit the data. A best fit was obtained with the χ^2 value of 1709.0 for 1030 degrees of freedom. However, for the present work, the best-fit value of the DISKPN normalization, $N_{\rm DPN} = M^2 \cos(i)/D^2 f_{\rm col}^4$, more importantly, is that it can provide some constraints on mass (M), distance (D), and inclination (i). The best-fit value of the DISKPN normalization was found to be $N_{\rm DPN} = 4.0 \times 10^{-4}$. Assuming a minimum mass of $\sim 3\ M_\odot$ and a maximum distance of $\sim$25 kpc for a Galactic black hole candidate along with a standard value for color correction factor, $f_{\rm col} = 1.7$, the best-fit value of $N_{\rm DPN}$ resulted in a lower limit on the inclination angle of 76°. Considering the 90% upper confidence limit of 1.04×10^{-3} for the normalization, the lowest possible inclination angle was $\sim$53°. This lower limit comes only from simultaneous spectral fitting and it is not dependent on any additional information, and hence it can be considered to be fairly robust. Since spectral fitting could not constrain the lower limit of $N_{\rm DPN}$, it was not possible to obtain an upper limit on i with the spectral fitting. However, simultaneous spectral analysis with DISKPN to model accretion disk spectra suggests that IGR J17091−3624 is a high inclination binary. This is consistent with the finding of Capitanio et al. (2012) and King et al. (2012).

Table 1
Parameters Obtained from a Simultaneous Fit to the Spectra of Five Phases with Model CONS*PHABS*(SIMPL⊗DISKPN)

	Phase 1	Phase 2	Phase 3	Phase 4	Phase 5
$N_{\rm H}$ ($\times 10^{22}$ cm^{-2})	$0.93^{+0.03}_{-0.03}$	$0.84^{+0.02}_{-0.02}$	$0.81^{+0.01}_{-0.02}$	$0.81^{+0.01}_{-0.01}$	$0.88^{+0.01}_{-0.01}$
$T_{\rm max}$ (keV)	$1.24^{+0.05}_{-0.05}$	$1.11^{+0.01}_{-0.01}$	$1.02^{+0.01}_{-0.01}$	$1.05^{+0.01}_{-0.01}$	$1.11^{+0.01}_{-0.01}$
$R_{\rm in}$ (R_g)	$24.8^{+2.9}_{-2.4}$	$24.9^{+1.2}_{-1.1}$	$28.2^{+1.3}_{-1.2}$	$26.3^{+1.0}_{-0.9}$	$27.3^{+1.0}_{-1.0}$
Γ	$3.57^{+0.25}_{-0.28}$	$2.66^{+0.10}_{-0.10}$	$2.56^{+0.06}_{-0.06}$	$2.52^{+0.04}_{-0.04}$	$2.70^{+0.06}_{-0.06}$
Scattered fraction	$0.47^{+0.02}_{-0.28}$	$0.27^{+0.02}_{-0.02}$	$0.36^{+0.02}_{-0.02}$	$0.37^{+0.01}_{-0.01}$	$0.35^{+0.02}_{-0.02}$
Disk flux[a]	2.10	1.23	1.01	1.06	1.47
Total flux[a]	2.54	1.53	1.42	1.49	1.92
DISKPN norm[b]			$4.0^{+6.4}_{-3.7} \times 10^{-4}$		

Notes.
[a] Unabsorbed flux in units of $\times 10^{-9}$ erg s^{-1} cm^{-2} for 2–10 keV energy range. Unabsorbed bolometric disk flux for phase 1 is 4.10×10^{-9} erg s^{-1} cm^{-2}. (See the text for discussion).
[b] Since spectral fitting could not constrain the lower limit of norm, it was calculated from the extreme values of M, D, and i.

3.2. Model: KERRBB

In the second part, we fitted the spectra using the model CONS*PHABS*(SIMPL⊗KERRBB). Apart from mass, distance, inclination, and spin as independent fit parameters, KERRBB has parameters governing the second-order effects such as "spectral hardening factor," "returning radiation," and "limb darkening." We, however, froze these parameters to their default values. Typically, KERRBB is used for disk-dominated spectra with luminosity $<0.3\ L_{\rm Edd}$; however, Steiner et al. (2009a) have shown that SIMPL⊗KERRBB can be used to accurately describe spectra with higher luminosities as well. In this case, we tied all KERRBB parameters except $N_{\rm H}$ and mass accretion rate across the five phases. Further, the normalization was frozen to 1.0. Since all system parameters cannot be fitted simultaneously, we selected specific values for mass, inclination, and spin and fitted for mass accretion rate and distance. In order to systematically investigate the parameter space, we varied the black hole mass from 3 $M_\odot$ to 20 $M_\odot$, the inclination angle from 50° to 85°, and the spin from 0 to 0.9. The results of this analysis are shown in Figures 3 and 4. Figure 3 shows variation of interstellar absorption, $N_{\rm H}$, two parameters of SIMPL—power-law index, Γ and the scattering fraction, $f_{\rm sc}$, and fit statistic, χ^2_ν for the five phases. Since these parameters are more or less the same for any combination of system parameters (mass, distance, inclination, and spin), these are shown without any distinction. Again it was found that neither the Fe line nor the reflection component is required for fitting the data, with the F-test chance improvement probability being >88% for all combinations of mass, distance, and inclination. For a combination of mass M, inclination i

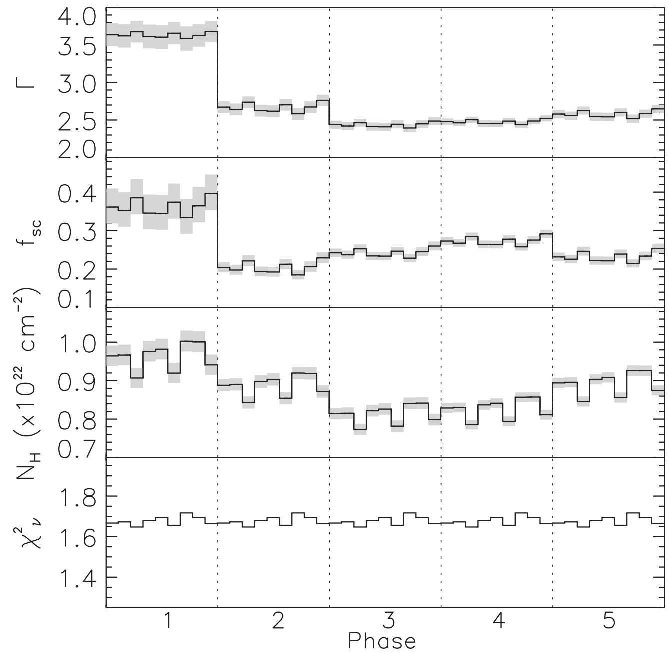

Figure 3. Best-fit values for all five phases of Γ, scattering fraction (f_{sc}), N_H, and χ^2_ν for all combinations of D, $\dot{M}$, i, and a_*. The parameters are more or less similar for any combination of system parameters and hence distinction between them is not made. Error bars (90% confidence) are shown with gray and only a subset of data are shown here.

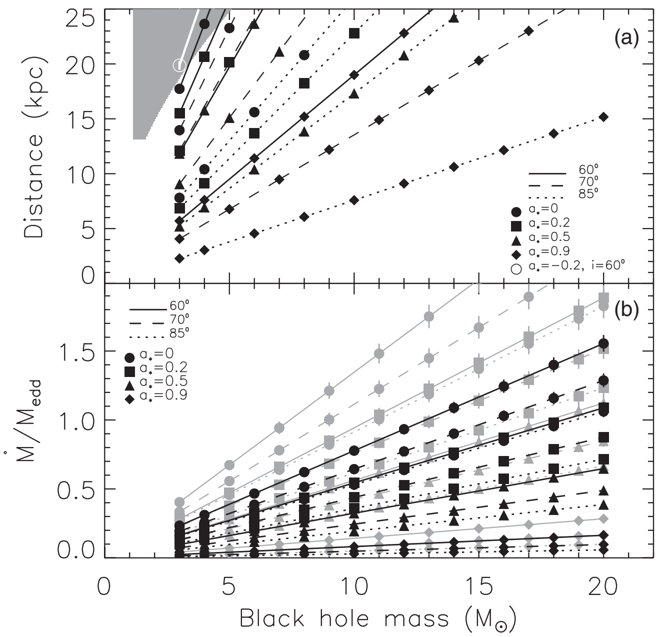

Figure 4. Variation of distance (panel (a)) and mass accretion rate (panel (b)) as a function of mass for different inclination angles and spins, as shown in the legend. For the purpose of clarity, symbols are shown for alternate values of mass, and mass accretion rate is shown only for the maximum (gray) and the minimum (black) of the five values. The gray region in the top left corner of panel (a) shows the allowed range for the black hole mass and distance from the luminosity argument.

(>50°), and spin a_*, the fitted values of distance D (top panel) and mass accretion rate $\dot{M}_{\rm Edd}$ (bottom panel) have been shown in Figure 4. Only the maximum (phase 1) and minimum (phase 3) mass accretion rates have been shown in Figure 4 for the sake of clarity. Error bars (90% confidence limit) are smaller than the symbols for most of the points in plot. This indicates that the distance and the accretion rate are very well constrained for a given combination of system parameters.

Figure 4 can be used to put some significant limits on the spin of the black hole with some independent constraints on either black hole mass or distance. One such independent constraint comes from the total luminosity argument during "heartbeat" oscillations. Neilsen et al. (2011, 2012) studied such oscillations in GRS 1915+105 and suggested the radiation pressure instability augmented by the local Eddington limit within the inner accretion disk to be the origin of such a variability pattern. However, this mechanism requires high accretion rate. Neilsen et al. (2011) showed that during the peak of the "heartbeat," the bolometric disk luminosity is typically as high as 80%–90% of the Eddington luminosity. Given the similarity between the variability patterns in GRS 1915+105 and IGR J17091−3624, it is natural to assume a similar mechanism operating in both sources. In this way, the observed flux during the peak of the "heartbeat" oscillations can be used to estimate the distance for a given mass, or, in other words, "heartbeat" can be used as a standard candle to constrain the parameters.

We found the best-fit value of the peak bolometric flux to be 4.10 $\times 10^{-9}$ erg s^{-1} cm^{-2}. Figure 1 shows that the peak flux in individual bursts is not the same and there is a burst-to-burst variation in the peak flux values. Therefore, we have assumed the range of the peak flux to be (3.0–5.0) $\times 10^{-9}$ erg s^{-1} cm^{-2} and a more conservative range of peak luminosity to be 60%–90% of Eddington luminosity. The obtained possible M–D range is shown as a gray area in the top left corner of Figure 4. It can be seen that the points within this region correspond to inclination angle <60° and spin <0.2. However, the lower limit on inclination was found to be ∼76° from DISKPN normalization. This presents the tantalizing possibility of the black hole spin being retrograde, indicating a black hole spin in opposite direction to the accretion disk. Further, we have found a lower limit of ∼53° on the inclination angle from the 90% upper confidence limit of DISKPN normalization. The points corresponding to $i \geqslant 50°$ require the spin to be <0.2. Thus, we exclude the possibility of high spin and it appears that the main reason for the observed faintness of IGR J17091−3624 is very low (or even negative) spin of the black hole, in contrast to GRS 1915+105, which is known to have a very high spin (McClintock et al. 2006).

It can be seen that even for the exotic type of black hole with mass <3 $M_\odot$ (Altamirano et al. 2011), this inference on black hole spin remains valid. Further, in order to verify the effect of the other frozen parameters of KERRBB, such as returning radiation, limb darkening, and inner boundary stress, we have also enabled all of them (one by one as well as all together) and found that the lines corresponding to a particular combination of spin and inclination angle move away from the shaded region. We verified that the same is valid when POWERLAW is used instead of SIMPL. Thus for any combination of these parameters or model for the high-energy tail, the black hole spin is required to be either very low or negative.

The 66 Hz HFQPO of IGR J17091−3624 detected by Altamirano & Belloni (2012) may also be considered to be an independent constraint on black hole mass, if it is assumed to be related to mass. In this case, the black hole mass in IGR J17091−3624 has to be ∼15 $M_\odot$. For such a high black hole mass, Figure 4(a) does not provide any constraint on the distance; however, both the inclination angle and the spin are required to be >70° and >0.7, respectively. For these high values of inclination angle and spin, Figure 4(b) shows that the required accretion rate is only a small fraction of the Eddington accretion rate. Thus, if we assume that the 66 Hz QPO is related to the black hole mass, the basic accretion process giving rise to the apparent similar variability of GRS 1915+105 and IGR J17091−3624 has to be different. However, it is more likely, as also suggested by Altamirano & Belloni (2012), that the 66 Hz HFQPO is not directly related to the black hole mass. In that case, the previous argument for low black hole mass based on the apparent flux and similar accretion process between IGR J17091−3624 and GRS 1915+105 holds, and the inference of low or negative spin remains valid. Overall, this work indicates that the black hole spin may not play a significant role in generating the observed extreme variability and such a behavior is generated mainly by a high accretion rate.

4. CONCLUSIONS

GRS 1915+105 is so far the only BHB exhibiting extreme variability and spectral changes over timescales as short as a few tens of seconds. Observations of similar variability in another BHB, IGR J17091−3624, establish that such extreme variability of GRS 1915+105 is not due to some specific coincidences unique to one particular BHB, but is a more generic phenomenon. Here, we presented results of simultaneous fitting of 0.7–35.0 keV spectra during different phases of the "heartbeat" oscillations in IGR J17091−3624, which indicate that the most likely difference between GRS 1915+105 and IGR J17091−3624 is in the spins of the respective black holes. While the black hole in GRS 1915+105 is known to be rotating with high spin, the black hole in IGR J17091−3624 is found to have a very low spin. In fact, for inclination $\sim 70^{\circ}$, which is favored by the data, the black hole could very well have a retrograde spin. In this case, IGR J17091−3624 would be the first known astrophysical source having a retrograde spin. Even though theoretically possible, such a scenario would be very challenging to explain from the point of view of evolution of such a system.

This research has made use of data obtained from High Energy Astrophysics Science Archive Research Center (HEASARC), provided by NASA's Goddard Space Flight Center. We thank A. R. Rao for useful discussions. We also thank the anonymous referee for very useful comments.

REFERENCES

Altamirano, D., & Belloni, T. 2012, ApJ, 747, L4
Altamirano, D., Belloni, T., Linares, M., et al. 2011, ApJ, 742, L17
Altamirano, D., Wijnands, R., Belloni, T., & Motta, S. 2012, ATel, 3913, 1
Belloni, T., Klein-Wolt, M., Méndez, M., van der Klis, M., & van Paradijs, J. 2000, A&A, 355, 271
Capitanio, F., Bazzano, A., Ubertini, P., et al. 2006, ApJ, 643, 376
Capitanio, F., Del Santo, M., Bozzo, E., et al. 2012, MNRAS, 422, 3130
Capitanio, F., Giroletti, M., Molina, M., et al. 2009, ApJ, 690, 1621
Done, C., Wardziński, G., & Gierliński, M. 2004, MNRAS, 349, 393
Fender, R., & Belloni, T. 2004, ARA&A, 42, 317
Fender, R. P., Garrington, S. T., McKay, D. J., et al. 1999, MNRAS, 304, 865
Fryer, C. L., & Kalogera, V. 2001, ApJ, 554, 548
Gierliński, M., Zdziarski, A. A., Poutanen, J., et al. 1999, MNRAS, 309, 496
King, A. L., Miller, J. M., Raymond, J., et al. 2012, ApJ, 746, L20
Krimm, H. A., Barthelmy, S. D., Baumgartner, W., et al. 2011, ATel, 3144, 1
Krimm, H. A., & Kennea, J. A. 2011, ATel, 3148, 1
Kuulkers, E., Lutovinov, A., Parmar, A., et al. 2003, ATel, 149, 1
Li, L.-X., Zimmerman, E. R., Narayan, R., & McClintock, J. E. 2005, ApJS, 157, 335
McClintock, J. E., Shafee, R., Narayan, R., et al. 2006, ApJ, 652, 518
Mirabel, I. F., Dhawan, V., Chaty, S., et al. 1998, A&A, 330, L9
Neilsen, J., Remillard, R. A., & Lee, J. C. 2011, ApJ, 737, 69
Neilsen, J., Remillard, R. A., & Lee, J. C. 2012, ApJ, 750, 71
Pahari, M., Yadav, J., & Bhattacharyya, S. 2011, arXiv:1105.4694
Revnivtsev, M., Gilfanov, M., Churazov, E., & Sunyaev, R. 2003, ATel, 150, 1
Rodriguez, J., Corbel, S., Caballero, I., et al. 2011, A&A, 533, L4
Steiner, J. F., McClintock, J. E., Remillard, R. A., Narayan, R., & Gou, L. 2009a, ApJ, 701, L83
Steiner, J. F., Narayan, R., McClintock, J. E., & Ebisawa, K. 2009b, PASP, 121, 1279
Vadawale, S. V., Rao, A. R., Naik, S., et al. 2003, ApJ, 597, 1023

RAA 2015 Vol. **15** No. **1**, 45–54 doi: 10.1088/1674–4527/15/1/005
http://www.raa-journal.org *http://www.iop.org/journals/raa*

***R**esearch in*
***A**stronomy and*
***A**strophysics*

Variation of the inner disk radius during the onset of the 2010 outburst of MAXI J1659–152

Anjali Rao Jassal and Santosh V. Vadawale

Physical Research Laboratory, Navrangpura, Ahmedabad 380009, India; *anjali@prl.res.in*

Received 2013 December 4; accepted 2014 May 15

Abstract Low mass black hole binaries are generally transient sources and spend most of their time in the quiescent state. It is believed that the inner accretion flow in the quiescent state is in the form of advection dominated accretion flow and the cold outer accretion disk is truncated far away from the central black hole. During the onset of an outburst, the disk gradually extends towards the central black hole. However, the observational evidence for this general picture is indirect at best. Here we present the results of a study performed to understand the variation of the inner disk radius during the early phase of an outburst. We investigated the variation of the inner disk radius during the 2010 outburst of the black hole candidate MAXI J1659-152 using the method of simultaneous spectral fitting. We found that the inner edge of the disk is truncated at a large radius in the beginning of the outburst when the source was in the hard state. We found a systematic decrease in the inner disk radius as the outburst progressed. We also estimated an upper limit on the mass of the black hole to be $8.1 \pm 2.9\ M_{\odot}$ within the uncertainty of the distance and inclination angle.

Key words: accretion, accretion disks — black hole physics — X-rays: binaries — X-rays: individual (MAXI J1659–152)

1 INTRODUCTION

There are about 70 known black hole sources and candidates, and most of them are transient in nature. They occasionally switch to the outburst state and remain most of the time in the quiescent state. The transient nature of black hole binaries can be broadly explained by the hydrogen ionization instability taking place mainly in the cooler outer regions of the accretion disks (see Lasota 2001). Detailed study of these outbursts is important in order to understand the various processes in the vicinity of the black hole. High quality data available from recent missions have provided valuable insights in the overall understanding of outbursts from black hole binaries. However, there are still some key aspects, particularly regarding the nature of the inner accretion disk during the state transitions, which are far from being fully understood. In general, black hole binaries have shown different outburst profiles and durations. The recurrence time between the successive outbursts is also found to differ among transient black hole binaries with multiple outbursts. Despite all these differences, almost all black holes have been observed to follow a Q-shaped track in the hardness-intensity diagram (see Homan et al. 2001; Belloni 2004; Fender et al. 2009). Such diagrams for many black holes show that an outburst starts with the source in the hard state and as the outburst progresses, the source switches to the soft state via an intermediate state called HIMS (see Fender et al. 2009; Done et al. 2007). The source again reaches the hard state when it enters into the quiescence via another intermediate state generally known as SIMS.

Observed properties of the hard and the soft states can be broadly explained in terms of the accretion disk having different inner radii during the two states. According to the truncation model for accretion disk around black hole binaries, the inner disk extends close to the innermost stable circular orbit (ISCO) during the soft states. Thus observations of the soft state provide a good opportunity to measure the spin of the black hole. However, the inner disk radius is truncated at a larger Schwarzschild radius when the source is in the hard state (see Qiao & Liu 2009). Since an outburst starts with the source in the hard state, it is presumed that in the quiescent state too the disk is truncated with the inner accretion flow in the form of a radiatively inefficient advection dominated accretion flow (Narayan & Yi 1994). Thus it is expected that during the onset of the outburst itself, the disk gradually moves in. The observational evidence, showing the changes in the inner disk radii during the very early stages of the outburst, is the best way to verify this concept. Such observations of very early stages are difficult because the outburst can typically only be detected after its luminosity reaches a significant fraction of the peak luminosity. However, with the recent availability of sensitive all sky monitors, it is possible to detect the sources at early stages of the outburst. Even after the early detection of an outburst, rapid follow-up observations, particularly with focusing X-ray telescopes that have energy coverage below 1 keV, are necessary to investigate the accretion behavior during the early progress of the outburst. NASA's *Swift* GRB mission (Gehrels et al. 2004), with its rapid follow-up capability using the X-ray telescope (XRT), is also providing valuable observations for the early stages of X-ray binary outbursts. MAXI J1659–152 is one such black hole binary source which was extensively followed up by *Swift* after the early detection of its 2010 outburst by the MAXI experiment onboard the International Space Station (Matsuoka et al. 2009). In the present work, we have focused on the investigation of the inner disk radius using dense and low-energy coverage by *Swift*/XRT.

MAXI J1659−152 was detected both by *Swift*/BAT (Mangano et al. 2010) and MAXI (Negoro et al. 2010) when it entered its discovery outburst on 2010 September 25. The source remained in the outburst state for about one and a half months. Various properties of this source during the outburst have been extensively reported by Muñoz-Darias et al. (2011), Kennea et al. (2011), Kalamkar et al. (2011) and Yamaoka et al. (2012) using the observations with both *Swift* and *RXTE* missions. Muñoz-Darias et al. (2011) carried out a spectral and timing analysis using energy and power density spectra obtained from *RXTE*/PCA. They found the inner disk radius to be constant at about 40 km during the peak of the outburst with a possible decrease towards the later stages of the outburst, assuming an orbital inclination of 70°. Kennea et al. (2011) studied *Swift* observations of the source and found that the inner radius of the disk was decreasing as the outburst proceeded. Kennea et al. (2011) also suggested the inclination of the source to be in the range 60°–75° owing to the absence of eclipses and the presence of dips in the light curves.

Here we report our reanalysis of *Swift* observations of MAXI J1659–152 carried out using the method of simultaneous fitting of multiple observations while tying the geometry dependent parameters (such as black hole mass, binary inclination, distance, etc.) which are not expected to change across various observations (Rao & Vadawale 2012). This method is expected to provide a better estimate of the process dependent parameters such as disk radius, temperature and accretion rate because the uncertainty in the geometry dependent parameters is removed to a large extent. We find that the source was in the hard state during initial observations and the accretion disk was truncated at a large radius. We show that the inner disk radius systematically decreases as the outburst progresses and the spectrum becomes softer and ultimately it reaches the ISCO during the peak of the outburst. This is possibly the first observational confirmation of the general picture of black hole binary outburst evolution that demonstrates it starts in the hard state with a truncated accretion disk and then the disk radius gradually decreases to the ISCO.

Section 2 of this paper provides the details of the observations used and the data reduction steps followed in the present study. We have described details of the analysis and the results obtained from it in Section 3 which is followed by the discussion in Section 4.

2 OBSERVATIONS AND DATA REDUCTION

The 2010 outburst of MAXI J1659–152 was extensively recorded by *Swift*. A total of 39 observations with *Swift*/XRT are available from NASA's public archive HEASARC. All XRT observations are in windowed timing mode except an observation taken on MJD 55466 (ObsID 00434928004) which is in photon counting mode. For the present work we have analyzed data from 38 observations acquired by *Swift*/XRT taken in windowed timing mode. The basic data reduction was carried out using the task XRTPIPELINE with the standard filtering and screening criteria for all the observations using R.A. (=$16^{\rm h}59^{\rm m}01.679^{\rm s}$) and Dec (=$15^\circ 15' 28.54''$) positions, as determined from the UVOT images by Kennea et al. (2011). The first few observations are long pointed observations with multiple pointings. The spectra were generated from individual pointings for all of the observations resulting in a total of 80 spectra from 38 observations. The source and background spectra were extracted using a circular region with a 20 pixel radius. The count rate for a few observations is above 150 count $\rm s^{-1}$, suggesting that these might be affected by a moderate pile-up. However, the count rate is below 300 count $\rm s^{-1}$ for all the cases and hence the effect of pile-up can be removed by ignoring one brightest pixel from the extraction region as suggested by Romano et al. (2006). Hence, we re-extracted the source spectra for all these observations after removing the brightest pixel. The ancillary response files were generated using the task `XRTMKARF`, corrected for hot columns and bad pixels along with PSF correction. The RMF files, necessary to fit the spectrum in `XSPEC`, were from `CALDB` as obtained from the task `XRTMKARF`. The spectra were grouped to obtain a minimum of 20 counts in each bin. The XRT spectra were extracted covering an energy range of 0.7–9 keV. Also, the energy range of 1.7–2.5 keV was ignored in all XRT spectra because of the presence of large residuals in almost all the spectra.

3 SPECTRAL ANALYSIS AND RESULTS

The spectrum of a black hole binary broadly consists of two components: a multi-temperature accretion disk component and a Comptonized component of radiation coming from the corona. The disk component is typically fitted with a multi-temperature disk blackbody model `DISKBB`. The model, `DISKBB`, is an old model (Mitsuda et al. 1984; Makishima et al. 1986) that calculates the accretion disk spectrum by ignoring the zero-stress inner boundary condition. It has two parameters, viz. the temperature at the inner disk radius and the normalization, which represents a combination of the inner disk radius $R_{\rm in}$ and two geometry dependent parameters, orbital inclination and distance to the source. Thus, estimation of the inner disk radius using `DISKBB` requires an accurate knowledge of both the distance and orbital inclination, which are not generally available for newly discovered sources. `DISKPN` is an alternate model describing a multi-temperature disk (Gierliński et al. 1999). It calculates the disk spectrum by considering the pseudo-Newtonian potential, which provides a more accurate description of the gravitational potential in the vicinity of the black hole. An important aspect of `DISKPN`, particularly in the context of the present work, is that it considers the inner disk radius to be an independent parameter in the units of gravitational radius, $R_{\rm g}$. It should be noted that there are other, fully relativistic, and hence more accurate, disk models such as `KERRBB` available in `XSPEC`. However, such models always assume the accretion disk extends to the ISCO and thus cannot be used to model the spectrum of a truncated disk. Hence, we use `DISKPN` to model the multi-color accretion disk component in our spectral analysis. The normalization of `DISKPN` presents a combination of geometry dependent parameters (apart from the color correction factor, which is typically assumed to be 1.7 in literature). Utilizing this feature of `DISKPN`, we fit multiple spectra simultaneously while tying their normalization. This results in an independent estimate of the inner radius for each spectrum and a better constraint on the normalization. The second major constituent of the black hole binary spectrum, the Comptonized component, is typically fitted with a POWERLAW as an approximation. However, this results in an underestimation of the disk flux at lower energies because of the low energy divergence of POWERLAW. Therefore, we use an alternate model, SIMPL, which represents the Comptonization process more accurately (Steiner et al. 2009). Thus we fit all the spectra with the model PHABS$\otimes$(SIMPL$\otimes$DISKPN). As expected, the fitting of an individual spectrum results in a rather poor constraint on the parameters with a large range in the normalization. Simultaneous fitting of all 80 spectra is not practically possible. Therefore, we made 10 groups from the 80 spectra such that a group has 10 spectra. In order to have a link between groups, we kept the first two spectra of a group same as the last two spectra of the previous group. Each group was fitted with the same model with the normalization tied for all the spectra. In this way, a good constraint on DISKPN normalization could be found.

From the above fits, we obtained 10 values of DISKPN normalization (N) from the spectral fitting of 10 groups and the minimum and the maximum values of N were 2.33×10^{-3} and 3.26×10^{-2} respectively. The spectral fitting in groups was not able to calculate the error for a few groups. Therefore, the maximum and minimum values of N were frozen in the spectral fitting of individual spectra. We show the parameters (with error bars) obtained from the fitting of individual spectra with frozen normalization in Figure 1. We also show the parameters obtained from the groups in all the panels. We can see from the figure that the points obtained from the fitting of individual spectra and fitting in groups match very well. All the error bars correspond to a confidence range of 90%. The reduced χ^2 values for all the 80 spectra are below 1.26 in both cases when the DISKPN normalization in the individual spectra was frozen at the minimum and the maximum values obtained from simultaneous fitting of spectra in groups. The variation in energy flux of the source is shown in panel A. Panel C shows the variation of the inner disk radius in units of gravitational radius for the maximum and minimum values for normalization of DISKPN. It is clear from the figure that the inner disk radius is at a larger distance in the beginning and it gradually decreases with time towards the black hole. This is consistent with the result shown by Done & Zycki (1999) where they demonstrated that the disk was truncated at a few tens of Schwarzschild radii during the hard state of Cyg X-1. Zdziarski et al. (2004) also reported that the inner disk was observed to have a larger radius in the hard states than in the soft states for two outbursts of GX 339-4.

4 DISCUSSION

It is well known that a typical outburst of a black hole binary system undergoes different spectral states during its evolution. These spectral states are generally understood in terms of an interplay between the direct X-ray emission from the accretion disk and its reprocessing by the Compton cloud surrounding the inner region of the disk. In the soft state, the accretion disk is believed to extend to the ISCO and the overall spectrum is dominated by the disk component. In the hard state, the accretion disk is believed to be truncated well before ISCO and the overall spectrum is dominated by the Comptonized component. Our finding that the accretion disk is truncated at the beginning of the outburst and the inner disk radius gradually reduces as the outburst progresses is consistent with this general understanding of the outburst as well as the spectral states of black hole binaries. This confirmation of the general picture has become particularly important because recently there have been a few reports contradicting the general picture of hard states (Miller et al. 2012; Reis et al. 2012, 2010; Hiemstra et al. 2011), where the hard state spectrum is modeled using models dominated by the reflection component, thus implicitly assuming the presence of the disk close to the black hole. In fact, some reports (Miller et al. 2013) model the spectrum with the power law and reflection component and completely ignoring the disk component, which would be physically inappropriate. Thus our present results reinforce the general understanding that the accretion disk is truncated in the hard state. The exact values of the inner disk radius corresponding to the minimum and the maximum

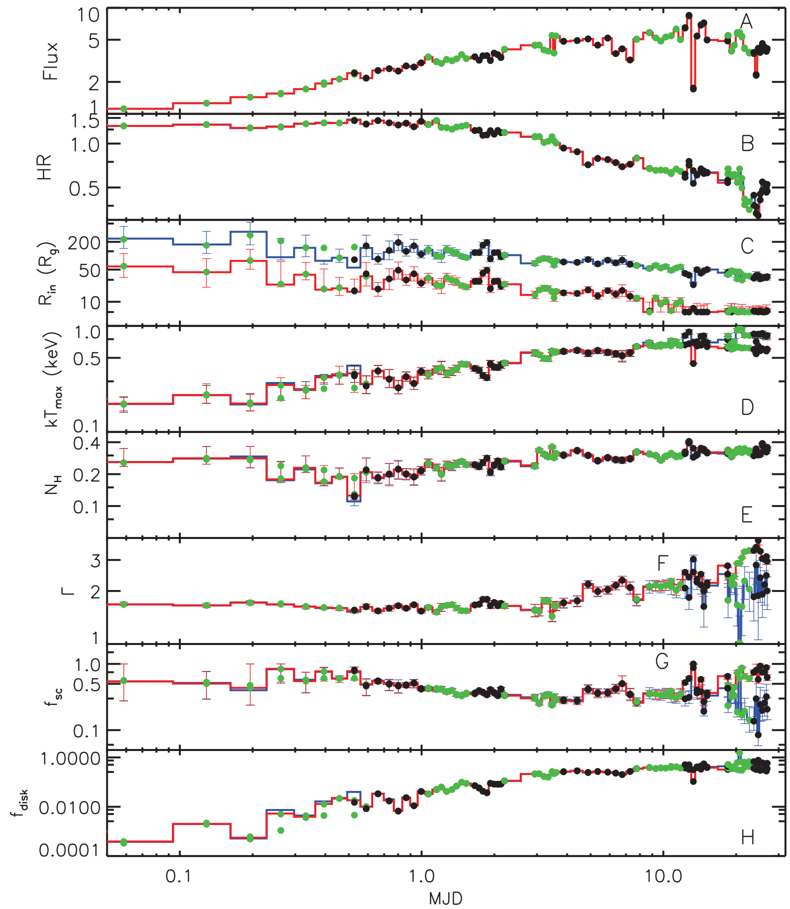

Fig. 1 A multi-panel plot showing the variation of the parameters with time, where MJD 55464.4 is taken as a reference. Red and blue solid lines correspond to the parameters obtained by freezing the normalization of DISKPN to its maximum and minimum values respectively. The parameters obtained from the fitting in groups have been overplotted with filled circles. Green and black circles have been used alternatively to differentiate parameters used for neighboring groups. See text for details.

DISKPN normalization differ as expected. Therefore, the inner disk radius for the minimum and maximum normalization is shown in separate panels in Figure 2. It is clear from Figure 2 that the inner disk radius decreases in both cases where the minimum and maximum DISKPN normalizations are applied. Since the values corresponding to the maximum DISKPN normalization are smaller, the inner disk radius reaches the minimum value of $6R_g$ as allowed by the model DISKPN, towards the later stages of the outburst as shown in the plot. Since the model DISKPN uses the Schwarzschild metric, it does not allow the R_{in} to go below $6R_g$. The dotted horizontal line in panel B of Figure 2 and the case shown in panel C of Figure 1 correspond to the inner disk radius of $6R_g$.

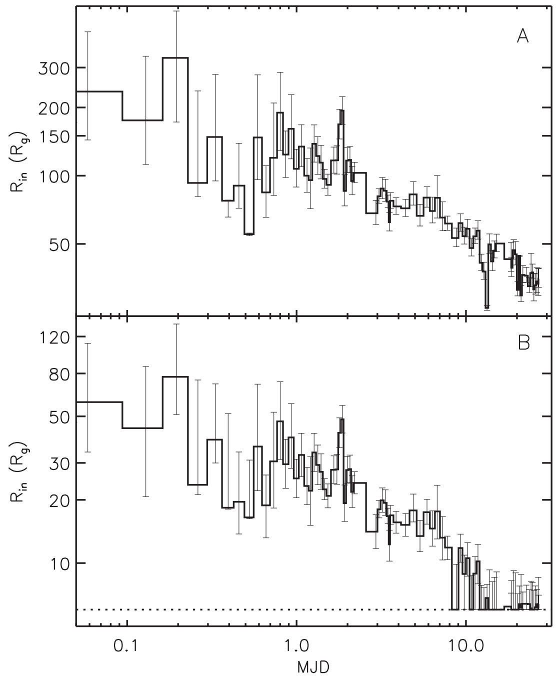

Fig. 2 The figure shows the variation of the inner disk radius, $R_{\rm in}$, with time in units of $R_{\rm g}$. MJD 55464.4 is taken as a reference. Panels A and B show the plots corresponding to the minimum and the maximum `DISKPN` normalization respectively. A dotted horizontal line at $6R_{\rm g}$ is drawn in panel B which is the minimum value allowed by the model `DISKPN`.

Panel A in Figure 1 gives absorbed total energy flux in units of 10^{-9} erg s^{-1} cm^{-2}. Panel B shows hardness ratio, HR, defined as the ratio of energy flux in the energy range 5–12 keV to the energy flux in 2–5 keV. Panels C and D in Figure 1 show the variation of the inner disk radius $R_{\rm in}$ and the maximum temperature $kT_{\rm max}$ respectively. It is clear from the plot that the maximum temperature of the blackbody component of radiation from the accretion disk was low at the beginning of the outburst and the inner edge of the disk was relatively far from the black hole. The maximum temperature increased slowly as the outburst progressed. However, during all the *Swift* observations the $kT_{\rm max}$ was found to be in the range 0.11–0.97 keV (including error bars).

We noticed small variations in $N_{\rm H}$ values during the outburst. However, the value is close to 0.3×10^{22} cm^{-2} most of the time. The variation in $N_{\rm H}$ is shown in panel E of Figure 1 in units of 10^{22} cm^{-2}. The power law index is small and the spectrum is hard at the beginning of the outburst and it softens as the outburst progresses. The power law index for the maximum normalization shows significant softening in the spectra towards the end of the plot, in contrast to the minimum normalization. The power law index is also well constrained, corresponding to the maximum normalization. This, along with the values of the inner disk radii, shows that the spectral parameters corresponding to the maximum normalization are more physical. The variation in power law index is shown in panel F of Figure 1. Panel G of Figure 1 shows the scattering fraction which is obtained from the model component SIMPL. The scattering fraction gives the fraction of seed photons coming from the disk which are Compton up-scattered in the corona (Steiner et al. 2009).

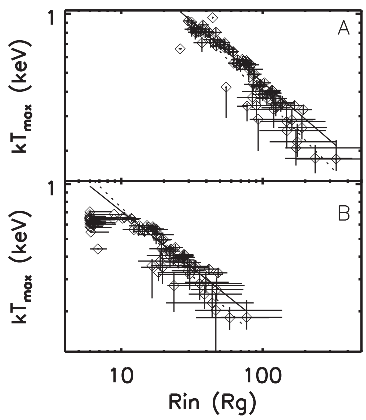

Fig. 3 The figure shows the variation of $kT_{\rm max}$ and $R_{\rm in}$ as obtained from spectral fits when `DISKPN` normalization was frozen at the minimum (*panel A*) and the maximum values (*panel B*). The solid and the dotted lines are the best-fit and standard results respectively.

We studied the ratio of unabsorbed energy flux from the disk to the unabsorbed total energy flux in the energy range 2–10 keV and the plot is shown in panel H of Figure 1. It can be seen that all the observations show consistent behavior of increasing disk fraction as the outburst progresses. It should be noted that one observation (ObsId 00434928028 on MJD 55485) shows a peculiar behavior of disk fraction corresponding to the minimum normalization > 1, which is a fitting artifact. This happens because the *Swift*/XRT spectrum alone is not able to properly constrain the power law giving the best fit power law index of $\Gamma \sim$1 which is unphysical. We have verified this by simultaneously fitting this particular spectrum with the nearest *RXTE*/PCA spectrum, where the simultaneous fit gives the power law index of $\Gamma \sim 2.2$ and the proper disk fraction (< 1). However, we have included here the values obtained from the *Swift*/XRT spectrum only because the *RXTE* observations are not available for the full duration of the *Swift* observations. We also studied the hardness ratio defined above and show the values in panel B of Figure 1. It is clear from the plot that the spectrum was hard in the beginning of the outburst and then it slowly softened. The softening of the source continued until the end of *Swift* coverage. The hardness ratio and the inner disk radius seem to be correlated and the correlation coefficient is 0.71 and 0.74 for the minimum and maximum normalization respectively. This is consistent with the general understanding that as the disk region increases with decreasing inner disk radius, the fraction of soft photons coming from the disk increases thereby making the hardness ratio small. Also, the correlation coefficients between disk-to-total flux ratio and the hardness ratio are –0.83 and –0.92 for the minimum and maximum normalizations respectively.

A sharp variation in almost all the parameters is observed between MJD 55477 and 55478. This is because of an observation with ObsID 00434928018. The count rate for this observation is only 42.49 cts s^{-1}. This may be one of the extended dips observed in this source. We studied the variation of the maximum blackbody temperature and the inner disk radius from individual fitting of spectra with normalization frozen at the minimum and maximum normalizations.

Figure 3 shows the plots obtained between $kT_{\rm max}$ and $R_{\rm in}$ for the maximum and the minimum normalizations. We fitted the plot and found the best fit to be $kT_{\rm max} = (7.75{\pm}0.93)\, R_{\rm in}^{-0.62\pm0.03}$ keV for the minimum normalization and $kT_{\rm max} = (2.96 \pm 0.38)\, R_{\rm in}^{-0.62\pm0.04}$ keV for the maximum normalization. We ignored the values of $R_{\rm in}$ where the lower bound is not constrained, to find the best fit corresponding to the maximum normalization. This result is comparable to the result given by

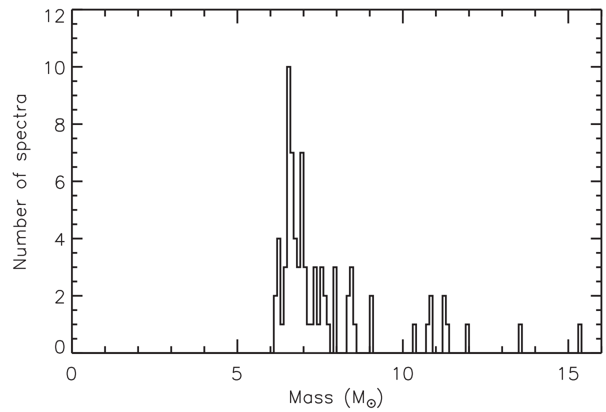

Fig. 4 Histogram of the black hole mass obtained from 79 spectra.

Kennea et al. (2011), though they fitted individual spectra separately with `DISKBB` and we fitted with `DISKPN` with normalization frozen at certain values in all the spectra, in order to tie the geometry dependent parameters. The results deviate from the standard result of $T_{\max} \propto R_{\mathrm{in}}^{-0.75}$. This deviation can be attributed to variation in the accretion rate as the outburst progresses.

We made an attempt to estimate the mass of the black hole using the maximum and the minimum values of normalization. We estimated the mass of the black hole with the following expression, which is taken from Gierliński et al. (1999),

$$M = \left[\frac{N}{(1 - f_{\mathrm{sc}})} \frac{D^2 f_{\mathrm{col}}^4}{\cos i} \right]^{1/2} , \tag{1}$$

where M is mass in solar units, N is normalization obtained from the disk component `DISKPN`, f_{sc} is scattering fraction obtained from the Comptonization component `SIMPL`, D is distance in kpc, f_{col} is the spectral hardening factor and i is inclination in degrees. The fitted value of normalization can be used to estimate the black hole mass because inclination and distance are relatively well constrained for MAXI J1659–152. The inclination angle is constrained in the range 60°–75° based on the presence of dips and absence of eclipses in the light curves of the source (e.g. Kennea et al. 2011; van der Horst et al. 2013; Kuulkers et al. 2013). A number of distance estimates are available for the source which are in good agreement with most of the estimates close to 6 kpc (Kennea et al. 2011; Kaur et al. 2012; Jonker et al. 2012). Since the scattering fraction f_{sc} is different for all 80 spectra, we obtain a total of 80 values for the mass assuming a distance of 6.0 kpc, inclination angle of 70° and the canonical value of 1.7 for the spectral hardening factor. A histogram of 79 out of these 80 mass values is shown in Figure 4. We ignored one observation (ObsID 00434928018) for the mass estimation because the scattering fraction for this observation was very high (~ 1), resulting in a very high value of mass. We calculated the black hole mass to be 7.9±2.4 $M_\odot$ using a weighted average of these values. If we consider the uncertainty in distance (within 5 to 6 kpc), inclination angle (within 65° to 75°) and spectral hardening factor (within 1.6 to 1.8), the average mass comes out to be 8.1±2.9 $M_\odot$. It should be noted that these estimates are obtained using the maximum normalization from our simultaneous fitting. For the minimum normalization, all the values of mass are found to be lower than 3 $M_\odot$ and hence are ignored. This mass estimate, therefore, can be considered to be an absolute upper limit for the black hole in MAXI J1659–152.

5 CONCLUSIONS

We carried out a detailed spectral analysis of the 2010 outburst of the black hole candidate MAXI J1659–152 with a different spectral model. The outburst lasted for almost one and a half months and has been studied by many authors. We fitted spectra of the outburst with a more physical model that included `DISKPN` and `SIMPL`. The normalization of `DISKPN` was frozen at certain values obtained from simultaneous fitting of spectra in groups. We found an upper limit on the mass of the black hole to be 8.1$\pm$2.9 $M_{\odot}$. We studied the variation of the inner disk radius during the outburst using a simultaneous fitting method. We have observed a very systematic variation in the inner disk radius as the outburst progressed. The disk was initially found to be truncated at a larger radius of about a few hundred Schwarzschild radii when the source was in the early stages of the outburst. This, probably, is the first observational evidence of an accretion disk closing-in as the outburst progresses. We see the result as a supporting evidence for the truncation model amongst the growing evidence against the truncation model.

Acknowledgements We thank the referee, Prof. Andrzej Zdziarski, for his valuable comments which helped to improve the manuscript. This research has made use of data obtained from the High Energy Astrophysics Science Archive Research Center (HEASARC), provided by NASA's Goddard Space Flight Center.

References

Belloni, T. 2004, Nuclear Physics B Proceedings Supplements, 132, 337
Done, C., Gierliński, M., & Kubota, A. 2007, A&A Rev., 15, 1
Done, C., & Zycki, P. T. 1999, MNRAS, 305, 457
Fender, R. P., Homan, J., & Belloni, T. M. 2009, MNRAS, 396, 1370
Gehrels, N., Chincarini, G., Giommi, P., et al. 2004, ApJ, 611, 1005
Gierliński, M., Zdziarski, A. A., Poutanen, J., et al. 1999, MNRAS, 309, 496
Hiemstra, B., Méndez, M., Done, C., et al. 2011, MNRAS, 411, 137
Homan, J., Wijnands, R., van der Klis, M., et al. 2001, ApJS, 132, 377
Jonker, P. G., Miller-Jones, J. C. A., Homan, J., et al. 2012, MNRAS, 423, 3308
Kalamkar, M., Homan, J., Altamirano, D., et al. 2011, ApJ, 731, L2
Kaur, R., Kaper, L., Ellerbroek, L. E., et al. 2012, ApJ, 746, L23
Kennea, J. A., Romano, P., Mangano, V., et al. 2011, ApJ, 736, 22
Kuulkers, E., Kouveliotou, C., Belloni, T., et al. 2013, A&A, 552, A32
Lasota, J.-P. 2001, New Astron. Rev., 45, 449
Makishima, K., Maejima, Y., Mitsuda, K., et al. 1986, ApJ, 308, 635
Mangano, V., Hoversten, E. A., Markwardt, C. B., et al. 2010, GRB Coordinates Network, 11296, 1
Matsuoka, M., Kawasaki, K., Ueno, S., et al. 2009, PASJ, 61, 999
Miller, J. M., Parker, M. L., Fuerst, F., et al. 2013, ApJ, 775, L45
Miller, J. M., Pooley, G. G., Fabian, A. C., et al. 2012, ApJ, 757, 11
Mitsuda, K., Inoue, H., Koyama, K., et al. 1984, PASJ, 36, 741
Muñoz-Darias, T., Motta, S., Stiele, H., & Belloni, T. M. 2011, MNRAS, 415, 292
Narayan, R., & Yi, I. 1994, ApJ, 428, L13
Negoro, H., Yamaoka, K., Nakahira, S., et al. 2010, The Astronomer's Telegram, 2873, 1
Qiao, E., & Liu, B. F. 2009, PASJ, 61, 403
Rao, A., & Vadawale, S. V. 2012, ApJ, 757, L12
Reis, R. C., Fabian, A. C., & Miller, J. M. 2010, MNRAS, 402, 836

Reis, R. C., Miller, J. M., Reynolds, M. T., Fabian, A. C., & Walton, D. J. 2012, ApJ, 751, 34
Romano, P., Campana, S., Chincarini, G., et al. 2006, A&A, 456, 917
Steiner, J. F., Narayan, R., McClintock, J. E., & Ebisawa, K. 2009, PASP, 121, 1279
van der Horst, A. J., Curran, P. A., Miller-Jones, J. C. A., et al. 2013, MNRAS, 436, 2625
Yamaoka, K., Allured, R., Kaaret, P., et al. 2012, PASJ, 64, 32
Zdziarski, A. A., Gierliński, M., Mikołajewska, J., et al. 2004, MNRAS, 351, 791

Draft version December 8, 2015
Preprint typeset using LaTeX style emulateapj v. 5/2/11

INVESTIGATING THE CONNECTION BETWEEN QUASI PERIODIC OSCILLATIONS AND SPECTRAL COMPONENTS WITH NuSTAR DATA OF GRS 1915+105

Anjali Rao Jassal, Santosh V. Vadawale, and Mithun N. P. S
Physical Research Laboratory, Ahmedabad- 380009, India

Ranjeev Misra
Inter-University Center for Astronomy and Astrophysics, Post Bag 4, Ganeshkhind, Pune 411007, India

Draft version December 8, 2015

ABSTRACT

The low frequency quasi periodic oscillations (QPOs) are commonly observed during hard states of black hole binaries. Several studies have established various observational/empirical correlations between spectral parameters and QPO properties, indicating a close link between the two. However, the exact mechanism of generation of QPO is not yet well understood. In this paper, we present our attempts to comprehend the connection between the spectral components and the low frequency QPO observed in GRS 1915+105 using the data from NuSTAR. Detailed spectral modeling as well as the presence of the low frequency QPO and its energy dependence during this observation have been reported by Miller et al. (2013) and Zhang et al. (2015) respectively. We investigate the compatibility of the spectral model and energy dependence of the QPO by simulating light curves in various energy bands for small variation of the spectral parameters. The basic concept here is to establish connection, if any, between the QPO and the variation of either a spectral component or a specific parameter, which in turn can shed some light on the origin of the QPO. We begin with the best fit spectral model of Miller et al. (2013) and simulate the light curve by varying the spectral parameter at frequencies close to the observed QPO frequency in order to generate the simulated QPO. Further we simulate similar light curves in various energy bands in order to reproduce the observed energy dependence of RMS amplitude of the QPO. We find that the observed trend of increasing RMS amplitude with energy can be reproduced qualitatively if the spectral index is assumed to be varying with the phases of the QPO. Variation of any other spectral parameter does not reproduce the observed energy dependence.

Subject headings: accretion, accretion disks — black hole physics — X-rays: binaries — X-rays: individual (GRS 1915+105)

1. INTRODUCTION

Accreting black hole binaries show variability on a wide range of timescales from milli-seconds to months and years. While the long term variability typically arises due to the transient nature or the state transitions, the short term (sub-second) variability is generally attributed to the processes in the inner regions of accretion disk. A perplexing feature of such a short term variability is the presence of quasi periodic oscillations, characterized by a narrow peak superimposed over a broad band noise in the power density spectrum (PDS). QPOs have been observed in a frequency range of less than Hz to hundreds of Hz (Remillard & McClintock 2006) and they are generally classified as low frequency QPOs (LFQPOs, 0.1-30 Hz) and high frequency QPOs (HFQPOs, 40-450 Hz). Frequency of HFQPOs does not vary with a sizeable change in luminosity suggesting that it depends on the fundamental system parameters such as black hole mass and spin (Remillard & McClintock 2006; Remillard et al. 2006).

It is evident that the LFQPOs are not linked with the orbital motion of the material in the disk because the observed frequencies correspond to the far outer regions of the accretion disk. The properties of these QPOs (e.g. low frequency break, centroid frequency, rms amplitude) are strongly coupled with the changes in spectrum and luminosity (see Muno et al. 1999; Sobczak et al. 2000; Vignarca et al. 2003; Li et al. 2014), suggesting that these QPOs originate in the same inner region of the accretion disk. Despite the knowledge of empirical correlations of QPO properties with spectral parameters (e.g. Sobczak et al. 2000; Stiele et al. 2013), the exact physics is not very well understood. There are several models to explain the origin and properties of LFQPOs. In one of the most promising models, the LFQPO originates as a result of relativistic Lense-Thirring (LT) precession of the hot inner flow (Stella & Vietri 1998; Wagoner et al. 2001; Schnittman et al. 2006; Ingram & Done 2012). The model successfully explains the variation of frequencies of QPO centroid and the low frequency break in terms of variation in the truncation radius of the inner disk. Another model based on the accretion ejection instability suggests that a QPO is produced by a spiral pattern rotating at a frequency of a few tenths of the Keplerian frequency at the inner edge of the disk (Tagger & Pellat 1999; Varnière et al. 2002; Rodriguez et al. 2002). However, according to the shock oscillation model, wherein a shock is formed by a centrifugal barrier in a region of lower viscosity, LFQPOs are originated due to oscillation of the post-shock region (Molteni et al. 1996; Chakrabarti et al. 2004; Garain et al. 2014).

Most of the available QPO models explain the frequencies and some of the observed correlations along with other timing and spectral properties. However, in many cases, the models are silent about the energy dependence of the QPO or the exact mechanism of origin of the QPO. Observing a QPO as a direct oscillation of one or more spectral parameter could provide much deeper insights in the modulation mechanism and thus origin of the QPO. In this context, here we attempt to investigate the observed energy dependence of the LFQPO in GRS 1915+105 in terms of modulation of the spectral parameters.

GRS 1915+105 is one of the most enigmatic black hole binary system famous for its relativistic jets exhibiting superluminal motion (Mirabel & Rodríguez 1994) and a variety of variability patterns (Fender & Belloni 2004). Its LFQPOs and their correlations with various other parameters have been studied extensively (Maccarone et al. 2011; Mikles et al. 2006; Rodriguez et al. 2002; Muno et al. 1999; Morgan et al. 1997, etc.). However, another intriguing aspect of this system is the spin of the black hole. Various reports have found spin of GRS 1915+105 ranging from 0.56 (Blum et al. 2009) to $\sim$0.98 (McClintock et al. 2006; Blum et al. 2009). Probably, the most accurate spin estimate for GRS 1915+105 is available from the NuSTAR observation (Miller et al. 2013, hereafter M13), where the lower values of spin are ruled out at a high level of confidence based on the accurate modeling of relativistically blurred reflection. This observation belongs to a special state of GRS 1915+105 known as 'plateau' state and it shows a QPO with frequency of 1.5 Hz. Properties of this LFQPO have been studied in detail by Zhang et al. (2015, hereafter Z15) where the authors show that the RMS amplitude of the QPO increases with energy with a characteristic flattening between 10−20 keV. This suggests the possibility of an interplay between independently varying spectral parameters. Thus investigation of the spectral parameter(s), which lead to the observed energy dependence of the QPO power can provide significant clues on the origin of the QPO.

In this context, here we delve into the energy dependence of the QPO power by means of simulating light curves by varying different spectral parameter(s). In the next section, we discuss the NuSTAR observation and its analysis to reproduce the results of M13 and Z15. The results of these spectral and timing analysis are used to generate the simulated light curve as explained in the following section, with the discussion on our findings and preliminary conclusions in the subsequent sections.

2. OBSERVATION AND DATA ANALYSIS

The NuSTAR observation of GRS 1915+105 carried out on July 03, 2012 has been used for the present study. The same observation has been analyzed in detail by M13 and Z15 for spectroscopic and timing studies respectively. We extract the spectrum following M13 and adopt their best fit model, `tbabs`×(`kerrconv`⊗`reflionx_hc` + `cutoffpl`) where the reflection of the primary cutoff power law is modeled by `reflionx_hc` (a variant of `reflionx` model), which assumes the incident spectrum as cut-off power law. With the same spectral model, we ensure that the best fit results are almost identical, which are then used in our simulations as explained in the next section.

We also carried out the timing analysis on the line of Z15. The light curves are extracted in an energy range of 3-80 keV with a bin size of 100 ms. PDS is generated for each interval of 1024 bins and co-added for all the intervals. The PDS from both FPMA and FPMB show a very strong type-C QPO at $\sim$1.5 Hz. The PDS also shows strong spikes at every 1 Hz, however, it is known that these are instrumental artifacts in the early NuSTAR observations and hence we ignore these bins during fitting in `XSPEC`. The light curves from FPMA and FPMB are added together in order to improve the statistics and the PDS is generated from the combined light curve (Fig. 1 left panel). We fit the PDS using multiple lorentzians and a constant, which takes care of white noise level in the PDS. It is obvious that the PDS has many complex features such as broad band noise, a small peak at frequency of $\sim$0.75 Hz and a strong QPO at $\sim$1.5 Hz. Here we concentrate only on the $\sim$1.5 Hz QPO feature because it is known to have systematic dependence on energy (Fig. 1 right panel). The small peak at $\sim$0.75 Hz has been described as a sub-harmonic by Z15. However for the purpose of the present work, we consider it as a part of broad band noise mainly because of very low Q value of $\sim$3.6. Z15 have reported that the RMS amplitude of the QPO increases with energy. We verify this from the light curves in different energy bands (3−4 keV, 4−5 keV, 5−6 keV, 6−7 keV, 7−9 keV, 9−12 keV, 12−15 keV and 15−30 keV).

We find an increasing trend with a shallow dip (or flattening) in 10−20 keV as reported in Z15 (Fig. 1 right panel). They have also reported that this observation shows increase in count rate as well as QPO frequency during the later part (after $\sim$40 ks of the start of the observation). Therefore, we restrict both the spectral and timing analysis to the first 40 ks of data, where the count rate and QPO frequency are quite stable. Effective exposure times for our analysis are 9.71 ks and 10.01 ks for FPMA and FPMB respectively.

3. LIGHT CURVE SIMULATION AND RESULTS

In many cases, the observed spectrum can be explained with different models with same statistical significance. In such cases, the compatibility of a spectral model with the observed timing characteristic can be helpful to solve the degenracy. The main objective of the present work is to investigate the compatibility of the observed QPO properties with the spectral model. One possibility to achieve this is by comparing the amplitude of the oscillations across multiple energy bands. Another possibility is by comparing the phase lags in a similar manner. Black hole binaries are known for showing phase lags between different energy bands. Phase lags for GRS 1915+105 has also been reported by several authors (e.g Reig et al. 2000; Qu et al. 2010; Lin et al. 2000), wherein it is generally found that the hard photons lag the soft photons. We also calculated phase lags between different energy bands using NuSTAR data, however because of the relatively poor statistics (compared to e.g. RXTE-PCA), the phase lags can not be constrained (obtained values are consistent with zero with larger error bars) with the present data. Hence we adopt the alternate method by comparing the observed energy dependence of the QPO RMS amplitude with the simulated energy dependence.

An important feature of the present best fit spectral

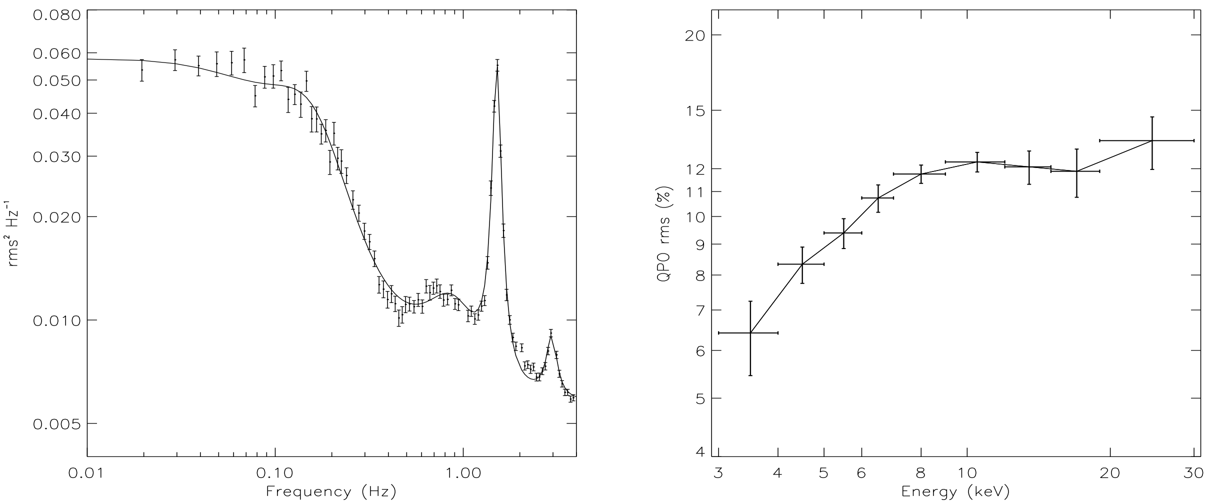

Figure 1. Figure shows the observed PDS (left) in the energy range of 3-80 keV and the energy dependence of QPO power (right).

Table 1
The best fit spectral parameters calculated with the model `tbabs`×(`kerrconv`⊗`reflionx_hc + cutoffpl`). Errors indicate 90% confidence intervals.

Parameter	Best fit value
N_H ($\times 10^{22}$cm^{-2})	$4.43^{+0.18}_{-0.05}$
Index 1	$9.99_{-0.06}$
Index 2	$0.01^{+0.02}$
R$_{in}$ (R$_g$)	$7.49^{+0.07}_{-0.06}$
a$_*$	$0.973^{+0.002}_{-0.002}$
i	$65.41^{+1.02}_{-0.39}$
Γ	$1.709^{+0.001}_{-0.001}$
Xi	$993.0^{+14.8}_{-19.0}$
A_{Fe}	$0.97^{+0.02}_{-0.13}$
Cut-off Energy	$35.47^{+1.19}_{-0.18}$
N_{ref} ($\times 10^{-5}$)	$1.19^{+0.20}_{-0.02}$
N_{pl}	$1.907^{+0.008}_{-0.007}$

model is that it consists of only one primary continuum component, cut-off power law, covering the full energy range. Hence, it does not allow interpretation of the QPO in terms of oscillation of one of the spectral component as suggested by Rao et al. (2000) (also corroborated by Vadawale et al. 2001, 2003). Thus observed energy dependence of the QPO power must result from the variation of one or more spectral parameters.

Here we assume that a particular spectral parameter varies with a frequency close to the observed QPO frequency. We consider four possible parameters of the spectral model, viz. the spectral index, normalization of the cut-off power law, normalization of the reflection component and the ionization parameter; which can vary with the phases of the QPO. Though the high energy cut-off can vary, we keep it fixed at the best fit value because its variation does not affect the model in the energy range of interest. All parameters of `kerrconv` are assumed not to vary with the phases of the QPO. We then simulate the light curve with a bin size of 100 ms. Initially we simulate the light curve for variation of only one parameter. As a zeroth order approximation, we assume that the parameter is varying sinusoidally with QPO phases in a range centered at the best fit value. The assumption of sinusoidal oscillation is clearly an over simplification and the actual oscillation profile could be more complex. However, the energy dependence of RMS amplitude is not likely to have strong dependence on the exact shape of oscillations. We also include a small random variation over the sinusoidal variation to be a bit more realistic. Later we also simulate the light curve for multiple parameters varying simultaneously. In either case the basic algorithm for simulation of light curve is as follows-

It is assumed that a parameter α obtained from the best-fit spectral model varies at a frequency close to the observed QPO frequency ($\bar{\nu}$). The amplitudes of the sinusoidal variation and random fluctuation are p_α and q_α respectively such that q_α = r p_α. The simulation is carried out for r=0.1, 0.2 and 0.3 and it is found that the results remain unaffected. Therefore, we present results hereafter for r=0.1 (i.e. 10% random variations superimposed over the sinusoidal oscillations).

- Let m_α be the best fit value of parameter α.

- The spectral model is evaluated in `XSPEC` with the parameter α assuming values in the range $m_\alpha \pm p_\alpha$, keeping the rest of the parameters at their best fit values. Model counts, including the effects of detector response matrix as well as effective area, are obtained in each of the energy bins and are tabulated.

- The light curve is simulated with a bin size of 100 ms for a duration of $\sim$ 10 ks to match the exposure time of the observation.

- For each interval ($\sim$ 2 s) a random frequency of oscillation (ν) is drawn from a lorentzian distribution with the mean $\bar{\nu}$ (=1.5 Hz) and the FWHM (=0.089 Hz) values same as those for the observed QPO. The frequency remains the same throughout an interval. We have also verified that the overall results remain unaffected if the frequency is changed more often within one interval. It is assumed here that the quasi periodic nature arises due to frequency modulation (see Rao et al. 2010).

- The phase of oscillation for each time bin i is obtained by

$$\phi_i = 2\ \pi\ \nu\ \Delta t\ +\ \phi_{i-1}$$

where Δt is the bin size and ϕ_{i-1} is the phase for previous time bin. Continuity of the phases across intervals is also maintained in the same manner.

- The value assumed by parameter α for the i-th timebin is calculated as

$$\alpha_i = p_\alpha\ sin(\phi_i) + q_\alpha\ z_i$$

where z_i is a standard normal variate (see Fig 5, left panel).

- Mean counts in the time bin i for a given energy bin j ($\bar{C_{ji}}$) corresponding to value α_i is obtained from the table generated in the first step. The energy bin j is kept same as that used to extract the observed light curves.

- Random number is generated from Poisson distribution with mean $\bar{C_{ji}}$ and is recorded as counts in the i-th time bin of the light curve in energy bin j.

- Power density spectra are generated for these simulated light curves using `POWSPEC` and are fitted with `XSPEC` as usual.

Fig (2) shows a section of the simulated light curve and its PDS in an energy range of 9−12 keV. It should be noted that we have not included low frequency noise in our simulations because our primary objective here is to investigate the energy dependence of the QPO power. Fig (3) summarizes the overall results of our simulations. The four panels show the simulated energy dependence of the QPO power for variation of the four spectral parameters. The observed energy dependence is shown with black solid line in all the panels. For each parameter, multiple lines are shown corresponding to the three different range of variation of parameters. It can be seen that only the variation of spectral index can reproduce the overall trend of the increasing QPO power with energy. Variation of other three parameters cannot reproduce the observed trend. Even in the case of the spectral index variation, the exact shape of the energy dependence curve, particularly the dip or flattening in the energy range of 10−20 keV is not reproduced. This suggests that, while the variation of spectral index during QPO phases is essential it is not the only source of the variability. Hence we test the hypothesis by simulationg the light curves considering the variation of more than one parameter simultaneously. The simulation was repeated for the variation of two and three parameters and the results are shown in Fig (4) and (5) respectively. Since the reflection component represents the Comptonization component reflected from the disk, it is expected that the former would be stronger for a harder spectrum. Or in other words, the reflection component should be anticorrelated with the spectral index. Therefore, the parameters of reflection component (N_{ref} and Xi) were varied out of phase with spectral index in the simulation of light curves. Panel A of Fig (4) shows the energy dependence obtained from the variation of reflection normalization (N_{ref}) and spectral index and Panel B shows the results for ionization parameter (Xi) and spectral index. A comparison of Panel A of Fig (3) and Fig (4) shows that the variation of spectral index and normalization of reflection reproduce the observed energy dependence more closely than the variation of spectral index alone. We also studied the energy dependence with the light curves simulated by varying 1) normalization of cutoff power law and normalization of reflection component and 2) normalization of cut-off power law and ionization parameter. The variation of the two set of parameters does not reproduce the observed increasing trend of QPO power.

We have further attempted to reproduce the observed pattern by varying three parameters simultaneously. The left panel of Fig (5) shows the variation of spectral parameters with time. Representative results obtained from the variation of three parameters are shown in the right panel of Fig (5). It can be seen that the results start resembling the observed pattern more closely. We avoid attempts to exactly reproduce the observed pattern as this will require detailed fine tuning of the specifics such as number of varying parameters, amplitudes of variation, phase lags etc. More importantly, a relook into the spectral model itself might also be necessary which is beyond the scope of this paper. The main objective here is to convey that the present best fit spectral model is compatible with the observed trend of the increasing QPO power with energy when the spectral index is assumed to be varying. However, it might be necessary to look beyond this model in order to reproduce the exact energy dependence of the QPO power.

4. DISCUSSION AND CONCLUSIONS

Increasing trend of the LFQPO power with energy is well known (e.g. Tomsick & Kaaret 2001; Rodriguez et al. 2004, 2008). The trend can also be seen in the results shown by Zdziarski et al. (2005); Sobolewska & Życki (2006). However, origin of this trend in terms of variation of the spectral components has not been investigated so far. Here we attempt to explain the energy dependence of LFQPO observed during the first NuSTAR observation of GRS 1915+105. We simulate the light curve for variation of various spectral parameters and compare the resultant energy dependence with the observed one. We find that only variation of the spectral index reproduces the overall trend of the increasing QPO power with energy. Variation of

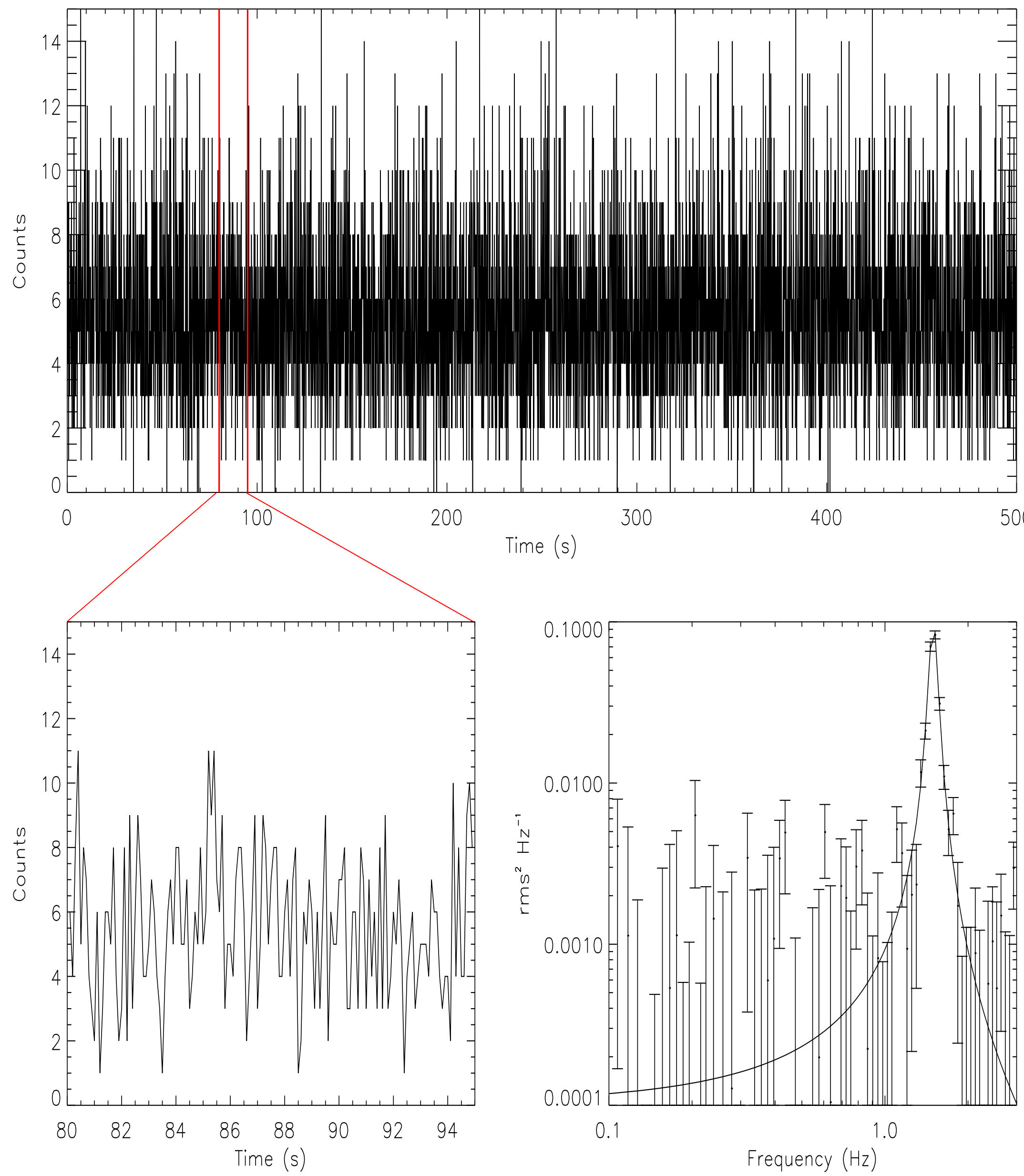

Figure 2. The upper panel shows the first 500 seconds of a 9-12 keV light curve simulated by modulating the spectral index. A zoomed-in view of a section of the light curve is shown in the lower-left panel. PDS of the full light curve is shown in lower right panel.

any other parameter does not reproduce the observed trend. This has significant implications on the feasibility of various models proposed to explain the origin of the QPO. For example, the fact that the variation of reflection normalization does not reproduce the observed trend suggests that the QPO models based on geometric modulation (Miller & Homan 2005) may not be realistic.

Among the other existing models for the low frequency QPOs, the model based on Lense-Thirring precession is considered the most successful model. It successfully explains the overall shape of the PDS and the variation of QPO frequency with the changes in spectral hardness, which is further linked with the truncation radius of the inner disk (Ingram & Done 2010). However, the energy dependence of QPO is not apparently clear. The similar situation exists with a magnetohydrodynamic model for QPO based on the accretion ejection instability (Tagger & Pellat 1999; Varnière et al. 2002; Rodriguez et al. 2002). The shock oscillation model (Molteni et al. 1996; Chakrabarti et al. 2004; Garain et al. 2014) does produce the spectral variation and it could be compatible with the energy dependent QPO power. However, the simulation results obtained from the present spectral model cannot be directly compared with the predictions of shock oscillation model. It might be necessary to perform similar simulation with appropriate model and then verify the results.

Another observation is the flattening of QPO spectrum at 10-20 keV which cannot be reproduced with variation of only spectral index. The flattening seems to be

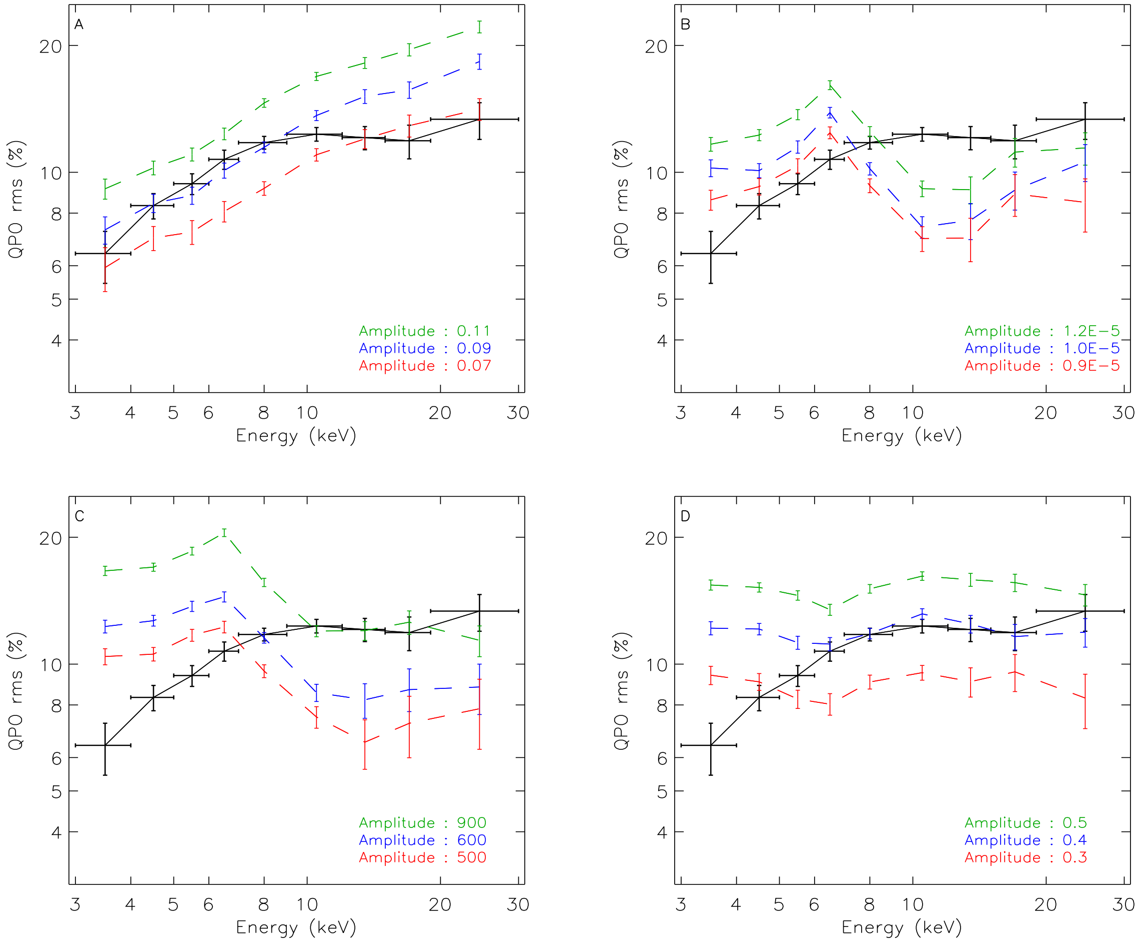

Figure 3. Figure shows the simulated energy dependence of QPO obtained by modulation of spectral index (A), normalization of reflionx_hc (B), ionization parameter (C) and normalization of cut-off power law (D). The dashed lines correspond to simulation results for different amplitudes of modulation. The observed energy dependence is shown with black solid line in all the panels.

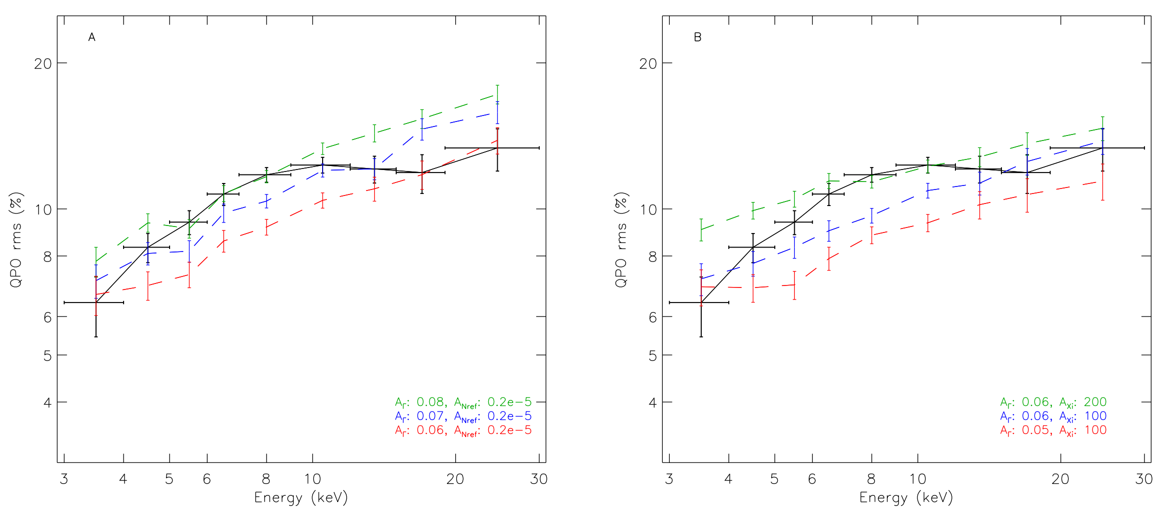

Figure 4. Plot showing the energy dependence of QPO with the simulated light curves by varying two parameter simultaneously. Panel A shows the results obtained from the variation of normalization of reflection and spectral index. Panel B shows the result for the variation of ionization parameter and spectral index. The dashed lines correspond to simulation results for different amplitudes of modulation. The observed energy dependence is shown with black solid line in both the panels.

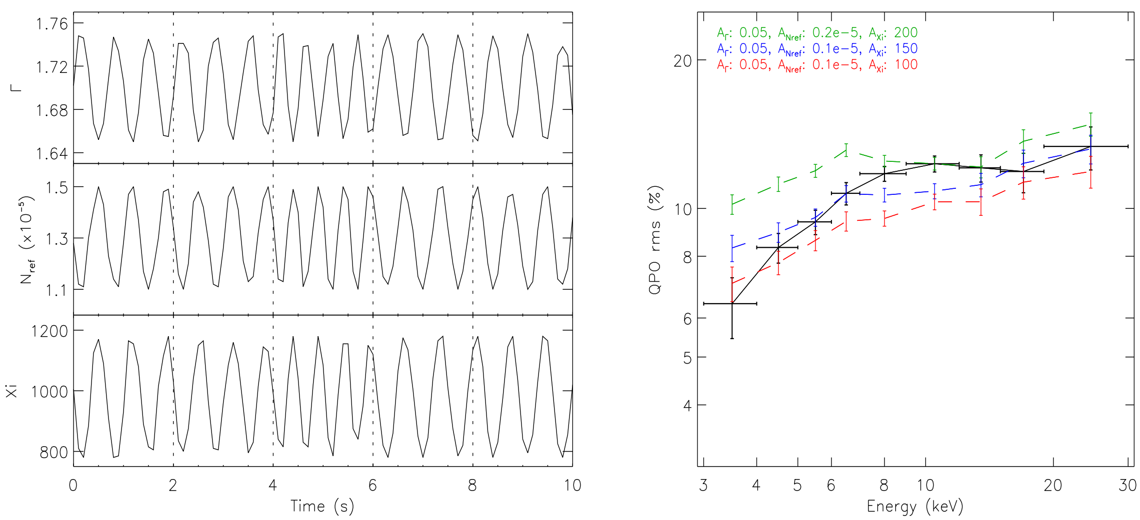

Figure 5. The left panel shows the variation of three spectral parameters; spectral index (Γ), reflionx_hc normalization (N_{ref}), and ionization parameter (Xi). The reflection normalization and ionization are varied in same phase which are assumed to be anti-correlated to the phase of spectral index variation. The dashed lines separate the intervals corresponding to different frequencies of modulation. The right panel shows the simulated energy dependence of QPO power obtained by modulation of three parameters. Amplitudes of modulation for Γ, N_{ref}, and Xi are mentioned in the figure.

more common as it has been observed at many other occasions (e.g. Tomsick & Kaaret 2001; Rodriguez et al. 2004, 2008; Zdziarski et al. 2005; Sobolewska & Życki 2006). Similar feature is also found in few other sources (Li et al. 2013). We have verified that the same feature is found in the RXTE observations of GRS 1915+105 during the 'plateau' states. We fit the spectra during these observations with the present spectral model consisting of cut-off power law and relativistically blurred reflection. The best fit spectral parameters are similar to that found for the present NuSTAR spectrum. We performed similar simulations using RXTE spectra and could reproduce the overall trend of increasing power of QPO. However, the flattening is not found in the simulation results. The observed flattening might be an indicator of the presence of more than one continuum component as suggested by Rodriguez et al. (2004).

Overall our simulation results can put significant constraints on the modulation mechanism assumed in various present theoretical models of QPO. Recently, Axelsson & Done (2015) have made an attempt to understand QPOs with frequency resolved spectroscopy. We suggest that the QPO phase-resolved spectroscopy, similar to that shown by Ingram & van der Klis (2015) can be another promising way to validate the spectral models, but with full energy resolution spectra. Recently launched Indian astronomy mission Astrosat (Singh et al. 2014), with large effective area of the LAXPC instrument, will provide ample opportunities for such QPO phase-resolved spectroscopy owing to its event mode data over broad energy range.

This research has made use of data obtained from High Energy Astrophysics Science Archive Research Center (HEASARC), provided by NASA's Goddard Space Flight Center. Research at Physical Research Laboratory is supported by Department of Space, Govt. of India. We thank A. C. Fabian and M. Parker for providing `reflionx_hc` model. We acknowledge the anonymous referee for his/her valuable comments.

REFERENCES

Axelsson, M., & Done, C. 2015, ArXiv e-prints
Blum, J. L., Miller, J. M., Fabian, A. C., et al. 2009, ApJ, 706, 60
Chakrabarti, S. K., Acharyya, K., & Molteni, D. 2004, A&A, 421, 1
Fender, R., & Belloni, T. 2004, ARA&A, 42, 317
Garain, S. K., Ghosh, H., & Chakrabarti, S. K. 2014, MNRAS, 437, 1329
Ingram, A., & Done, C. 2010, MNRAS, 405, 2447
—. 2012, MNRAS, 419, 2369
Ingram, A., & van der Klis, M. 2015, MNRAS, 446, 3516
Li, Z. B., Gao, H. Q., Zhang, Z., et al. 2014, MNRAS, 440, 143
Li, Z. B., Zhang, S., Qu, J. L., et al. 2013, MNRAS, 433, 412
Lin, D., Smith, I. A., Liang, E. P., & Böttcher, M. 2000, ApJ, 543, L141
Maccarone, T. J., Uttley, P., van der Klis, M., Wijnands, R. A. D., & Coppi, P. S. 2011, MNRAS, 413, 1819
McClintock, J. E., Shafee, R., Narayan, R., et al. 2006, ApJ, 652, 518
Mikles, V. J., Eikenberry, S. S., & Rothstein, D. M. 2006, ApJ, 637, 978
Miller, J. M., & Homan, J. 2005, ApJ, 618, L107
Miller, J. M., Parker, M. L., Fuerst, F., et al. 2013, ApJ, 775, L45
Mirabel, I. F., & Rodríguez, L. F. 1994, Nature, 371, 46
Molteni, D., Sponholz, H., & Chakrabarti, S. K. 1996, ApJ, 457, 805
Morgan, E. H., Remillard, R. A., & Greiner, J. 1997, ApJ, 482, 993
Muno, M. P., Morgan, E. H., & Remillard, R. A. 1999, ApJ, 527, 321
Qu, J. L., Lu, F. J., Lu, Y., et al. 2010, ApJ, 710, 836
Rao, A. R., Naik, S., Vadawale, S. V., & Chakrabarti, S. K. 2000, A&A, 360, L25
Rao, F., Belloni, T., Stella, L., Zhang, S. N., & Li, T. 2010, ApJ, 714, 1065
Reig, P., Belloni, T., van der Klis, M., et al. 2000, ApJ, 541, 883
Remillard, R. A., & McClintock, J. E. 2006, ARA&A, 44, 49
Remillard, R. A., McClintock, J. E., Orosz, J. A., & Levine, A. M. 2006, ApJ, 637, 1002
Rodriguez, J., Corbel, S., Hannikainen, D. C., et al. 2004, ApJ, 615, 416
Rodriguez, J., Varnière, P., Tagger, M., & Durouchoux, P. 2002, A&A, 387, 487
Rodriguez, J., Shaw, S. E., Hannikainen, D. C., et al. 2008, ApJ, 675, 1449
Schnittman, J. D., Homan, J., & Miller, J. M. 2006, ApJ, 642, 420
Singh, K. P., Tandon, S. N., Agrawal, P. C., et al. 2014, in Society of Photo-Optical Instrumentation Engineers (SPIE) Conference Series, Vol. 9144, Society of Photo-Optical Instrumentation Engineers (SPIE) Conference Series, 1
Sobczak, G. J., McClintock, J. E., Remillard, R. A., et al. 2000, ApJ, 531, 537
Sobolewska, M. A., & Życki, P. T. 2006, MNRAS, 370, 405
Stella, L., & Vietri, M. 1998, ApJ, 492, L59
Stiele, H., Belloni, T. M., Kalemci, E., & Motta, S. 2013, MNRAS, 429, 2655
Tagger, M., & Pellat, R. 1999, A&A, 349, 1003
Tomsick, J. A., & Kaaret, P. 2001, ApJ, 548, 401
Vadawale, S. V., Rao, A. R., Naik, S., et al. 2003, ApJ, 597, 1023
Vadawale, S. V., Rao, A. R., Nandi, A., & Chakrabarti, S. K. 2001, A&A, 370, L17
Varnière, P., Rodriguez, J., & Tagger, M. 2002, A&A, 387, 497
Vignarca, F., Migliari, S., Belloni, T., Psaltis, D., & van der Klis, M. 2003, A&A, 397, 729
Wagoner, R. V., Silbergleit, A. S., & Ortega-Rodríguez, M. 2001, ApJ, 559, L25
Zdziarski, A. A., Gierliński, M., Rao, A. R., Vadawale, S. V., & Mikołajewska, J. 2005, MNRAS, 360, 825
Zhang, L., Chen, L., Qu, J.-l., & Bu, Q.-c. 2015, AJ, 149, 82